UNIVERSITAT POLITÈCNICA DE CATALUNYA BARCELONATECH

Controlling the multipolar interference of nanoantennas

Ion M. Hancun

Controlling the multipolar interference of nanoantennas

Ion M. Hancu

Advisor: Prof. Dr. Niek F. van Hulst

ICFO – The Institute of Photonic Sciences

Table of Contents

The case for optical antennas

Light is generally emitted by single quantum oscillators. Specifically, the oscillation of an electric charge radiating light is the very definition of the most basic and common emitter there is: the electric dipole. In the case of atoms, fluorescent molecules, quantum dots and more, the electrons oscillate in a much-reduced volume, on a nanometer scale, while the wavelength of their fluorescence and absorption typically measures hundreds of nanometers. Thus, there is an enormous size mismatch between the wavelength of photons with which they interact most efficiently and the physical distance of the electron oscillation. This results in the low probability with which a photon can interact with a quantum emitter, as it is unlikely for such a photon to "see" the emitter. While focusing light with a lens or microscope objective can help, it only does so by increasing the number of attempts of achieving an interaction by adding more photons into the mix. Due to the diffraction limit, the spot size of a focused light beam cannot be smaller than roughly half the wavelength, so this size mismatch persists. One solution is to operate at cryogenic temperatures, but such configurations are as of yet incompatible with nanotech devices. The field of plasmonics, specifically optical antennas, addresses this size mismatch straightforwardly while still operating at room temperature [1-3].

A surface plasmon is the oscillation of electrons that is confined to the interface of any two materials wherein the real part of the electric permittivity changes sign at said interface. This is typically obtained at the interface of a metal and a dielectric. A surface plasmon can be driven both optically [4], as well as electrically [5]. The motion of charge along this interface creates electromagnetic fields that are highly confined to the volume near the interface, orders of magnitude smaller than the wavelength of excitation (Fig. 1). Given that negative permittivity materials are necessarily absorbing, the surface plasmon decays as the charge oscillates. This gives rise to two types of surface plasmons: propagating and localized. If the surface plasmon decays before reaching the edge of the surface (imagine a semi-infinite plane), and is not back reflected, it is called a propagating surface plasmon. If the electron oscillation is back reflected then it is a plasmonic resonator as the reflected plasmons interfere with the oncoming plasmons (assuming constant excitation), creating a cavity. These cavity plasmons are referred to as a localized surface plasmons, and the plasmonic resonators will be referred to as optical nanoantennas throughout the entirety of this thesis.

Inside a resonator, light travels back and forth a number of times before being leaked or absorbed, and in fact, that number of times is the quality factor *Q* of the resonator [6]. Therefore, the longer the average lifetime of a photon within the cavity, the higher the likelihood said photon has of interacting with a quantum emitter coupled to the cavity. The quality factors in optical antennas are generally between 10^1 and 10^2, as they are typically made of lossy metals. These values are quite low compared to those of lossless dielectric cavities that can easily be of the order of 10^5, and some laser cavities can even reach 10^{11}. However, one great advantage of plasmonics is the reduced mode volume of the oscillation. In a dielectric cavity, the mode volume is of the order of $\lambda^3_{free\ space}$ while for an optical antenna the mode volume is approximately one-thousandth of that. As the probability of an interaction is inversely proportional to the mode volume, this brings the two to par in that respect [7].

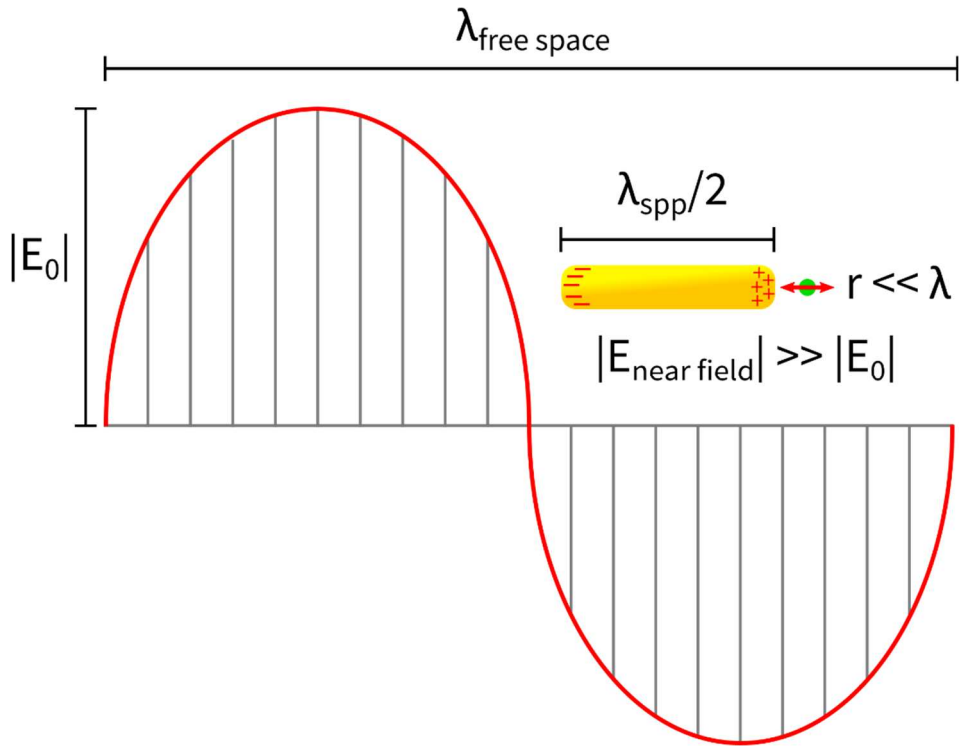

Figure 1 A schematic of the size mismatch between photons and single emitters. In red is the field of a photon propagating through free space. A single photon emitter and its dipole axis is represented with a green spot and red arrow, respectively, with its radius r typically being hundreds of times smaller than $\lambda_{free\ space}$. In yellow is a plasmonic dipole or λ/2 antenna, with its surface plasmon polariton (spp) wavelength, $\lambda_{spp,}$ being about half of $\lambda_{free\ space}$. The antenna localizes optical fields such that its near fields are much stronger than propagating photons, greatly increasing the interaction probability with the emitter.

Not only is the mode volume of a plasmonic antenna much smaller than a dielectric cavity, it also interacts with more light than one would expect given its physical size. As the electrons of such an antenna are free to move across its surface, they can react to electromagnetic fields from a distance. For example, a simple gold dipole antenna resonant near 800 nm under plane wave excitation interacts with light from an area almost 40 times larger than its physical cross section (Fig. 2 - red). The result is that not only are the electromagnetic fields used to drive the antenna localized to a much-reduced volume, but the antenna also interacts with a larger portion of the incoming photons [8].

Another consideration when discussing efficient light-matter interaction is the directionality, which is the direction in which photons are predominantly emitted, or reciprocally, the direction from which incoming photons are best detected. As the great majority of emitters radiate like electric dipoles, which is to say, not directionally, engineering optical antennas so that the antennas themselves or emitters coupled to them radiate unidirectionally can dramatically increase the efficiency of a device that makes use of the light emitted. As technology advances, we find more and more devices that can benefit from more efficient light-matter interactions. For example, in photovoltaic devices, a typical problem is

light being reflected or scattered before reaching the active layer, which is where photon absorption and charge separation takes place. An antenna that scatters light predominantly into one direction could in theory increase the efficiency of such a device. The logic gates used in quantum computing also depend on photon interactions, and these photons need to be emitted and later detected, so increasing the efficiency of these processes would improve their functionality. In fact, any device that requires the efficient interfacing between photons and electrons can in principle benefit from directional nanoantennas. As the light in high-Q dielectric resonators is generally scattered in multiple directions, not only are optical nanoantennas superior in that they can radiate unidirectionally, their much smaller size gives them the potential to be implemented in devices where size is critical.

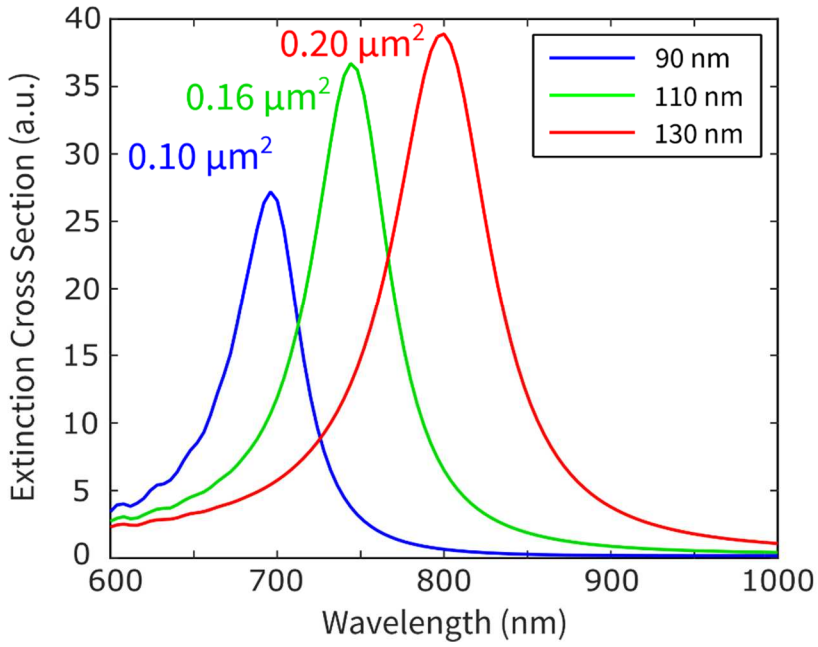

Figure 2 The normalized extinction cross section of three Au rod antennas of various lengths. Extinction is typically given in μm^2 but here each simulated spectrum was normalized to the size of each antenna (length x width). The lengths are in the legend, and the height and width of the antennas is 40 nm. The values next to each peak are the extinction (in μm^2) of that peak. The simulations include experimental details such as the adhesion layer used in nanofabrication.

The electric dipole and beyond

The majority of light emission falls under the electric dipole approximation, both when working with single emitters by themselves or when coupled to optical antennas, but this does not mean that non-electric dipole emission is always negligible or that it cannot be dominant [9]. An everyday example is found in the materials that line the insides of fluorescent lightbulbs. The lanthanide ions used, such as Europium, have numerous magnetic dipole transitions, and though they are typically slower than electric dipole transitions, they still form a non-negligible part of their emission spectrum. Electric quadrupole transitions have also been observed in

ordered molecular aggregates. While these transitions can potentially be enhanced by coupling such emitters to properly engineered optical nanoantennas [10-16], the focus of this work lies not in non-dipole transitions but mainly in the resonant non-dipole modes of the antennas themselves.

The basic electric dipole antenna is by definition a first order λ/2 resonance given the oscillating positive/negative charge distribution at the opposite ends of a rod-like geometry (Fig. 3a); similarly, doubling its length makes it a lambda or quadrupole resonance at the same wavelength. However, this second order λ mode has two antiparallel currents that oscillate along the antenna length, which cannot be driven by a symmetric source such as a plane wave at normal incidence. These even parity modes are sometimes referred to as "dark modes" but they are not dark in that they do not radiate light, they simply require more clever excitation schemes. For example, by coupling an electric dipole emitter to one end of a λ antenna, symmetry is immediately broken and the system can radiate in the quadrupole mode (Fig. 3b). For a magnetic dipole antenna, the simplest example is the electrically driven radiofrequency loop antenna, where the oscillating circular current creates a net magnetic dipole moment. Generally, to bring radiofrequency designs to the visible-to-near infrared region of the electromagnetic spectrum some changes must be made, as the electronics are not fast enough and the charge oscillation must be driven optically. The plasmonic analogue of the loop antenna, like the quadrupole antenna, requires symmetry to be broken. The geometry is known as the split-ring resonator (Fig. 3c), and its λ/2 resonance is driven with a light source polarized across the antenna gap so that the resulting charge oscillation creates both an electric dipole moment across the gap and a magnetic dipole moment within the center of the ring. As each multipole has different field symmetries, the presence of one or more of these multipoles potentially allows that their interference can be used to direct light emission, which is the overall focus of this Thesis.

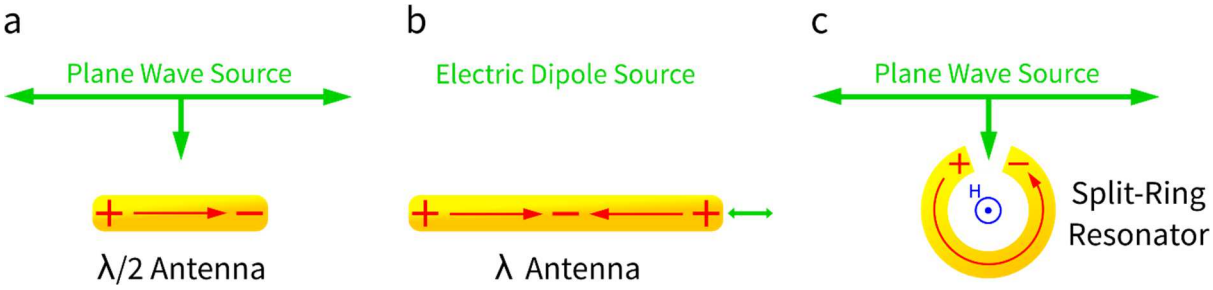

Figure 3 An assortment of optical nanoantennas and how they might be driven. The sources are shown in green, the resulting charge distributions and currents in red, and the magnetic field in blue. **(a)** A λ/2 or dipole antenna driven by a plane wave. **(b)** A λ or quadrupole antenna driven by a local electric dipole source. The antiparallel currents prevent this antenna from being driven by a plane wave. **(c)** A split-ring resonator driven by a plane wave. The circular current creates a magnetic dipole moment in its center.

From linear to nonlinear

Light emission from single photon sources, regardless of any enhancements, is ultimately the result of spontaneous emission, and is thus an incoherent process. If one were interested in, for example, achieving a switchable directivity from a single nanoantenna, then a coherent process is required. With this goal in mind, we turn to second harmonic generation (SHG) directly from optical nanoantennas. The capacity for plasmonics to confine optical fields to nanometric volumes not only increases the emission of single photon emitters, but also increases the likelihood of nonlinear processes occurring [17]. In the case of SHG, its power output is a function of the fourth power of the excitation field. Optical nanoantennas generate second harmonic mainly from their field hot spots, with a well-defined phase between them, but they can also behave as a resonant scatterer. Thus, there is a paradigm shift in their behaviour with respect to the linear regime. The understanding and characterization of the SHG from nanoparticles is necessary before we can engineer directional second harmonic nanoantennas.

Thesis outline

The outline is as follows:

- In Chapter 1, I explain the experimental and theoretical methods I applied over the course of this project, which include nanofabrication, the optical setup, pulse shaping, FDTD simulations, and the multipole model.

- In Chapter 2, I present how the interference of two multipoles in a higher-order mode of a U-shaped split-ring resonator emits the light from quantum dots coupled to it unidirectionally.

- In Chapter 3, I move onto the coherent emission process, second harmonic generation, directly from single plasmonic nanoantennas, and study the emission patterns of two nanoantenna geometries. I model their radiation patterns with the same multipole model and attribute them to a purely surface second harmonic contribution. I then control the local phase of the cross antenna to manipulate the radiation pattern, which is not possible with an incoherent emitter.

- In Chapter 4, I take a detour, and measure the angular radiation patterns of the second harmonic from crystalline silicon nanowires to distinguish the different competing processes that lead to SHG. In contrast with the previous chapter, the SHG observed comes from three distinct processes.

- In Chapter 5, I go back to the second harmonic from plasmonic antennas and demonstrate the switchable directional emission from a single plasmonic antenna, and study its mode of operation, the surface and bulk origin of its emission and their coherent interference that leads to unidirectional emission.

Chapter 1

Methods

In this chapter, we introduce the experimental, computational and theoretical methods employed throughout this Thesis for the characterisation of light emission by optical nanoantennas. On the experimental side, we first describe the process of sample preparation, move on to show how the antenna systems are characterized in our optical microscope, and finally describe the process used to compress broadband laser pulses used in the later chapters of this Thesis. We then move onto the computational side to show how our nanoantennas and emitters are characterized in FDTD simulations, and then use those simulated results to assist us in our theoretical fits of experimentally measured radiation patterns.

1.1 Sample fabrication

To fabricate the nanoantennas we used positive tone electron-beam lithography, as is shown in Fig. 1.1. First, a cleaned coverslip has a 5-10 nm layer of indium-tin oxide (ITO) deposited on it using e-beam evaporation. ITO is used because it is a transparent conductor, but as the evaporation process removes the oxygen from the material, even 10 nm makes the coverslip visibly opaque, so it is then baked at 350º C for 15 minutes so that oxygen from the air is absorbed, making the layer transparent. The purpose of the ITO is twofold; first, it is an adhesion layer for the metal that is deposited on top, and second, it is a conduction layer that helps remove excess charge during the e-beam writing of antenna geometries. This also allows for later imaging of said geometries in a scanning electron microscope (SEM) without having to destroy the sample.

Next, a layer of positive electronic resist, polymethyl methacrylate (PMMA), is spun-cast onto the coverslip and baked at 130º C for 5 minutes for drying. The e-beam lithography then defines the Au antenna structures, and the exposed areas are removed with a solvent in the development step, before Au is evaporated onto the entire coverslip. For the last step, lift-off, another solvent is used to remove the excess PMMA and Au, leaving behind the structures defined by the e-beam writing. In Chapters 3 and 5 the nanoantennas themselves are the emitters, whereas in Chapter 2 we couple single emitters to the nanoantennas, which requires further sample preparation before the lift-off. To chemically attach quantum dots to the Au nanoantennas we functionalize the sample surface with a thiol group molecular chain, mercapto-undecanoic acid (MUA, which has specificity to Au), and then use a carbodiimide to activate the carboxylic acid terminations of MUA, so that the amino groups of the quantum dots used can bind to them. After performing lift-off the quantum dots are attached all over the nanoantennas without leaving fluorescent emitters in between them.

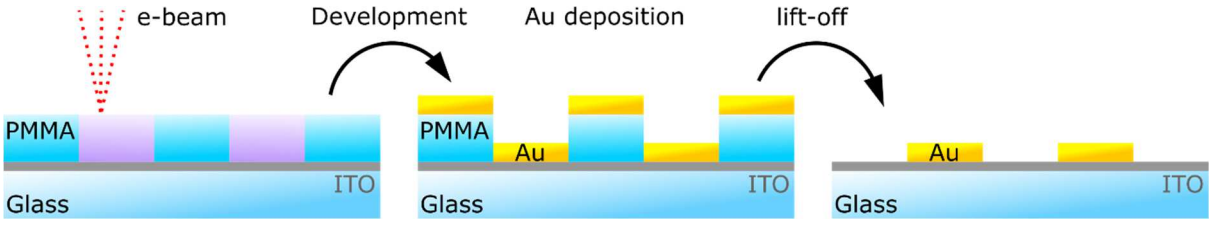

Figure 1.1 A step-by-step explanation of e-beam lithography. The e-beam resist, PMMA (blue), is first exposed to write the nanoantenna geometries that we wish to study. The exposed area (purple) is then removed in the development step, and Au is then deposited via thermal evaporation onto the sample. Finally, the residual PMMA and excess Au is removed in lift-off, leaving behind arrays of Au nanoantennas with a periodicity of 1.5 μm.

1.2 Confocal microscopy and angular imaging

The first step in studying single antennas is to assess the quality of the nanofabrication. Confocal microscopy allows us to hone in onto single antennas within arrays and analyze their characteristics. The microscope is a Zeiss Axiovert 200 with a high-NA oil immersion objective (Zeiss, α Plan-Apochromat 100x/1.46 NA). The high-NA objective is critical for increasing the collection efficiency of this setup, as most light radiated near an interface does so mainly into the higher-index medium and at angles above the critical angle. The sample is mounted on a piezoelectric stage to scan our sample around with respect to the laser excitation, and allows for the one-by-one measuring of nanoantennas. The laser spectrum is then filtered out from the signal of interest using a dichroic mirror, and one or more dichroic filters. This signal is then sent to one detection arm and focused onto an avalanche photodiode (Perkin Elmer, SPCM-AQR-14 and 16) for real space imaging, and with the optics selected such that the focal spot is the same size as the APD sensor. Scanning over a nanoantenna array and measuring its two-photon photoluminescence shows that the signal comes purely from the antennas, with no residual light emission from the areas away from the antennas (Fig. 1.2, right). Along the other detection arm, we measure the angular emission pattern of the object of interest by further magnifying and imaging the back focal plane (BFP) of the objective on an electron-multiplied CCD camera (Andor, iXon+ 897). This technique has been used to determine the orientation of single molecules [18] as in a single measurement it shows nearly the entire angular pattern of the light emitted into the glass half-space of a sample. Each point in the BPF correspond to angular coordinates θ and φ, which will be described in more detail in Chapter 2. The patterns are typically measured over an area of 130x130 pixels in the emCCD. This setup allows for the easy measurement of both real space and momentum space of single antennas.

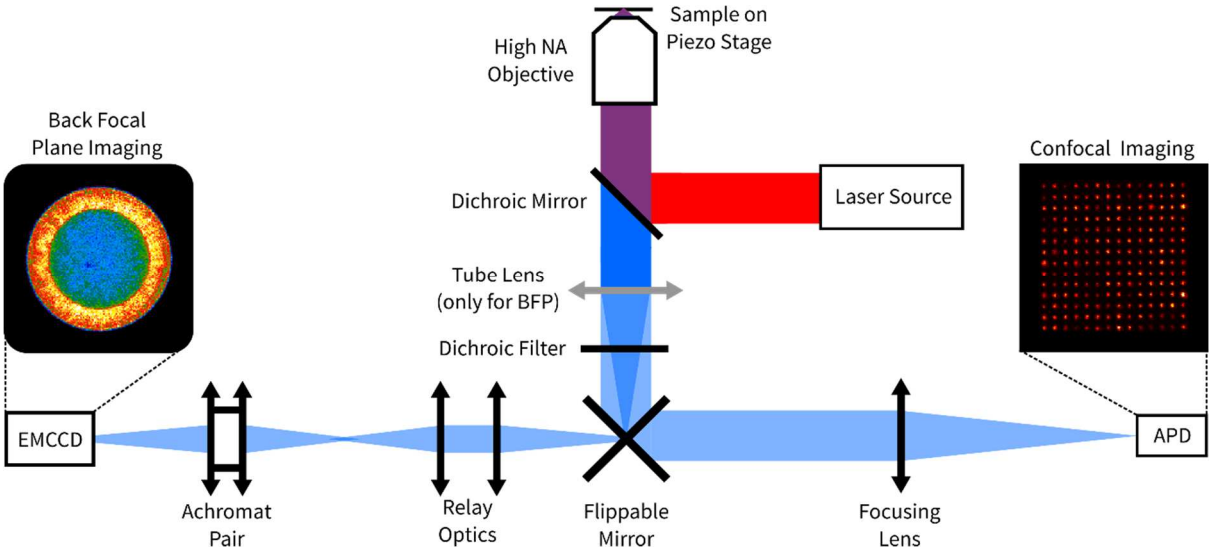

Figure 1.2 A schematic of the confocal microscope used. A laser source is focused to a diffraction-limited spot and used to excite the sample of interest, which is scanned around on a piezoelectric stage. The signal of interest is then imaged on one of two detection channels, which correspond to the image plane of the objective (right side), and the objective's back focal plane (left side).

In this Thesis light emission from single nanoscale objects is excited using one of two lasers. In Chapter 2, we used a Helium-Neon continuous wave laser that operates at 633 nm, and in Chapters 3-5 for the second harmonic generation measurements, we used a pulsed titanium sapphire laser with a spectrum between 760 and 860 nm, and a repetition rate of 85 MHz. In order to maximize the second harmonic signal, it is necessary to maximize the peak electric fields at the sample plane, and we a pulse shaper based on a liquid crystal spatial light modulator (SLM) to do this [19-28].

1.3 Pulse compression

The pulse shaper is arranged in a 4-f configuration and is illustrated in Fig. 1.3. The chirped laser pulse enters from the left and is spectrally dispersed with a diffraction grating. The grating is exactly one focal length away from the spherical mirror, and the SLM is placed at its Fourier plane. The second spherical mirror, placed another focal length away from the SLM, focuses light onto a second grating, and the collimated beam is sent to the microscope.

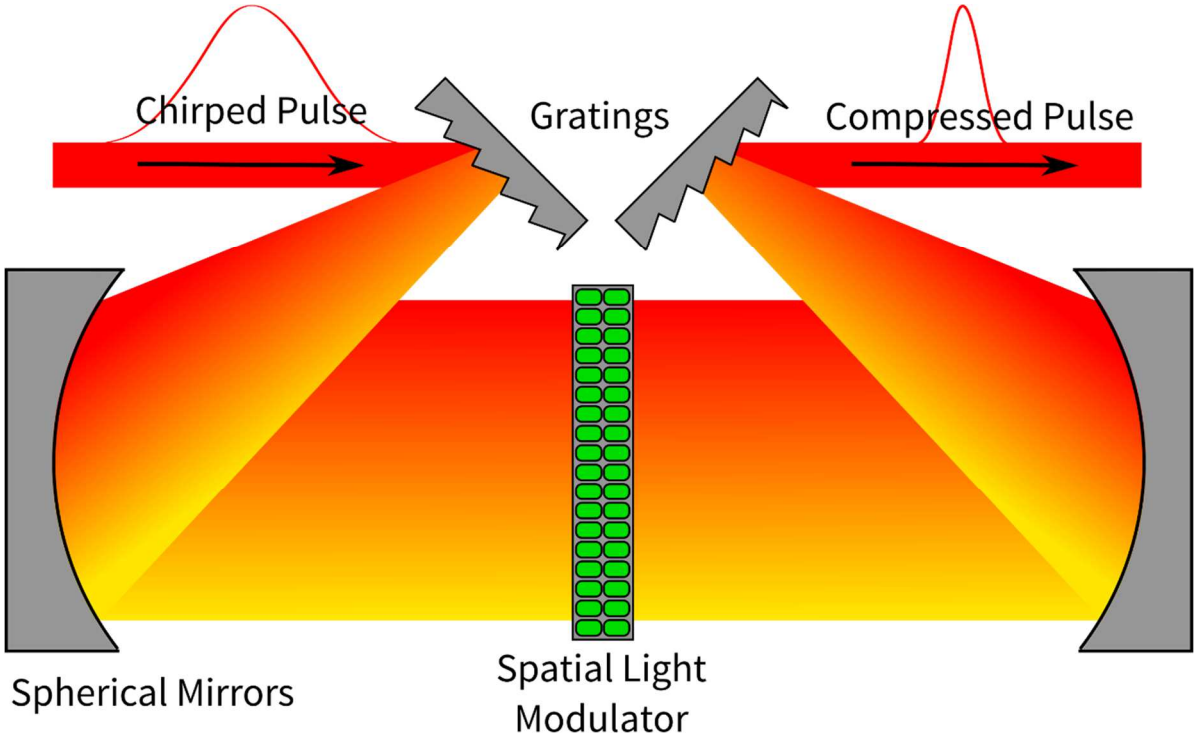

Figure 1.3 A schematic of the 4-f pulse shaper used. The chirped pulse is spectrally divided onto the spatial light modulator in order to modify the spectral phase at each wavelength independently, before being recombined and sent to the microscope.

As the optical elements along the laser path are dispersive due to the variation of their refractive index over the laser spectrum, the pulse becomes chirped as it propagates through more elements [29-32]. This is mostly due to the thick glass of our objective, but other optical elements can also have an effect. Multiple techniques exist for studying ultrafast laser pulses,

such as frequency resolved optical gating (FROG) [33-34], and spectral phase interferometry for direct electric field reconstruction of ultrashort optical pulses (SPIDER) [35], but our group normally uses multiphoton intrapulse interference phase scan (MIIPS) [26, 36-40]. The objective of MIIPS is to produce Fourier-limited pulses at the sample plane, so it measures phase distortions in the SH spectrum of a nonlinear crystal by iteratively applying different phase masks to the SLM. Once the phase distortions are well defined, the SLM applies a phase mask of the inverted phase so that the pulses at the sample plane are Fourier limited.

This method requires the detection of the second harmonic generation (SHG) from a nonlinear crystal smaller than our excitation spot, typically $BaTiO_3$ [41], with a flat spectral response to the laser field, such that the measured spectral phase is purely from the laser and not due to any resonance effects. For a broadband laser where $E(\omega) = E_0(\omega)e^{-i\varphi(\omega)}$ each frequency component can be doubled to obtain SHG, but frequencies can also be summed for sum frequency generation (SFG). Assuming a central frequency ω whose second harmonic is 2ω, $\omega + \delta\omega$ and $\omega - \delta\omega$ can yield a signal at 2ω through SFG. This means that the second harmonic (SH) spectrum can be Gaussian even when the laser spectrum is not (Fig. 1.4). For convenience, from here on we will use the term SHG to include SFG as well. The SH spectrum is defined as follows:

$$SH(2\omega) = \left|\int |E_0(\omega+\Omega)||E_0(\omega-\Omega)|e^{i[\varphi(\omega+\Omega)+\varphi(\omega-\Omega)]}d\Omega\right|^2 \qquad (1.1)$$

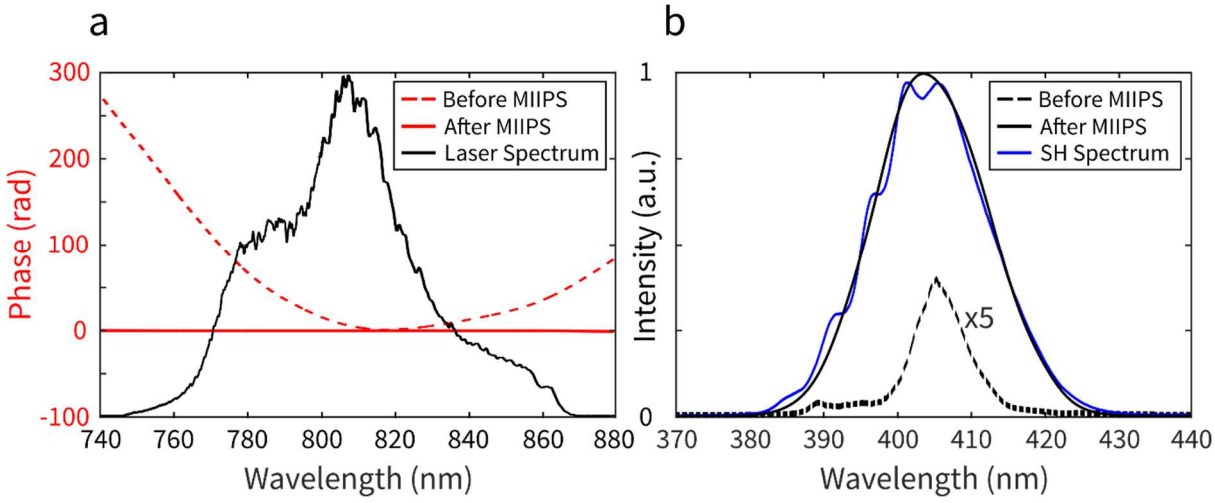

Figure 1.4 Broadband laser pulse compression with MIIPS. (a) The measured spectrum of our laser (black), and its spectral phase before (dashed) and after (solid) running MIIPS. **(b)** The simulated SH spectrum from a nonlinear nanoparticle calculated with equation (1) using the experimental laser spectrum and the measured phases (black), and the measured SH spectrum after pulse compression (blue). Note the very similar, though imperfect, measured SH spectrum with respect to the simulation. The low shoulder of the pre-compressed pulse (dashed) at 390-400 nm clearly corresponds to the shoulder in the laser spectrum at 780-800 nm, but disappears in the simulated compressed pulse to obtain a Gaussian SH spectrum. The SH signal increases 25-30x with respect to the uncompressed pulses, indicating that their duration before and after MIIPS is ~80 and ~15 fs, respectively.

The measured laser spectrum (Fig. 1.4a) has a bandwidth of about 40 nm at FWHM, from 780 to 820, while the theoretical SH spectrum after MIIPS is from about 395 to 315 nm (Fig. 1.4b). The ~5 nm red-shift from the expected center is a result of the fundamental spectrum having its peak near 810 nm, and its long tail in the red part of the spectrum. Note how the phase shifts hundreds of radians over the laser spectrum while after compression the phase shifts less than 0.1 radians, and how the total SH signal increases 25-30 times. As maximizing the SH signal is the only use of MIIPS required in this Thesis, its finer details will not be discussed in here. For more information on its functionality and further applications, please refer to the published works of its inventor, Markus Dantus [24, 36-40], as well as some of our other published works [28, 41].

1.4 Finite-difference time-domain simulations

In the coming chapters we employ finite-difference time-domain (FDTD) simulations to improve our antenna design and help interpret experimental results. To this end, we employ the software *FDTD Solutions* (Lumerical Inc.). In the majority of our simulations, we model all of the materials used to represent our experimental conditions as accurately as possible. This means that both the glass coverslip and ITO layer are modelled along with the antenna of interest. Without these components, the resonant modes of our antennas can easily blue-shift 100 nm or more. The corners of the antennas must also be rounded as their terminations shift the resonances, and there are no infinitely sharp corners in the nanofabrication process.

The first main use of our simulations is to identify the resonance modes of antennas of a given geometry, which we do with either near or far field excitation depending on the aim of the experiment. To calculate the extinction cross section of an antenna at a given resonance, we use the source called total field scattered field (TFSF). The TFSF source is essentially a closed box that injects a plane wave from one of its surfaces, and subtracts the light that exits the box without interacting with the objects inside of it. The sketch in Fig. 1.5a depicts this source as well as two boxes of planar power monitors, which are found within and outside of the TFSF source. The exterior monitors record the intensity of light scattered by the geometry, and the interior monitors record a combination of the scattered light, the injected intensity, and the transmitted intensity, which are used to calculate the absorption. The sum of absorption and scattering is the extinction of the antenna. Employing a plane wave at normal incidence, this method can only calculate modes of odd parity.

To identify both even and odd parity antennas modes, as well explore the changes in radiative rate, we use an electric dipole source in lieu of a plane wave (Fig. 1.5b). The dipole source in FDTD solutions has a pre-defined amplitude of unity for when it radiates in a homogenous non-absorbing medium, and an internal quantum efficiency of 100%. When such an emitter is coupled to a resonator its local density of optical states (LDOS) increases proportionally with the quality factor of the resonator dived by the mode volume (LDOS $\propto$ Q/V) [8, 42-45]. The increase in LDOS, typically referred to as the Purcell factor, means that the emitter has more radiative channels through which to emit light, and can go through more

cycles of photon absorption (excitation) and photon emission (relaxation). The interior power monitors in Fig. 1.5b record this radiative enhancement spectrum, while the exterior monitors record the power radiated into the far field. The values are different due to absorption in the antenna, and their quotient is the external quantum efficiency of the system.

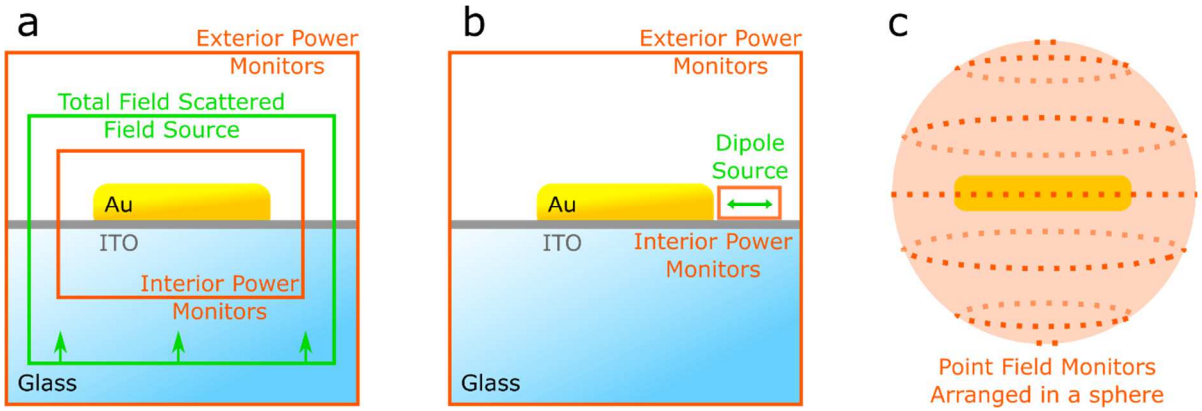

Figure 1.5 Diagrams of the different types of simulations realized in order to characterize the optical antennas studied. (a) A sketch illustrating how the extinction spectrum of a nanoantenna is calculated. **(b)** A sketch illustrating how the radiative rate enhancement of a nanoantenna is calculated. **(c)** A sketch illustrating how the multipole moments of a nanoantenna is calculated.

Finally, in order to calculate the dominant multipole moments of a given antenna, we remove the substrate to obtain a homogeneous medium and place the optical nanoantenna in the center of a sphere of point field monitors with a radius much larger than the length of the antenna. Using the methods described by Grahn et al. [46], we use the recorded scattered fields to calculate the multipole coefficients from the electric dipole up to the next order of multipoles, the magnetic dipole and electric quadrupole, as follows:

$$a(l,m) = \frac{(-i)^{l+1}kr}{h_l^{(l)}(kr)E_0[\pi(2l+1)l(l+1)]^{1/2}} \int_0^{2\pi}\int_0^{\pi} Y_{l,m}^*(\theta,\varphi)\,\hat{\boldsymbol{r}}\cdot\boldsymbol{E}_s(r)sin\theta\,d\theta\,d\varphi \tag{1.2}$$

$$b(l,m) = \frac{(-i)^{l}Z_0kr}{h_l^{(l)}(kr)E_0[\pi(2l+1)l(l+1)]^{1/2}} \int_0^{2\pi}\int_0^{\pi} Y_{l,m}^*(\theta,\varphi)\,\hat{\boldsymbol{r}}\cdot\boldsymbol{H}_s(r)sin\theta\,d\theta\,d\varphi \tag{1.3}$$

where l is the order of the multipole (l = 1 for dipole and 2 for quadrupole), m varies from $-l$ to l, k is the wave vector, r is the radius of the sphere, Z_0 is the vacuum impedance, h is the Hankel function, and $Y_{l,m}$ is the spherical harmonic. The coefficients are then used to define the electric dipole p, magnetic dipole m, and electric quadrupole Q, as follows [47]:

$$p = \begin{pmatrix} p_x \\ p_y \\ p_z \end{pmatrix} = C_0 \begin{pmatrix} a_{1,1} - a_{1,-1} \\ i(a_{1,1} + a_{1,-1}) \\ -\sqrt{2}\,a_{1,0} \end{pmatrix} \tag{1.4}$$

$$m = \begin{pmatrix} m_x \\ m_y \\ m_z \end{pmatrix} = cC_0 \begin{pmatrix} b_{1,1} - b_{1,-1} \\ i(b_{1,1} + b_{1,-1}) \\ -\sqrt{2}\, b_{1,0} \end{pmatrix} \tag{1.5}$$

$$Q = \begin{pmatrix} Q_{xx} & Q_{xy} & Q_{xz} \\ Q_{yx} & Q_{yy} & Q_{yz} \\ Q_{zx} & Q_{zy} & Q_{zz} \end{pmatrix} =$$

$$D_0 \begin{pmatrix} i(a_{2,2} - a_{2,-2}) - \frac{i\sqrt{6}}{2} a_{2,0} & (a_{2,-2} - a_{2,2}) & i(a_{2,-1} - a_{2,1}) \\ (a_{2,-2} - a_{2,2}) & -i(a_{2,2} + a_{2,-2}) - \frac{i\sqrt{6}}{2} a_{2,0} & (a_{2,-1} + a_{2,1}) \\ i(a_{2,-1} - a_{2,1}) & (a_{2,-1} + a_{2,1}) & i\sqrt{6} a_{2,0} \end{pmatrix} \tag{1.6}$$

where $C_0 = (6\pi)^{1/2} i/cZ_0k$, $D_0 = 6(30\pi)^{1/2}/iZ_0ck^2$, and c is the speed of light in vacuum. When the antenna medium is changed from an interface (across which n changes from 1.5 to 1) to a homogenous medium (where n is 1), its resonance is blue-shifted. The precise values for the fields scattered by the antenna also have minor variations when the center of the spherical monitor is shifted. Because of these reasons, these calculations are used only to identify the dominant multipole terms so that we can fit them to experimental measurements.

1.5 Multipole fitting

The final method necessary for understanding the following chapters is multipole fitting. To do this we analytically calculated the angular emission patterns of all of the electric dipole, magnetic dipole and electric quadrupole terms [48-49]. In the case of the electric and magnetic dipoles, they each have three independent terms (eq. 1.4-1.5), while the electric quadrupole has five independent terms that are used to define the nine terms of the symmetric matrix in eq. 1.6. The BFP patterns of each multipole can be seen in Fig. 1.6. The p_y, m_y, Q_{yy} and Q_{yz} terms are omitted as they are simply 90º rotations of p_x, m_x, Q_{xx} and Q_{xz}, respectively. Note how the parallel electric and magnetic dipole components show similar patterns, and only vary in the sharpness of their emission peaks near the critical angle (Fig. 1.6a-d). In free space, an x-oriented electric and magnetic dipole have the same far-field radiation pattern, even though their electric and magnetic field symmetries are inverted. When radiating near an interface, these in- and out-of-plane electric fields lead to different transverse electric and magnetic Fresnel coefficients, so the light they radiate is refracted differently into the glass side of the glass-air interface, giving rise to the complementary sharp/dull peaks in Fig. 1.6 a/c and b/d.

To fit these terms to an experimental pattern we preselect the dominant terms as described in the previous section, normalize the patterns so that they each radiate a total intensity of unity, and fix the amplitude and phase of one while varying the amplitude and phase of the others. The fits are done using a least squares method and the quality of the fit is quantified using the coefficient of determination, R^2.

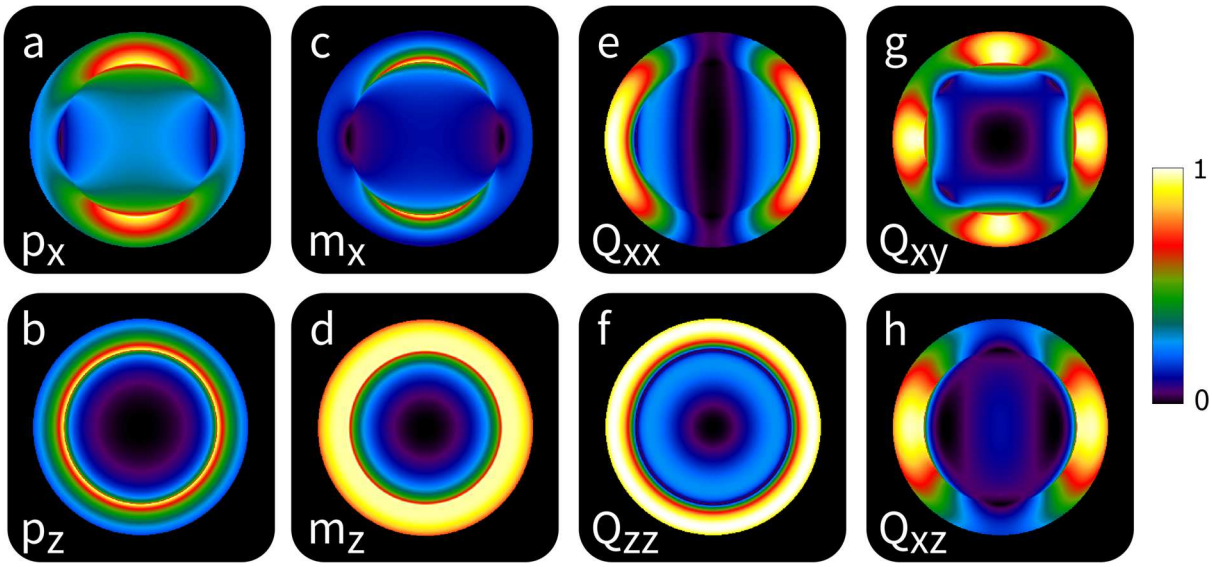

Figure 1.6 The theoretical back focal plane patterns of various multipoles at different orientations radiating near a glass-air interface. (a-b) The x- and z-oriented electric dipole. **(c-d)** The x- and z-oriented magnetic dipole. **(e-f)** The x- and z-oriented linear electric quadrupole. **(g-h)** The x-y and x-z lateral (or box) electric quadrupole. The y-oriented electric dipole, magnetic dipole, and linear electric quadrupole are simply 90º rotations of (a), (c) and (e), respectively. The y-z lateral electric quadrupole is a 90º rotation of (h).

Chapter 2

Split-ring resonators for directed light emission

By directing light, optical antennas can enhance light-matter interaction and improve the efficiency of nanophotonic devices. Here we exploit the interference between the electric dipole, quadrupole and magnetic dipole moments of a split-ring resonator to experimentally realize a compact directional optical antenna. This single-element antenna design robustly directs emission even when covered with nanometric emitters at random positions, outperforming previously demonstrated nanoantennas with a bandwidth of 200 nm and a directivity of 10.1 dB from a sub-wavelength structure. The advantages of this approach bring directional optical antennas closer to practical applications.

2.1 Directional nanoantennas

Optical devices such as sensors, solar cells or interfaces for integrated optics often require an efficient interaction with light in well-defined directions. Optical antennas offer a promising means to engineer and control the directional response of materials to light. Most optical antenna designs demonstrated to date are scaled down counterparts of radio and microwave antennas, now tuned for operation at much shorter wavelengths [1]. To obtain directional light emission or reception, design strategies inspired by conventional antenna engineering might be employed. For example, beaming has been achieved through the interference of antenna elements arranged in arrays to engineer their relative phase (Yagi-Uda antennas [50-52], grating-like designs [53-55]). However, this principle of operation is limited by a specific operation frequency and the challenging need to position local sources with nanometric accuracy to drive the antenna [44, 50, 56]. Alternative designs such as aperture [54], leaky-wave [57-58], patch [59] or reflector [60] antennas require larger footprints to obtain broadband directionality and do not solve the need to position sources with nanometric accuracy. Therefore, designing a single-element directional antenna that is compact, broadband and robust is a significant step towards applications.

In this Chapter, we demonstrate a principle for directional light emission based on the interference between different multipolar moments excited in a single metal antenna element. This multipolar interference concept is sketched in Fig. 2.1a; the fields radiated by different multipoles (electric dipole, quadrupole and magnetic dipole) have distinct field symmetries, which we exploit for the design of optical antennas with a target radiation pattern. When emitting with the same polarization, the interference of the electric fields of perpendicular electric and magnetic dipoles (or parallel electric dipoles and quadrupoles) depends on their relative phase. The result is that their interference is constructive in one direction and destructive in the opposite when their phase difference is $\pi/2$ or $3\pi/2$, whereas their interference is prevented if they are in or out of phase (0 or π). Therefore, it becomes possible to obtain a unidirectional emission if a local light source (e.g., an electric dipole transition) couples to an antenna that simultaneously induces electric dipole and higher-order moments.

To implement this multipolar interference at optical frequencies, nanostructures with coexisting multipolar moments are required. Directional scattering has been demonstrated in semiconductor nanospheres supporting simultaneous electric and magnetic dipole resonances [61-66], and the directionality of metal-dielectric nanoshells [67-68], nanocups [69], and V-antennas [70] have also been attributed to the role of additional multipole scattering beyond electric dipoles. Here, we exploit the concept of interference between multipolar moments to achieve directional light emission from sub-diffraction-limited sources. To this end, we employ single split-ring resonators (SRRs), which have mainly been studied within the context of metamaterials [71-74].

2.2 Measuring uSRRs

First, we tailor the geometry of a U-shaped resonator (Fig. 2.1b) to tune its directivity to the spectrum of our electric dipole sources. The structure consists of two parallel arms and a perpendicular connecting element (bridge). Similarly to a gap antenna, by reducing the gap between both arms in our SRRs we create a more intense near field for improving the coupling of electric dipole emitters to the antennas and selectively enhance the radiated power of the emitters located within it. The presence of the bridge connecting both arms differentiates the SRR from two parallel unconnected wires, leading to an asymmetry in the angular pattern.

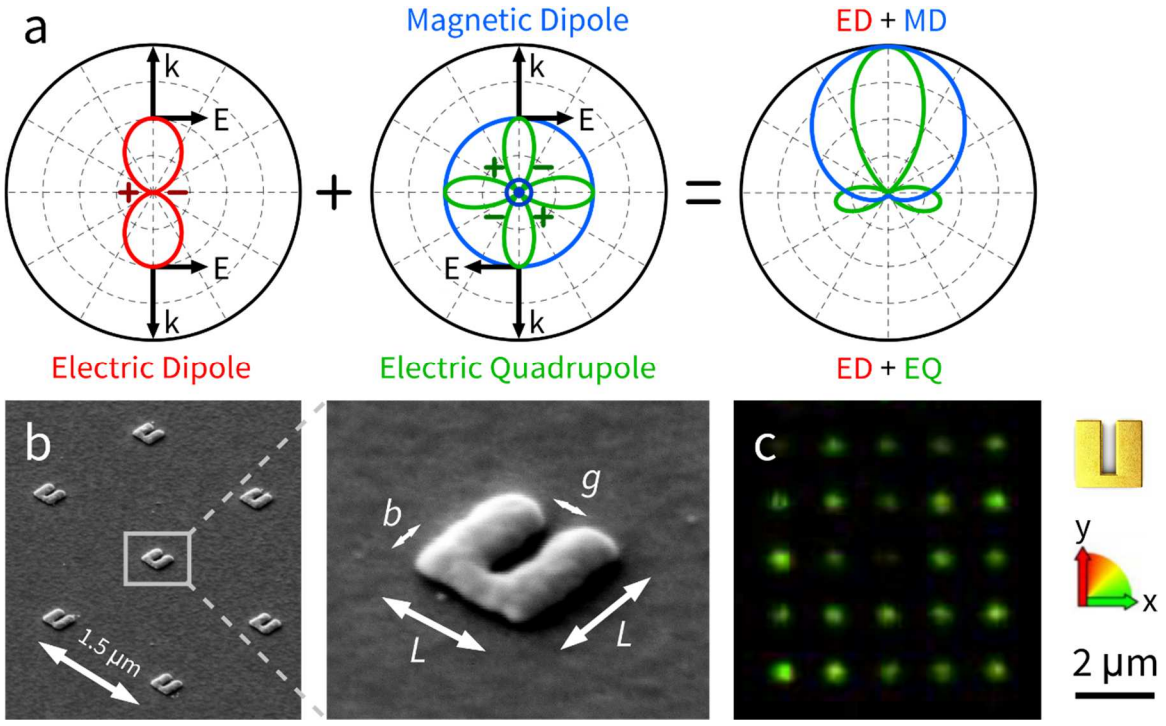

Figure 2.1 Principle of multipolar interference for directional emission. (a) Two examples of directional emission are obtained from the maximized interference of an in-plane electric dipole (red) with an out-of-plane magnetic dipole (blue), or with an in-plane lateral electric quadrupole (green). **(b)** Fabricated split-ring resonators in a scanning electron microscopy image. The parameters of the gold nanoantennas are bridge (b), gap (g) and length (L) with values $30 \leq b \leq 60$, $35 \leq g \leq 55$ and $L = 250$ nm. **(c)** A confocal photoluminescence image of an array of nanoantennas excited by quantum dots shows that the emission is localized at the antenna positions. The color scale denotes the orientation of the linear polarization of the emission.

To fabricate the nanoantennas we use electron beam lithography, thermal evaporation and lift-off, as described in Chapter 1. SRRs with different size parameters (Fig. 2.1b) are studied. Colloidal quantum dots (QDs) are the optical sources that drive the antennas. The QDs have a luminescence spectrum peaking at a wavelength of 790 nm with a full-width at half-maximum (FWHM) of 80 nm (Invitrogen, Qdot 800 ITK amino (PEG)). The nanoantennas are

functionalized with mercaptoundecanoic acid to attach the QDs specifically to the gold structures and at a distance of several nanometers.

We detect the photoluminescence of QDs coupled to single nanoantennas with a confocal microscope with a high numerical aperture oil-immersion objective (1.46 NA). A piezo stage is used to scan the sample confocal detection volume. To excite the QDs, circularly polarized light with a wavelength of 633 nm wavelength (10 μW of power) from a He-Ne laser is focused to a diffraction-limited spot. The reflected excitation beam is filtered from the emitted luminescence with a dichroic mirror and a long-pass filter. The signal is then divided with a polarizing beam-splitter and detected with two avalanche photodiodes, corresponding to linear polarizations along the *x* and *y* axes. To obtain angular emission patterns, momentum-space images are recorded at the back focal plane of the objective with an electron-multiplying CCD camera. This allows for a one-by-one characterization of selected antennas in both real space and k-space.

The emission is neatly localized at the antennas with no residual QD luminescence from the surrounding substrate (Fig. 2.1c). Confocal microscopy reveals that the light collected from QDs coupled to the SRRs is mainly polarized across the antenna gap (green color in Fig. 2.1c). Defining the degree of linear polarization $DOLP = (I_x - I_y) / (I_x + I_y)$, the polarization average over the array is $DOLP = 0.60$ ($I_x = 4I_y$). This indicates that the QDs are efficiently coupled to the antennas and are probably exciting the gap mode.

We demonstrate broadband beaming of light by multipolar interference antennas using back focal plane measurements. Most of the emission is radiated unidirectionally (see Figure 2.2a) by coupling to a SRR tuned in size to maximize its directionality. To quantify this observed directionality, we define the front-to-back ratio (*F/B*) as the intensity ratio between the point of maximum emitted power and the point diametrically opposite to it in the back focal plane image. This value is 8.5 dB and spans the entire QD emission spectrum. By changing the size of the SRR, we detune it from the QD emission spectrum and obtain an *F/B* of 3.9 dB (Fig. 2.2b – Detuned SRR). Generally, when dipolar emitters radiate near an interface, they emit predominantly into the higher-index medium (about 78% for our glass-air interface). There is also a sharp maximum near the critical angle ($\theta_C = 41.1°$) [75]. In the absence of an antenna, the lack of a preferential dipole orientation results in symmetric ring-like patterns with *F/B* = 0 dB (Fig. 2.2b – Without SRR). The outer edge of the back focal plane images is given by the maximum collection angle of our objective, the numerical aperture ($\theta_{NA} = 72.8°$). These Fourier-plane images contain information on the direction of light emission through the glass substrate and thus we can convert them to angular space to clearly represent the directional emission and *F/B* (Fig. 2.2b).

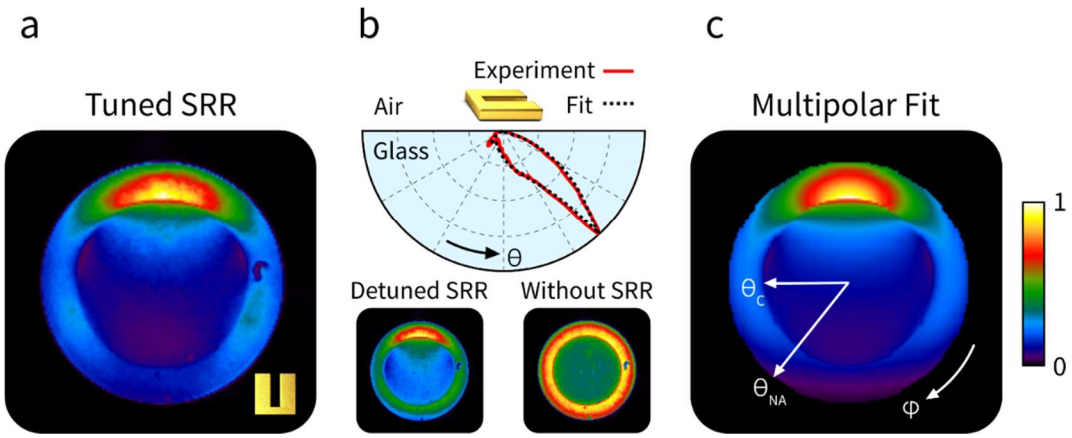

Figure 2.2 Directed broadband emission by split-ring resonator antennas. (a) Experimental angular radiation pattern as recorded at the back focal plane of the microscope objective showing that a SRR (parameters L = 250, b = 50 and g = 35 nm) emits unidirectionally even when QDs are coupled to it at random positions. **(b)** A vertical slice of the previous radiation pattern converted to angular space, highlighting the dielectric interface between air and the glass substrate. The bottom insets show the emission patterns of a SRR with dimensions slightly detuned from the QD emission spectrum (L = 200, b = 50 and g = 35 nm) and the omnidirectional pattern of QDs without a SRR (left and right, respectively). The images contain the entire QD emission spectrum (790 ± 40 nm at FWHM). **(c)** Calculation of the angular pattern by fitting the experimental result in (a) with a superposition of multipolar point sources, considering an electric dipole (p_x), a magnetic dipole (m_z) and a lateral electric quadrupole (Q_{xy} = Q_{yx}). The detailed features of the pattern are reproduced with this simple model, including the various minima and small side lobes.

Such directionality is consistently obtained for many antennas with the same nominal dimensions (Fig 2.3). The fabricated structures, whose emission patterns are shown in Fig. 2.3, have varying nominal bridge and gap sizes and the back focal plane images of 37 of them were recorded. These were selected based on their total emission intensity and degree of linear polarization. We observed that structures with relatively large gaps tended to direct light less, likely due to the less-intense electric near fields within the gap. This would decrease the emission enhancement of the quantum dots (QDs) within the gap and thus increase the weight of the QDs coupled to the antennas from outside the gap. Since the QDs are attached to the SRR at random positions, these results demonstrate the robustness of our nanoantenna design for directing light from local emitters.

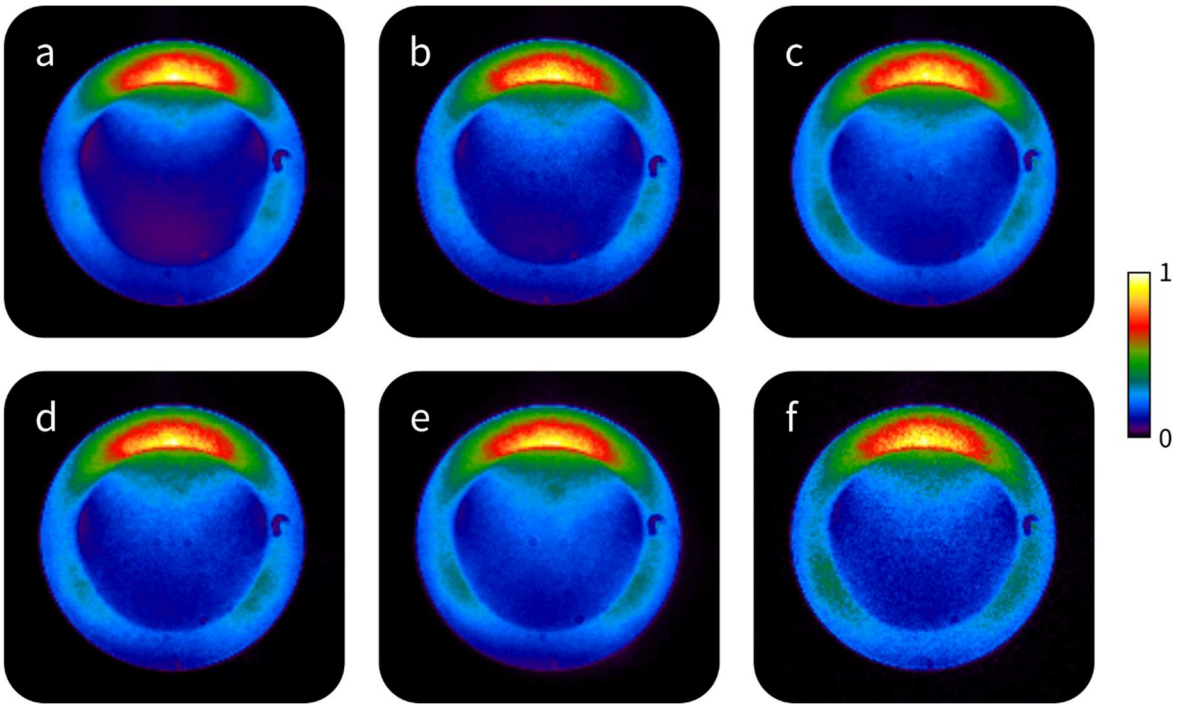

Figure 2.3 Back focal planes images of different antennas demonstrating the reproducibility of the directional emission patterns obtained by coupling quantum dots (QDs) to our nanoantennas. All the structures are 250 by 250 nm and have bridges between 40 and 70 nm and gaps between 35 and 55 nm, with the best experimental directivity coming from one measured (with a scanning electron microscope) to have a 50 nm bridge and 35 nm gap. Each measurement had a 10-second integration time and the QDs were excited by a circularly-polarized He-Ne laser at 633 nm with 10 μW of power. The maximum number of counts for each measurement nanoantenna is: (**a**) 131k, (**b**) 55k, (**c**) 86k, (**d**) 54k, (**e**) 88k and (**f**) 16k.

2.3 Multipole model

The far field emission pattern may be accurately represented by a superposition of multipolar point sources but we do not know *a priori* which multipoles are the dominant terms in our nanoantennas. To identify these terms we employ the finite-difference time-domain method (FDTD Solutions, Lumerical Inc.) with a SRR of the same nominal dimensions as in the experiment and a point electric dipole source positioned in the antenna gap where the electric near field is strongest. Using the formalism described in Chapter 1 (eq. 1.2-1.6) for the scattering of plane waves, we used the electromagnetic fields recorded on a spherical surface (radius of 10 μm) to calculate the moments of the electric and magnetic dipoles and quadrupoles. The multipolar moments which dominate the emission pattern are found to be an electric dipole on the *x*-axis (p_x), a magnetic dipole along the *z*-axis (m_z), two dependent electric quadrupole terms on the *x*-*y* plane ($Q_{xy} = Q_{yx}$) and two dependent magnetic quadrupole terms on the *y*-*z* plane. By calculating the radiated powers based on the multipolar moments [29], the first three terms radiate powers of similar magnitude and are each between one and two orders of magnitude higher than the *y*-*z* magnetic quadrupole; they are also at least four orders of magnitude higher than any of the other dipole or quadrupole components. Therefore, in subsequent modeling we only consider the dominant three components p_x, m_z and $Q_{xy} = Q_{yx}$.

The directional emission of the SRR antennas is adequately modeled by the interference of these three multipolar point sources radiating near a glass substrate [48-49]. We normalize their respective emissions so that each one radiates the same total power through the substrate. By varying the phase and amplitude of m_z and Q_{xy} with respect to p_x and propagating the total interference to the far field, we fit the pattern to the measurement using a non-linear least squares method (Fig. 2.2c). The interference between m_z and p_x is maximized when the phase is 0.5π or 1.5π, whereas a value of 0 or π prevents them from interfering. The interference between Q_{xy} and p_x behaves similarly. The best fit is obtained when all three components are considered, with amplitudes $|m_z| = 0.14$ and $|Q_{xy}| = 0.50$ and respective phases are 1.23π and 0.70π. An identical solution is found with phases of 1.77π and 0.30π, which are equidistant from the phases of maximum forward interference for m_z and Q_{xy}, respectively. In both cases, the phases of m_z and Q_{xy} cause them to simultaneously interfere with p_x constructively and destructively in the same directions. The moments extracted with this fit thus indicate that the measured directivity is primarily due to electric quadrupole-dipole interference, assisted to a lesser extent by magnetic-electric dipole interference.

The multipolar fit is in excellent quantitative agreement with the experimental observation, reproducing the experimental patterns in detail (compare Fig. 2.2a and 2.2c). The fit results also allow us to determine the directivity of the antenna by calculating its radiation outside of our NA and thus not detected in the experiment. The directivity is defined as the ratio of the power in a given direction over that of an isotropic source.[34] By taking into account the light radiated both into and out of the substrate, we find a directivity of 10.1 dB in the maximum direction. This value is comparable to the 10-14 dB directivities achieved with radio-frequency Yagi-Uda arrays [76].

2.4. Radiative rate enhancement

Next, we further demonstrate the robustness of this antenna design through numerical simulations by analyzing the performance of the SRR antenna with respect to changes in its dimensions as well as in the position of a local emitter around the antenna. We simulate a point electric dipole source located at different positions and orientations around the antenna structure which is on a substrate, unlike the previous simulations realized for the multipolar fit. We define the radiated power enhancement (RPE) as the total power radiated by the electric dipole coupled to the antenna normalized by the power radiated by an electric dipole in vacuum. This figure of merit is equal to both the increase in decay rate and the increase of the local density of states [77]. We find that the emission is greatly enhanced for an electric dipole located within the antenna gap and oriented across, in contrast with other positions and orientations (Fig. 2.4).

Given such drastic contrast in emission enhancement, we focus our analysis on emitters coupled to the uSSR from within the gap and polarized across it. We tune the structure's size parameter L (Fig. 2.1b); for L = 250 nm the center of the broadband enhancement region is aligned with the QD emission spectrum (red line in Fig. 2.5a and shaded area). For that antenna,

we systematically displace an *x*-polarized electric dipole source along the antenna gap and find that the radiated power is enhanced over a 200 nm spectral band for dipole positions covering two-thirds of the gap (Fig. 2.5b) while a source closer to the end of the gap has a much lower radiated power for wavelengths within the QD emission spectrum. Such widely distributed enhancement offers a large area and bandwidth for the QDs to couple to the antenna efficiently.

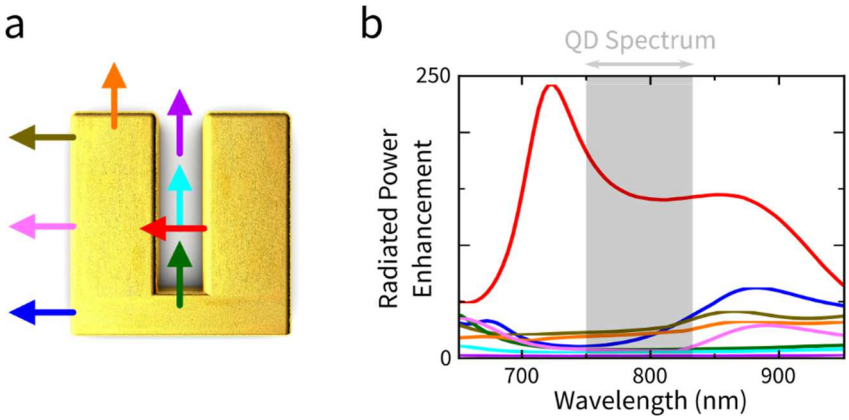

Figure 2.4 The radiated power enhancement of electric dipoles coupled to a uSRR from various positions and orientations. The size parameters are identical to those of Fig. 2.2. The radiated power enhancement (RPE) is defined as the power radiated by a dipole coupled to an antenna normalized by the power radiated by a dipole in vacuum. **(a)** A representation of the gold U-shaped split-ring resonator studied here and some of the different electric dipole positions and orientations studied. The distance between the emitter and the gold structure was kept constant. **(b)** The RPE spectrum for single electric dipole emitters coupled to the SRR from the color-coded positions shown in (a).

From these simulations we also calculate the system's external quantum efficiency to obtain 71% for an electric dipole emitter with 100% intrinsic efficiency at an optimal position (60 nm from the bridge) at the central QD emission wavelength. By combining this quantum efficiency with the previously obtained directivity, we estimate the average antenna gain [76] to be 6.8 dB in the case of a perfect electric dipole emitter with the broadband spectrum of our QDs.

Simulated electric and magnetic near fields have main components along the *x* and *z* axes, respectively, for a source at the same position 60 nm away from the bridge. The $|E_x|$ and $|H_z|$ field distributions (Fig. 2.5c) reveal a similarity to the third resonant mode in thin U-shaped SRRs [73-74, 78], here distorted for thick SRRs by the large arm widths and a narrow gap. At the third mode charge accumulates at the top of the arms, the bottom and in between, and this can been seen in Fig. 2.5b where the RPE near 720 nm peaks when the emitter is at the middle or top of the antenna gap. The wavelengths around this third-order mode of SRRs possess electric dipole and quadrupole scattering cross-sections of similar magnitude with a relatively small magnetic dipole contribution [47], in contrast with the first and second-order modes [79-80]. Accordingly, the distribution of $|H_z|$, with its two maxima out of phase, has no clear magnetic dipole moment (blue arrows in Fig. 2.5c). Related structures known as dolmens, with

separated arms and bridge elements, were also shown to have strong electric quadrupole-dipole interactions [81-82]. These observations confirm that the directivity of the SRR is mainly due to the interference of electric quadrupole and dipole moments.

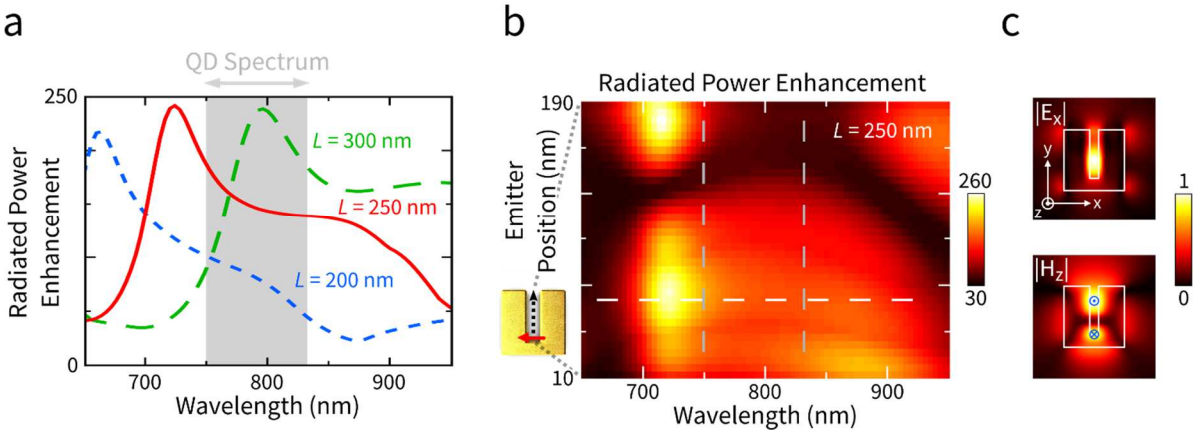

Figure 2.5 Broadband emission enhancement for emitters at different positions. The radiated power enhancement compared to a dipole in vacuum is analyzed as a function of antenna size and emitter position within the antenna gap. **(a)** By changing the antenna size parameter L (with b = 50 and g = 35 nm) for an emitter positioned 15 nm below the center of the antenna along the y-axis, the antenna spectrum can be tuned to the quantum dot emission spectrum (shaded region). **(b)** Power radiated by an emitter coupled to an antenna with L = 250 nm when displaced along the center of the antenna gap. The dashed vertical lines correspond to the FWHM of the QD emission spectrum and the horizontal line depicts the dipole position in (a) – red curve. **(c)** The electric near field is maximum when the emitter is located at that optimal position 60 nm from the bridge. The simulated distributions of $|E_x|$ and $|H_z|$ reveal characteristics of the third resonant mode of a SRR at the central wavelength of the QD emission (790 nm).

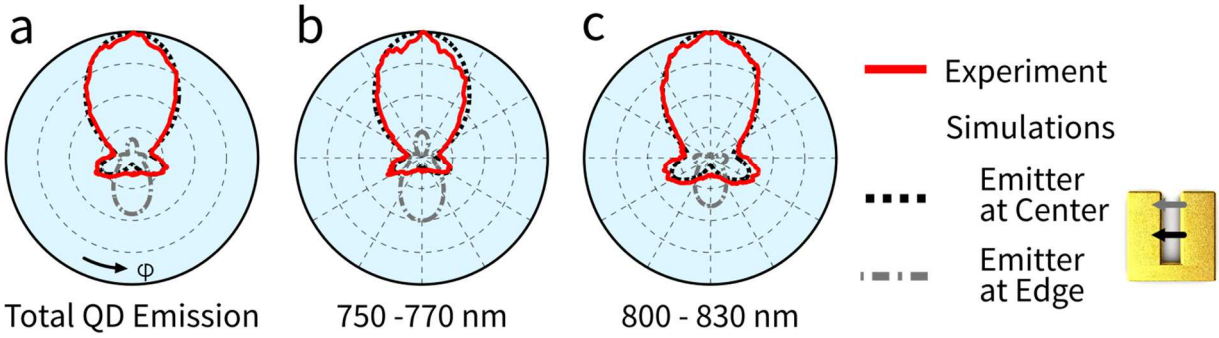

Figure 2.6 A comparison of experimental and simulated emission patterns. Azimuthal polar plots (φ = 0 to 360°) at the angle of maximum emission (θ = 43°) for two dipole positions (black and grey curves) compared to experimental measurements (red) at wavelengths between **(a)** 750 and 830 nm (the QD emission spectrum at FWHM), **(b)** 750 and 770 nm, and **(c)** 800 and 830 nm. The experimental measurement in (a) contains the entire QD emission spectrum and (b) and (c) were measured using spectral filters. The simulated patterns are weighted averages of different sections of the approximately Gaussian QD emission spectrum.

By comparing the measured angular radiation patterns to the ones obtained in FDTD simulations for sources at the center and edge of the gap (Fig. 2.6, dashed black and grey curves, respectively), we conclude that the operation of the antenna in our experiments is dominated by quantum dots located within the high field enhancement region of the gap. In contrast, when the dipole is located at the end of the gap (emitter position of 180 nm in Fig. 3b) the system emits predominantly in the backward direction (grey curves in Fig. 2.6a-c). However, due to our tuning of the SRR size to maximize directivity over the QD emission spectrum (which is slightly red-shifted from the third mode peak), the positions from which the system radiates in the forward direction have a much higher RPE than those radiating in the backward direction (Fig. 2.5b), and additionally, the emitter positions resulting in forward emission also cover a larger area of the antenna gap.

Regarding the spectral dependence of the directionality, the simulated radiation patterns indicate directional emission over a bandwidth of 200 nm for emitters at the center of the antenna gap. This broadband directivity has been decomposed in two different spectral bands, using filters. Figs. 2.6b and c show nearly identical experimental (red) and simulated (black) angular patterns for both bands. Regarding polarization, we note that for this emitter position the simulated *DOLP* of the antenna emission at these wavelengths is between 0.61 and 0.63, in good agreement with the experimental value of 0.60 and indicative of good coupling efficiencies between emitters and antennas. In conclusion, our simulations explain the origin of the experimentally observed robustness of the antenna directivity with respect to emitter position and wavelength.

2.5 Conclusions

With a more compact, more broadband and more robust single-element design, our multipolar interference antennas direct light emission comparably better than previously realized directional nanoantennas. The antenna has a footprint of only $\lambda^3/200$, the directional bandwidth is about 200 nm and there is no need to accurately position the emitters. Further tuning of the geometrical parameters or selectively positioning local emitters may result in higher directional and radiative enhancements. Interestingly, split-ring resonators may be patterned by simpler nanofabrication methods such as shadow-mask lithography because they do not require the alignment of multiple elements. Therefore, these results are promising for the integration of directional nanoantennas in light-emitting and harvesting devices.

From a fundamental point of view, understanding the directional response of a SRR is necessary to explain transmission and absorption spectra commonly found in experiments on metamaterials. For example, optical activity has been observed for achiral arrays of SRRs under oblique incidence [83, 84], which is a direct consequence of the multipolar origin of the directivity of a single SRR.

Chapter 3

Controlling the second harmonic generation from dipole antennas

Metal nanoantennas give a relatively strong nonlinear optical response due to the confined fields in the antenna hot spots. In general, nonlinear processes are forbidden in centrosymmetric media, so in plasmonic nanoantennas the surface contribution dominates over the bulk as symmetry is broken at the antenna surface. In this Chapter, we tailor the antenna resonance to the fundamental wavelength and measure the angular pattern of its second harmonic generation. We demonstrate that the second harmonic generation of a single dipole antenna resonant at the fundamental wavelength has a quadrupolar pattern in the second harmonic, and characterize them through both theory and simulations, which are in good agreement with the experiment. Our findings establish a basis for the controlled driving of coherent optical fields in nanoantennas, and for the understanding and development of innovative quantum nano-optical components and devices.

3.1 From quantum emitters to SHG

In the previous chapter we showed how one can control the emission direction of quantum dots through the use of plasmonic nanoantennas. Proper choice of antenna modes allow for certain radiation patterns to be achieved, with the interference of said modes being the source of directional emission. However, as such modes are static, controlled switchable bidirectional emission from such an antenna is not possible at a given wavelength. Furthermore, the positioning of emitters such as quantum dots at multiple antenna "hot spots" cannot typically make for a coherent interference as spontaneous emission, even when enhanced, is incoherent. As multiple single photon sources cannot interfere coherently, in this chapter we turn to a coherent process, specifically second harmonic generation (SHG), directly emitted by plasmonic antennas with the intent of controlling the phase of the antenna near field in excitation in order to manipulate the emitted second harmonic pattern of said antenna in the far field.

Plasmonics has been demonstrated to be of substantial use for increasing the efficiency of nonlinear optical processes [17, 85] as surface plasmon resonances can greatly enhance electromagnetic fields, and these processes have exponential dependencies on said fields. For example, Raman scattering can be enhanced by orders of magnitude to the point of single molecule Raman scattering becoming possible [86, 87]. Second (and higher order) harmonic generation from single nanoparticles has long been the topic of theoretical studies [88-97], and while much work has been done on metasurfaces and 2D and 3D arrangements of metallic particles [98, 99], the experimental studies of nonlinearities in single plasmonic objects has been more limited, though it is an expanding field [100-105]. The reason that the focus of many works has been mainly on enhancing nonlinear effects of arrays and not single antennas is because the signals from single plasmonic objects are usually extremely low and the objects under study may easily be destroyed before an appreciable signal can be detected. This threshold has started to be experimentally overcome in recent years through the design of antennas with double resonances that enhance both the fundamental and their harmonic fields [95, 95, 104]. However, despite the recent advances in this field, coherent control of the local phase of a nonlinear optical source [90] has yet to be experimentally demonstrated.

3.2 Single antenna SHG

In our experiments, in order to achieve a bright enough second harmonic signal while minimizing photodamage to the optical antennas studied, high peak power and low average power are required. If we consider two ultrafast laser pulses of the same energy, with, for example, 10 and 100 fs durations, the 10 fs pulse will give 100x more SH signal. To compress our broadband laser pulses to the Fourier limit we use the broadband laser and the pulse shaping process called MIIPS described in Chapter 1. As previously, our excitation beam is focused to a diffraction-limited spot with a 1.46 NA oil-immersion objective mounted in a confocal microscope, and the nonlinear emission of single antennas is collected in both the Fourier plane and the image plane.

To fabricate the nanorods we use e-beam lithography to define the antennas as described in Chapter 1. Next, we scan a sweep array of dipole antennas (Fig. 3.1a) where each column is nominally identical and the antenna length increases 10 nm with each row, from 110 to 240 nm. Both the antennas and the excitation polarization are oriented vertically. The first order (dipole) mode for our broadband laser spectrum corresponds to a length of 130 nm, and a height and width of 40 nm. We detect the nonlinear emission from single nanoantennas while exciting with a typical average power of 50-100 μW at the focus, which corresponds to a peak power density of 40-80 GW/cm^2. As the nonlinear emission of the antennas is predominantly the incoherent process of two-photon photoluminescence (TPPL), we filter it out (along with the excitation beam) using a 670 nm short-pass dichroic mirror, a 532 short-pass dichroic filter and a 390 nm band-pass filter with a FWHM of 50 nm. While this last filter blocks a small portion of our signal of interest (< 20%), it helps ensure the removal of all of the TPPL. Next, we select a resonant antenna from the third row from the bottom with a length of 130 nm and measure its emission spectrum and pattern (Fig. 3.1b-e). Notice the changes in both the spectrum and the emission pattern just by attenuating our laser with a neutral density filter OD 0.25, which corresponds to 1.78 times more/less light. The peak in the spectrum is over 4 times higher despite the fact that if it were purely SHG the change would be expected to be a factor of 3.16 (1.78^2) due to the exponential dependence of SHG. This is indicative that one or more higher order processes start dominating at higher powers [106-108]. Looking to the angular patterns, we see that at the lower power measurement (Fig. 3.1d) there seems to be an up-down pattern with a horizontal minimum crossing the center, whereas at the higher power (Fig.3.1c) there seems to be an omnidirectional and azimuthally symmetric pattern superimposing itself over the top and bottom emission lobes. If we suppose that the pattern in Fig. 3.1d is pure SHG, account for the theoretical increase in emission (a factor 3.16), and subtract it from the pattern in Fig. 3.1c, we obtain Fig. 3.1e. This pattern appears to be almost perfectly omnidirectional with no features worth mentioning aside from its symmetry. As each multipole has a clear angular pattern, an omnidirectional emission is a clear sign of incoherent emission, and we assume this one to be a result of three-photon luminescence and/or a cascade of effects sometimes referred to as white light super continuum. For the remainder of this Chapter we will avoid driving our antennas at such high powers so that we only observe SHG. Fortunately, any “leakage” from higher order processes is usually noticed quickly due to the brightness and omnidirectionality of the emission. Another sign that the antennas are being driven too strongly is the unstable but generally decreasing emission rate over time, which we understand to be due to directly damaging our antennas, either through melting, which depends on the average power, or through ablation, which depends on the peak power.

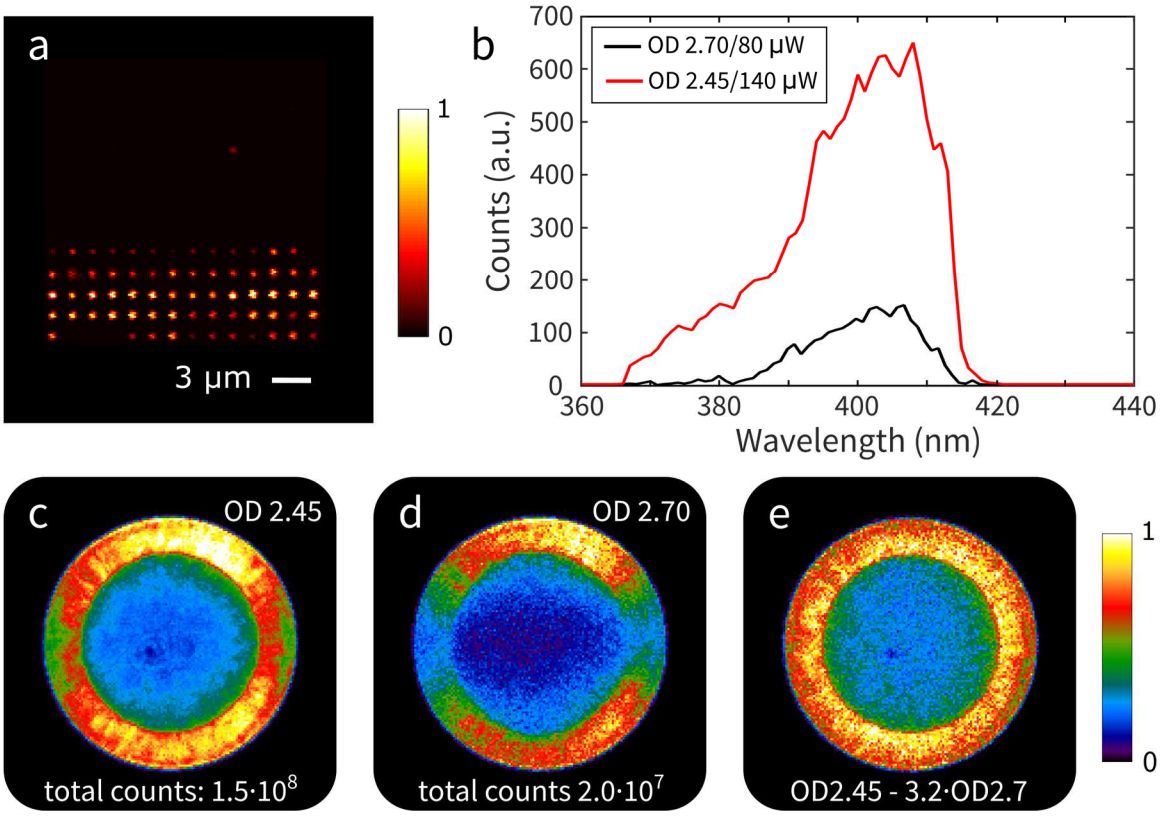

Figure 3.1 A first look at the nonlinear emission from Au dipole antennas. (a) A scan of an antenna sweep array in which every row is nominally identical and the antenna length increases 10 nm with each row, from 110 nm (bottom row) to 240 nm (not visible). The peak emission corresponds to a length of 130 nm, and both the antennas and the excitation polarization are oriented vertically. **(b)** The spectrum measured from a single 130 nm antenna while changing the incident power by a factor of 1.78. The peak increases by more than a factor 4 and not $1.78^2 = 3.16$, as one would expect from SHG. **(c-d)** The back focal plane (BFP) images corresponding to these two incident powers. At higher powers an azimuthally symmetric and omnidirectional emission predominates over the two up-down lobes that appear at lower power. **(e)** The difference between the BFP pattern (c) and 3.16 times (d), which is azimuthally symmetric.

Further measurements from an array of purely resonant antennas (Fig. 3.2a) reveal that we have no signal from anything but the antennas. Their relative brightness can vary more than a factor 2 from antenna to antenna, but all of them are visible in the second harmonic. BFP measurements from a number of them (Fig. 3.2b-f) show that their emission pattern is extremely consistent even if some of them are darker and/or less symmetric. We attribute this asymmetry to slight differences in the antenna apexes during nanofabrication [92]. They all show the same two emission lobes at the top and bottom and have a horizontal minimum across the middle. Note how, as the antennas are oriented vertically, the main emission lobes of BFP images are exactly perpendicular to where one would expect them to be if the emission were dipolar, as dipoles have their emission peak exactly perpendicular to the dipole axis. Figure 3.3a shows the angular pattern of a dipole and quadrupole radiating in free space. The rotational symmetry of the dipole (red) and quadrupole (black) give 3D patterns that are the known

"doughnut" for the former and a "diabolo" for the latter. Fig. 3.3b sketches half of the diabolo pattern to help visualize the quadrupole emission pattern in free space. As discussed in the previous chapter, when such emitters are placed near the interface of two materials of different refractive indices, the light predominantly radiates into the higher index medium with a peak near the critical angle, so in practice half of the diabolo shape is being refracted into the glass side of our glass-air interface.

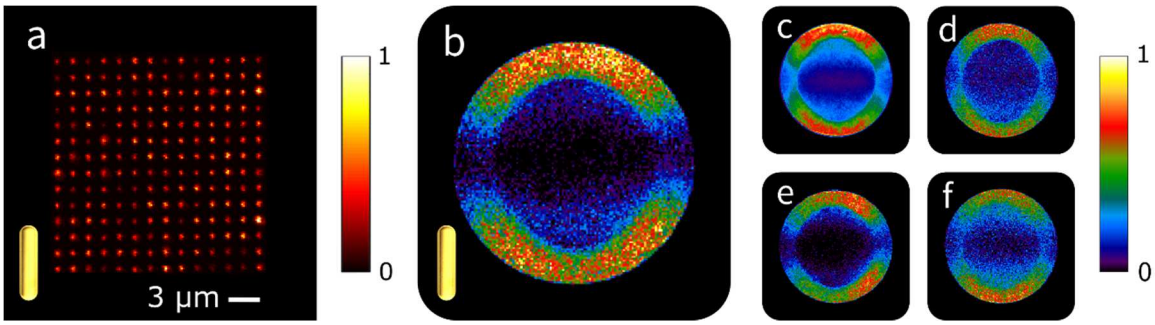

Figure 3.2 SHG measurements from an array of identical 130 nm antennas resonant at the fundamental. The antenna orientation and the excitation polarization are vertical. **(a)** A piezo scan of an array of antennas. While all of the antennas are clearly visible, their brightness can greatly vary, as their edge sharpness can be critical for brighter/darker SHG. **(b-f)** Angular emission patterns from five different antennas, each with an integration time of 10 seconds. Note how while some are brighter than others, and some have less symmetric emission lobes, but all of them generally show the top and bottom lobes with a horizontal minimum across the center.

We calculate the BFP pattern of a quadrupole next to a glass-air interface (Fig. 3.3c), and find that it is practically identical to the experimental patterns measured in Fig. 3.2. The four-lobed pattern in Fig 3.3a becomes only a two-lobed pattern in the BFP image in 3.3c because the top two and bottom two lobes are connected by the rotational symmetry shown in 3.3b, before being refracted into the glass side of the interface. The fact that the SHG from a single nanoantenna at its dipole resonance in the fundamental wavelength has a quadrupolar radiation pattern is a clear indication of the coherence of the process.

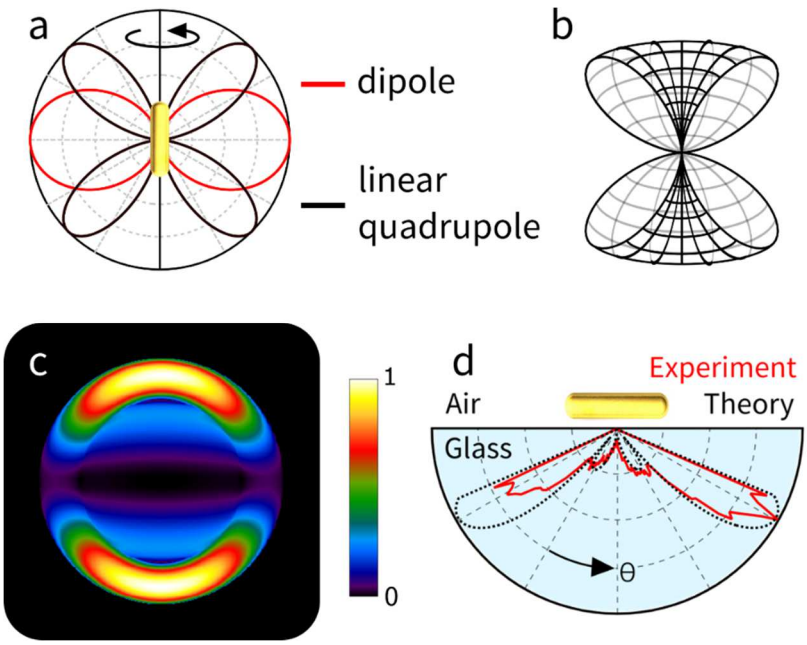

Figure 3.3 A closer look at the linear quadrupole. (a) A polar plot of the emission pattern of an electric dipole and an electric quadrupole, both oriented vertically, in free space. Note the rotational symmetry. **(b)** A 3D sketch of half the emission pattern of the quadrupole; the black lines denote the exterior and grey lines the interior. A full 3D pattern would resemble a "diabolo" toy with a top and bottom "cup". **(c)** The calculated BFP pattern of a quadrupole radiating at a glass-air interface. **(d)** A comparison of the experimental data and calculated quadrupole, which were obtained by calculating the polar coordinates of each point along a vertical line bisecting Fig. 3.2b and 3.3c.

The source of the quadrupolar SHG pattern

Generally, centrosymmetric media only have a non-zero $\chi^{(2)}$ at the surface where symmetry is broken, but this is only true in the electric dipole approximation, so higher order contributions may be possible [88, 89]. In the case of a dipole resonance, the electric near field has its strongest maxima at the surface of the antenna apexes, as well as a weak, relatively flat field that traverses the antenna. As the gradient of such a field is practically zero we will disregard the bulk in this Chapter.

The radiation pattern of a quadrupole is by definition that of two parallel dipoles arranged uniaxially and radiating exactly π out of phase, so we must consider the possibility that each end of the antenna is radiating like a dipole in the second harmonic and only interfering in the far field. Indeed, several of the surface $\chi^{(2)}$ terms give a SH dipole field that is dependent on $\hat{\mathbf{r}} \cdot |E_\omega|^2$, where $\hat{\mathbf{r}}$ is the vector normal to the surface. This means that for a rod antenna, two SH dipoles radiate exactly π out of phase due to their surface normals being antiparallel. However, it is also possible that the antenna, aside from being the emitter, can also act as a scatterer, and as the 130 nm Au rod has its $\lambda/2$ resonance at ω it might be scattering the 2ω photons close to its λ resonance.

To analyze this notion we use FDTD simulations. In them, we model the coverslip, the thin ITO layer, and the Au antenna according to experimentally measured parameters in a SEM. We then place a dipole emitter at one or both antenna apexes exactly at the Au-air interface, polarized along the antenna axis. When driven resonantly at the fundamental wavelength we see how the antenna "hot spots" are equally intense despite the fact that there is only one dipole on one side of the antenna (Fig. 3.4a). The phase map for the same case (Fig. 3.4d) shows that the two hot spots are almost exactly in phase as they are nearly the same color, with the slight difference being attributed to gold not being a perfect conductor. It may be confusing to the reader, but the hot spots being approximately in phase simply means that the field lines at each hot spot are parallel and in this case are pointing left as the phase is roughly π and $e^{i\pi} = -1$. This indicates that there is positive charge at the left apex and negative charge at the right. Between the two hot spots and along the antenna the phase is mostly 0, so the field lines there go from left to right, from the positive charge to the negative, as it should be.

Going down to SHG at a wavelength of 400 nm for the single dipole case (Fig. 3.4b), we find that the dipole is unable to drive much of a charge oscillation on the opposite antenna end as the field there is roughly one-sixth of the intensity around the dipole emitter. Finally we add the second dipole emitter on the opposite end to the first and have them radiate π out of phase. The 800 nm case is omitted because their destructive interference give nearly 0 fields. The appearance of a second field maxima along the antenna length (Fig. 3.4c) is generally indicative of a λ resonance. However, the hot spots at the apexes are actually weaker than the single dipole case (again, by about one-sixth), which means that they have an inefficient destructive interference. That fact indicates that the mode being driven has odd-parity, and is likely the $3\lambda/2$ (octupole) mode. Normally, the phase map (Fig. 3.4f) would be useful for identifying the mode, but the two π out-of-phase dipoles will always create a phase map that is completely antisymmetric. The mode would also normally be clear from the single dipole in Fig. 3.4b&e, but as the antenna quenches so much at 400 nm it is difficult to discern.

Thus, we take a more rigorous approach with the data we record in the simulation. We use two box monitors, each consisting of six planar power monitors, to record the power radiated by the dipoles, and a larger box encompassing the entire system to record the total radiated power. The total radiated power divided by the sum of the dipole powers gives the quantum efficiency (QE) of the system, assuming 100% efficient dipole emitters when they radiate in a homogenous non-absorbing medium. This figure of merit removes any wavelength dependent enhancements and allows us to compare and contrast the crosstalk of the dipole emitters at the antenna apexes.

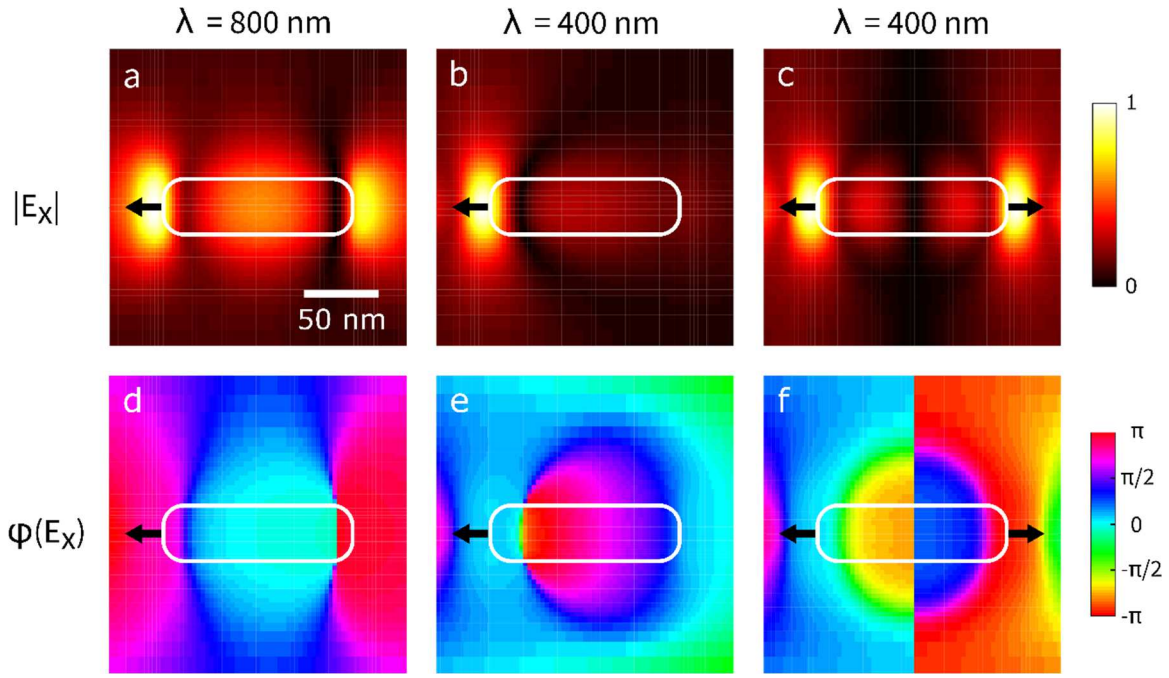

Figure 3.4 FDTD simulations of antenna near field at both the fundamental and the SH, when driven by one dipole emitter or two. (a-c) The near fields $|E_x|$ at the central fundamental wavelength of 800 nm (a), the central second harmonic wavelength of 400 nm (b), and the same wavelength when driven by two out-of-phase dipoles instead of one. **(d-e)** their respective phases in the same order.

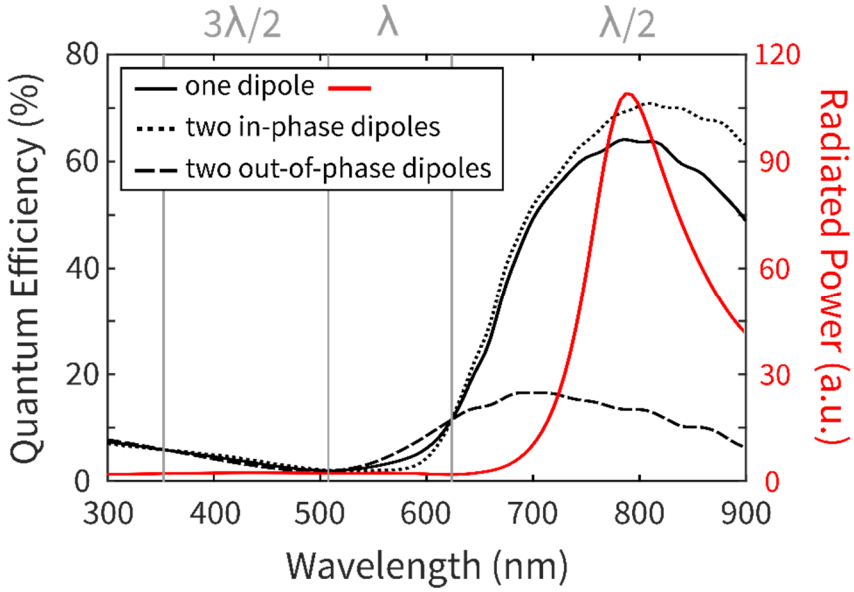

Figure 3.5 The quantum efficiency (QE) and radiated power of electric dipole emitters radiating from the apexes of a dipole antenna. The red curve is the radiated power spectrum of a single dipole coupled to the antenna. The solid black curve is the QE of that same dipole, the dotted curve is the QE of two in-phase dipoles, one at each apex, and the dashed curve is the QE of two out-of-phase dipoles, also at each apex. The vertical grey lines denote the mode of the antenna at those wavelengths, with the λ/2 (dipole) mode for λ > 625 nm, the λ (quadrupole) mode between 505 and 625 nm, and the 3λ/2 (octupole) mode between 350 and 505 nm.

In Fig. 3.5 - red we see what portion of light a single dipole emitter radiates to the far field when coupled to a nanoantenna nominally identical to the ones in our experiment. The large peak near 800 nm corresponds to the dipole resonance of the antenna, and as the curve quickly drops we find ourselves off resonance and in the region where gold is highly absorbing. The solid black curve corresponds to the QE of same case, while the dotted and dashed curves correspond to the QE of two in and out-of-phase dipoles, respectively. Note how at the dipole resonance, the two out-of-phase dipoles destructively interfere with one another, but as the wavelength decreases all three black curves cross over each other near 625 nm and the dashed line becomes the largest value. This is the wavelength at which they started constructively interfering, i.e., the λ resonance. These lines converge and cross again at 505 nm and at 350 nm, such that between 350 and 505 nm is the $3\lambda/2$ resonance, as was indicated in the analysis of Fig. 3.4, and below 350 nm is the 2λ resonance. The most important thing to note is that at wavelengths shorter than ~550 nm, the interference of the dipoles through the antenna is quite reduced, as can be seen by the close proximity of the dashed and dotted lines.

This demonstrates that the quadrupolar mode of our antenna, between 500 and 630 nm, is well outside our SHG spectrum (380-420 nm), and in fact would correspond to the antenna's $3\lambda/2$ (octupolar) mode. The angular pattern of this mode [49] was not observed in any of our measurements, and thus these results lead us to the conclusion that the radiation pattern is not generated by antenna's mode at the second harmonic wavelength. Thus, the experimentally observed pattern is due to the far-field interference of the two apex dipoles, and the role of the antenna after the second harmonic is generated, is that of a non-resonant and partially quenching scatterer.

3.4 Phase control

Now that we understand that SHG allows us to create phase-related dipole emitters at controlled nanometric distances, we can use this coherent property to control the phase of an antenna in order to change the angular pattern. To achieve this we fabricated a simple 2D structure, a cross antenna with each axis being a dipole resonant at the same excitation wavelength (Fig. 4.6a). The angular pattern of such an antenna will depend on the polarization of our excitation beam. If the cross is driven with linearly polarized light along either of the two antenna axes, then the expected radiation pattern is that of a linear quadrupole oriented along the polarization axis. If we excite with diagonally or circularly polarized light, we will drive both perpendicular components simultaneously, either in phase or $\pi/2$ out of phase. A phase difference of $\pi/2$ between the two antenna axes means that when one axis is at its field maxima, the other is at a current maximum and field minimum (in absolute value). As each axis radiates like a quadrupole, this change in phase between the two quadrupole emitters can reveal the four-lobe pattern seen in the back focal plane calculation shown in Fig. 3.6c, or suppress the lobes and achieve an azimuthally symmetric pattern (Fig. 3.6f). Experimental measurements reveal that indeed, we can control the relative phase between the perpendicular antenna elements through the careful manipulation of a quarter- and half-waveplate. The horizontal and vertical polarizations give exactly what was expected (Fig. 3.6 h-i), and the

diagonal (Fig. 3.6b) and circular polarizations (Fig. 3.6e) give imperfect but clearly identifiable patterns.

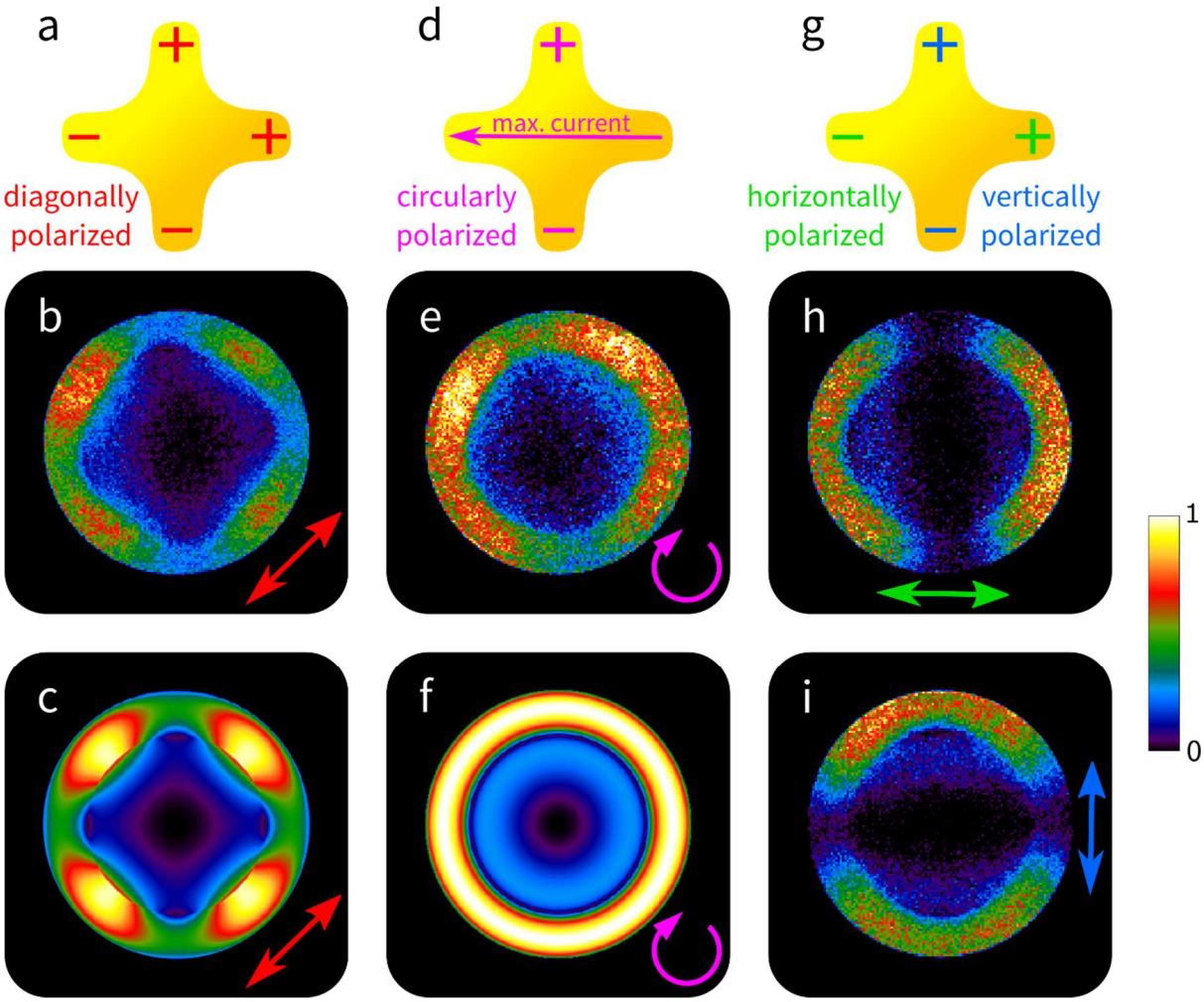

Figure 3.6 Controlling the phase of SHG to change the emission pattern of a single cross antenna. **(a)** A sketch of a cross antenna excited by diagonally polarized light and the resulting charge distribution. **(b)** The BFP measurement of SHG under the conditions described in (a). **(c)** The calculated BFP image of two perpendicular in-plane quadrupoles radiating in phase. **(d)** A sketch of a cross antenna excited by circularly polarized light and the resulting charge distribution. When the fields are maximum on one axis the current is maximum on the other. **(e)** The BFP measurement of SHG under the conditions described in (d). **(f)** The calculated BFP image of two perpendicular quadrupoles radiating $\pi/2$ out of phase. **(g)** A sketch of a vertically/horizontally polarized cross antenna and the resulting charge distribution. **(h-i)** The BFP measurements of SHG under the conditions described in (g).

As with the rods, the slight differences between the measurement and theory are attributed to imperfections in the fabrication process, particularly along the antenna edges from which the second harmonic is primarily generated [92]. Even within the linear quadrupole patterns, the two lobes generally have asymmetric intensities, thus finding an antenna with four identical edges becomes exponentially more challenging. Despite all of this, the 45° rotation of a broadband quarter-waveplate has a clear effect on changing the radiation pattern from a four-

lobe pattern in the back focal plane to a much more azimuthally symmetric one with its lobes becoming fused together.

3.4 Conclusions

In the context of nonlinear plasmonics, angular measurements combined with the multipole expansion are a powerful tool for understanding how coherent nonlinear processes occur and interact at the single antenna level, which may then be scaled up to metasurfaces [98 ,99]. Due to the nature of these processes, this may lead to interesting effects such as selective, directional coupling to waveguides [109-111], and for devices which may serve to produce or detect optical orbital angular momentum at the nanoscale [112-114].

In this chapter, we presented a detailed study of the second harmonic radiation patterns of Au dipole and cross antennas. These results provide a new path for devices requiring coherence for control, such as optical switches and optoelectronic interfaces, with ample opportunity for further enhancements through antenna design, material selection, and the use of other nonlinear processes. This use of coherent emission allowed us to gain an extra parameter of control over an often-static property of light emission with optical antennas - its phase.

Chapter 4

Second harmonic generation from crystalline silicon nanowires

When driving nonlinear process, plasmonic antennas are typically much brighter than non-metallic nanoparticles of equal size due to their ability to confine optical fields to nanometric volumes, but they are also highly susceptible to photodamage. Dielectric and semiconductors are not nearly as sensitive to this type of damage. As these materials can be pumped at much higher powers, they allow for the study of other, non-dominant, second order processes. In this Chapter, we measure and identify other, non-dominant contributions to second harmonic generation through their distinct angular emission patterns. These findings advance our understanding of different competing nonlinear processes and demonstrate a new application for angular imaging, the differentiation of the multiple origins of second harmonic generation.

4.1 From metal to semiconductor

High refractive-index nanostructures exhibit optical properties different from metallic nanostructures [61-66, 115-117]. While a surface plasmon propagates along the dielectric-metal surface due to its free surface electrons, in a dielectric or semiconductor the electrons are bound, allowing for local polarizability. The difference is that photons can propagate through both the interior and edges of a non-metallic geometry. In the case of a metallic nanosphere, driving it at its dipole resonance results in a charge oscillation back and forth from its poles (Fig. 4.1a). In contrast, the first resonant modes of a high-index sphere (Fig. 4.1b), light is reflected along its inner surface along the edge at oblique angles, often called a Whispering Gallery Mode [118], where the polarization of the impinging light defines whether the dipole moment of the resonance is electric or magnetic. For a sphere with a given refractive index and radius, its electric and magnetic dipole modes are at different wavelengths due to their different Fresnel coefficients for transverse magnetic (TM) and transverse electric (TE) incidence, with the electric dipole mode being at a shorter wavelength for a given refractive index [117]. Guided modes can also be excited with such materials, with their resonances depending on the size and shape of the medium.

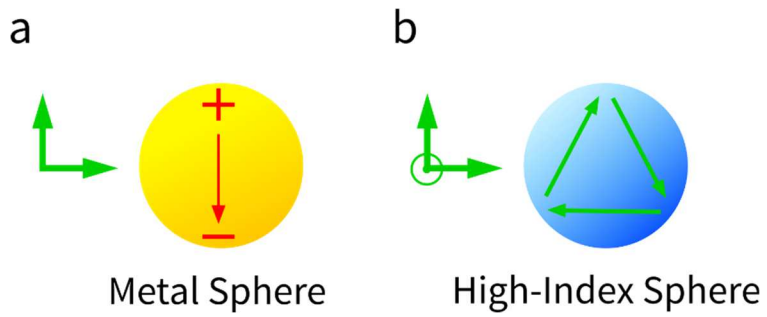

Figure 4.1 Schematic of the differences between resonances in metal and high refractive index spheres. The green arrows denote the polarization axis (in or out of plane) and the propagation direction. **(a)** Linearly polarized light induces a charge oscillation along the polarization axis of a metal sphere. **(b)** Linearly polarizaed light is reflected along the inner surface of a high-index sphere, with either in plane polarization (magnetic resonance), or out of plane polarization (electric resonance).

The main advantage of such high index materials with respect to plasmonic materials is their greatly reduced losses. High-index materials can be dielectric, but in the visible-to-near-infrared part of the electromagnetic spectrum, the materials used are more often semiconductors, so there are still losses if one is working with light with an energy equal to or above the band gap of the semiconductor. The extinction cross section of a metal nanosphere is much larger than that of a dielectric nanosphere of equal radius, so more light is absorbed per volume of material. Furthermore, in the metal particle, the losses are largely Ohmic and thus heat can rapidly damage it, in contrast, a semiconductor will re-radiate a larger portion of the absorbed light.

Similar to metal nanoparticles, second harmonic generation can also be obtained with semiconductor geometries, with the effects boosted by using their resonant modes [119-124].

Centrosymmetric media, such as single species crystalline semiconductors, have a vanishing second order polarizability in the electric dipole approximation, so any second order processes that they might have would be reduced to the surface contribution. While higher-order modes might also give rise to bulk SHG despite their centrosymmetry (eq. 4.1), typically the field gradients in dielectrics are quite small compared to metals. As these materials can be pumped at much higher powers, other relatively weak second order nonlinear terms may be observable. In recent years, the source of the largest contribution to SHG from single crystalline silicon has led to some controversial conclusions. Below is the second order nonlinear polarizability, divided into its surface and bulk terms.

$$\boldsymbol{P}^{(2w)}(\boldsymbol{r}) = \boldsymbol{P}^{(2w)}_{surface} + \boldsymbol{P}^{(2w)}_{bulk} \tag{4.1}$$

4.2 Underlying research on SHG of SiNWs

Here we address silicon nanowires (SiNWs) and the SHG measured from them. In the works of the Paillard Group in Toulouse, they studied the polarization characteristics of the SHG from SiNWs of varying dimensions [125-126]. They grew (111)-oriented nanowires with the vapor-liquid-solid method (VLS) and deposited them onto a glass coverslip. The wire lengths were typically 3-4 µm and the diameters studied were 50, 120 and 250 nm, but we will only focus on the thinner two wires, which can be seen in Fig. 4.2 (adapted from [126]). In Fig. 4.2a we see that the 50 nm wire cannot be detected in SH when excited with TE polarization (perpendicular to the wire axis), but does show SH when under TM polarization (parallel to the wire axis), and has the SH polarization parallel to the incident polarization. The 120 nm wire (Fig. 4.2b), however, has a clear signal under both excitation polarizations. In contrast with the 50 nm wire, when the 120 wire is excited with TM light it has a definite polarization component perpendicular to the excitation. To analyze these polarization properties, we decompose the second order nonlinear polarizability into the following components:

$$\boldsymbol{P}^{(2)}_{S} = \chi^{(2)}_{\perp\perp\perp}[\boldsymbol{E}^2_{\perp}]\widehat{\boldsymbol{e}_{\perp}} + \chi^{(2)}_{\perp\parallel\parallel}[\boldsymbol{E}^2_{\parallel}]\widehat{\boldsymbol{e}_{\perp}} + \chi^{(2)}_{\parallel\parallel\perp}[\boldsymbol{E}_{\perp}\boldsymbol{E}_{\parallel}]\widehat{\boldsymbol{e}_{\parallel}} \tag{4.2}$$

$$\boldsymbol{P}^{(2\omega)}_{bulk}(\boldsymbol{r}) = \gamma\boldsymbol{\nabla}\left(\boldsymbol{E}^{(\omega)}\cdot\boldsymbol{E}^{(\omega)}\right) + \beta\boldsymbol{E}^{(\omega)}\left(\boldsymbol{\nabla}\cdot\boldsymbol{E}^{(\omega)}\right) + \delta(\boldsymbol{E}^{(\omega)}\cdot\boldsymbol{\nabla})\boldsymbol{E}^{(\omega)} \tag{4.3}$$

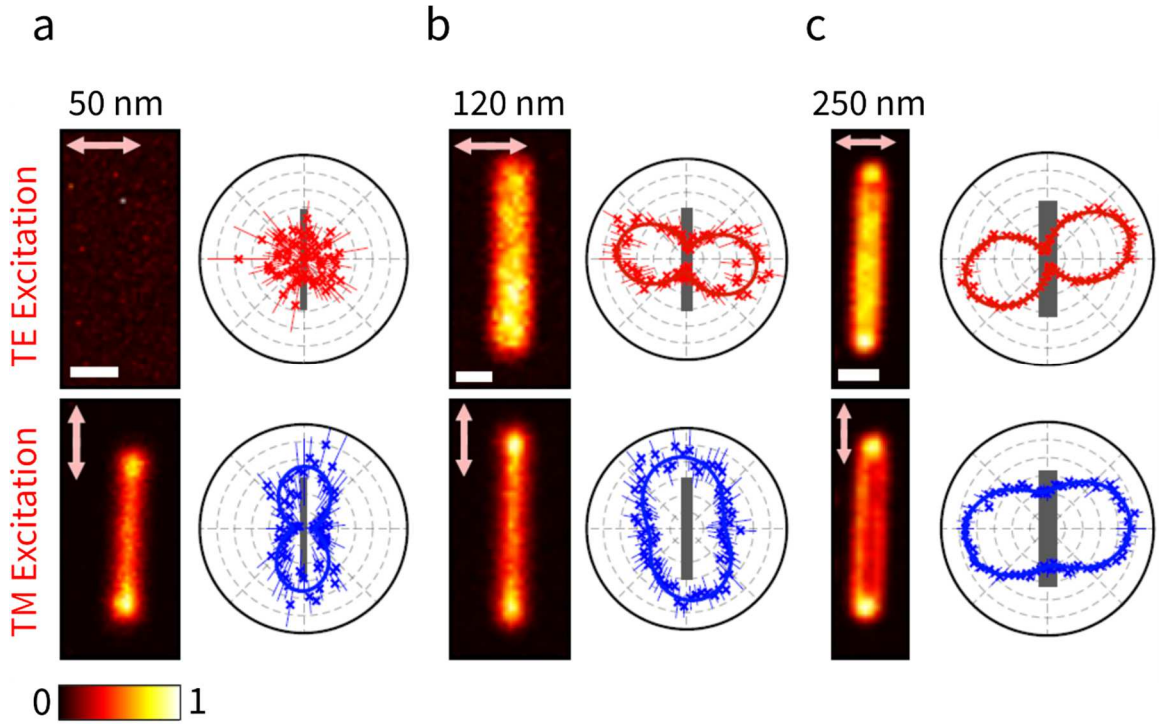

Figure 4.2 Second harmonic generation from silicon nanowires of various lengths, excited with light polarized perpendicular (TE) and parallel (TM) to the wire axis, and detected with an analyzer. TE and TM scans and polarization measurements of the second harmonic from a 50 nm wire (a), a 120 nm wire (b), and a 250 nm wire (c). The 50 nm wire has a SH polarization parallel to its axis when under TM excitation, but a perpendicular polarization component appears in the 120 nm wire, which then becomes the dominant component in the 250 nm wire. The white scale bars are 500 nm. Figure adapted from [126].

When under TE excitation (Fig. 4.2 - top), the electric field is perpendicular to the wire axis, $\widehat{\boldsymbol{e}_{\perp}}$, and it is clear that a SH polarization parallel to the excitation axis is the result of the first surface term, $\chi^{(2)}_{\perp\perp\perp}$. However, when the incident electric field is parallel to the wire axis, $\widehat{\boldsymbol{e}_{\parallel}}$ (Fig. 4.2 – bottom), the first and third terms in eq. 4.2 vanish and the remaining second term should give a SH polarization perpendicular to the wire axis. This is exactly the opposite of what was observed for the 50 and 120 nm wires (Figure 4.2 – bottom), so Paillard & collaborators expanded their study to the SH bulk components. Due to its surface-like behavior, the first term in eq. 4.3 can be included in the first terms of eq. 4.2 with an effective surface susceptibility [127-128]. We can also ignore the second term as $\boldsymbol{\nabla} \cdot \boldsymbol{E}^{(\omega)}$ vanishes in a homogeneous medium [129]. Thus, when under TM excitation the bulk is reduced to:

$$\boldsymbol{P}^{(2\omega)}_{bulk,TM}(\boldsymbol{r}) = \delta(E_z \frac{\partial E_z}{\partial z})\, \widehat{\boldsymbol{e}_z} \qquad (4.4)$$

where z is the direction along the wire axis. As this direction is parallel to the wire axis, this bulk contribution is the only component in agreement with the TM polarization measurements in Fig 4.2a-b. When the wire diameter is increased, the bulk contribution loses importance as

a polarization component perpendicular to the wire axis appears for the 100 nm wire (Fig. 4.2b – bottom) and then dominates in the 250 nm wire (Fig. 4.2c – bottom). The appearance of this contribution is attributed to the aforementioned second surface term ($\chi^{(2)}_{\perp\parallel\parallel}$) from eq. 4.2. The minimum in signal along the center axis of the 250 nm wire (Fig. 4.2c – bottom) also indicates that that this surface contribution is brighter than the bulk. These results are in agreement with previous work on the relative magnitudes of the different surface and bulk contributions [130].

Finally, Paillard et al. simulated the second harmonic fields within a nanowire and calculated the far field patterns expected from the $\chi^{(2)}_{\perp\perp\perp}$, $\chi^{(2)}_{\perp\parallel\parallel}$, and δ contributions from a horizontal silicon nanowire in vacuum (Fig 4.3 – also adapted from [126]). The SH near fields in Fig. 4.3a bear a resemblance to what one might expect from a plasmonic $\lambda/2$ antenna, but with its near fields much more spread out as if it were a "wide" antenna, with its spreading mainly defined by the width of the excitation spot. Due to this spreading, in contrast to the linear quadrupole pattern observed in Chapter 3, the expected angular pattern here would be that of several parallel in-phase electric quadrupoles, whose amplitudes decrease as one moves away from the excitation spot center, as denoted by the multiple white dipole arrows in Fig. 4.3d – top. A two-lobed, vertically polarized radiation pattern is the calculated result. A practically identical pattern is expected from the surface SHG in Fig. 4.3b. The bulk SH fields in Fig. 4.3c are comprised of two regions of opposite sign, as the slope of the excitation field changes sign when crossing the peak. This sign change is denoted by the two antiparallel dipole arrows in Fig. 4.3d – bottom. As such, the expected radiation pattern from the bulk is expected to be that of a linear quadrupole parallel to the wire axis.

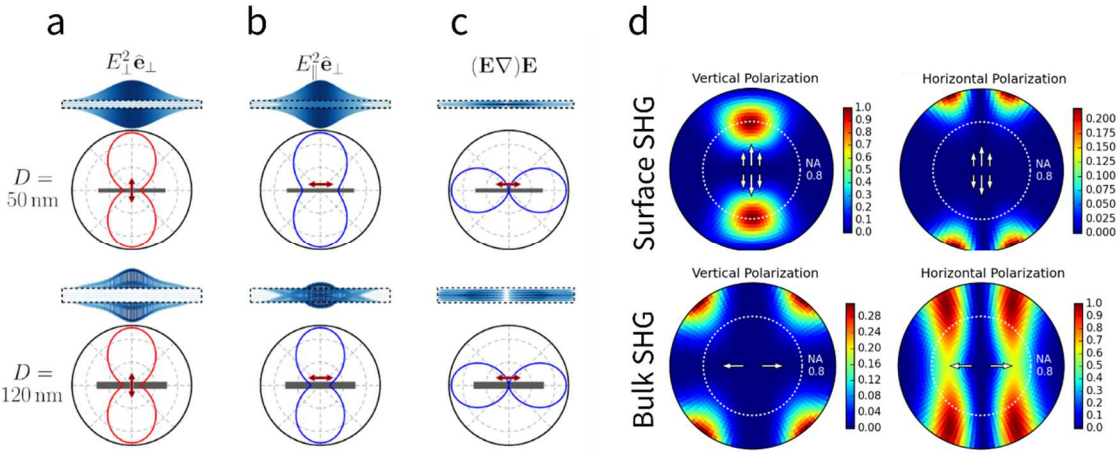

Figure 4.3 The simulated second harmonic fields from silicon nanowires. (a) The surface SHG under TE excitation. **(b)** The surface SHG under TM excitation. **(c)** The bulk SHG under TM excitation. Only a small section of the semi-infinite wire is shown. The red arrows denote the incident polarization and the polar plots are the far field polarization. **(d)** The surface (top) and bulk (bottom) far field patterns calculated from the near fields in (a) and (c). The white arrows denote electric dipoles, and thus the bulk contribution is predicted to be a linear quadrupole. The multiple dipoles from the surface are effectively multiple parallel electric quadrupoles that destructively interfere along the sides to suppress the side lobes that appear in the horizontal polarization of the bulk. Figure adapted from [126].

4.3 The angular patterns of 50 nm SiNWs

While the work of Paillard et al. [125, 126] is indicative of the presence of SHG from the bulk of narrow SiNWs, it has not been fully demonstrated. In the presence of multiple SH terms that spectrally overlap, polarization measurements are not the only way to distinguish them. In the coming sections we investigate samples of SiNWs with a diameter of 50 and 120 nm using BFP measurements. The angular patterns of each SH term are also a signature of their origin. Placing the 50 nm wire sample in our microscope, which is operating under the same conditions as in Chapter 3, we find that we are able to see them under both TE and TM excitation (Fig. 4.4), in contrast with Figure 4.2a – top. We attribute our much brighter signal to the smaller excitation spot size high NA oil-immersion objective, and more importantly, the shorter pulse duration of our laser with respect to theirs, ~15 vs ~100 fs, which in turn gives >40x more SH signal for the same average power. This not only allows us to detect previously undetectable SiNWs, but also produces enough signal to measure their angular emission patterns.

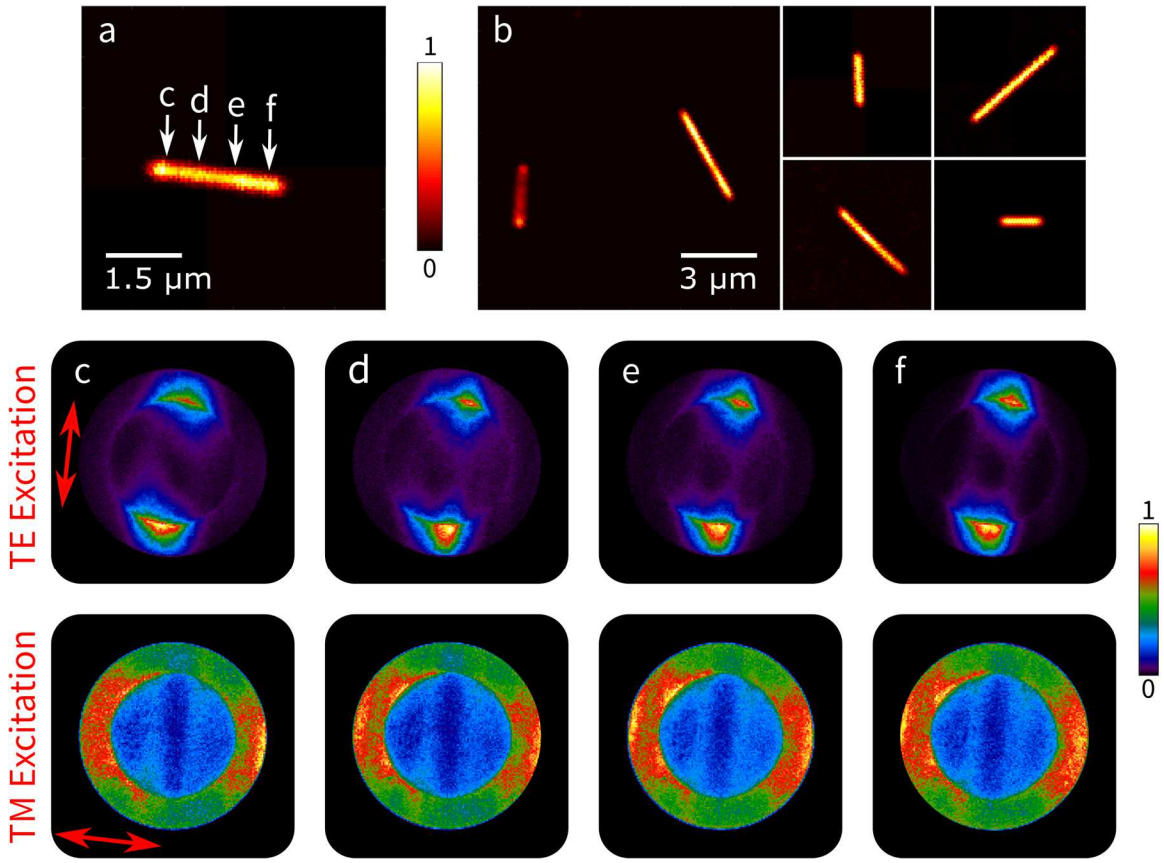

Figure 4.4 Second harmonic signal and back focal plane images from 50 nm silicon nanowires. The red arrows denote the excitation polarization and the white arrows indicate the position on the wire where each BFP image was measured. **(a-b)** Piezo scans of multiple wires of the same 50 nm diameters, but with varying lengths. **(c-f)** The back focal plane measurements of the wire in (a) with TE excitation **(top)**, and with TM excitation **(bottom)**, measured from the same positions. The measurements were taken from at least 300 nm away from the antenna apexes to avoid the surface contribution when exciting with TM polarization, and the TE measurements were done by sending 4 times more power into the microscope than for TM polarization.

The first observation is that the measurements do not change at all at when exciting the wire at different positions, which is indicative of the single crystalline nature of the wire. Polycrystalline silicon nanoparticles have been shown to have much brighter SHG due to their internal asymmetries [131], but each nanoparticle in that work is likely to have greatly different angular patterns due to their differing internal compositions. The measurements done under TE excitation (Fig. 4.4c-f TE) show patterns that are practically identical to the calculations done by the Paillard Group (Fig. 4.3d top), with two sharp radiation lobes oriented perpendicular to the wire axis and zero emission around these two lobes. This confirms the origin of the $\chi_{\perp\perp\perp}^{(2)}$ surface term. The measurements under TM excitation (Fig. 4.4c-f TM) resemble but are not identical to the predicted pattern in Fig. 4.3a. Like the SH quadrupoles studied in Chapter 3, there are two main lobes oriented along the wire axis with a minimum bisecting them, but the pattern is clearly not without several important differences. An omnidirectional background is present, and there are two extra minima vertically crossing the BFP pattern. This background is likely the result of a higher-order process (such as of three-photon photoluminescence) [106-108], but the minima are clearly interference fringes, which would not appear with an incoherent source. Such fringes can either be a result of multiple SH emitters radiating throughout the wire, or a resonance mode that the nonlinear emission has coupled to. When under TM excitation, we know of no physical reason that might justify the presence of a chain of SH dipoles emitting along the wire axis, as the field gradient is negligible everywhere except under our excitation spot (Fig. 4.3c). For this reason, we performed FDTD simulations to understand the modes in the wire and the scattering effects.

Using a total field scattered source to apply the method described in Chapter 1, we calculated the extinction cross section of the two wires for both excitation polarizations (Fig. 4.5). For a wavelength of 800 nm there are no resonance modes, but there is, however, a response near 400 nm for all of them, with the thinner wire overlapping better with our experimental SH spectrum. Then, taking the quadrupolar prediction from the Paillard group calculations, we place such an emitter within a 50 and 120 nm silicon wire and simulate the far field scattering pattern (Fig. 4.5b). The expected left-right lobes appear, though in the case of the 50 nm wire they are each split into 3 peaks. Signs of this 3-peak splitting are visible in the measurements (Fig. 4.4d-f TM). Furthermore, weak interference fringes also appear, despite their amplitude and spacing being different from the measurements, which is likely due to a difference in simulated wire length. Thus, we attribute the differences between the measured BFP image under TM excitation and the theoretical prediction to be due to resonant scattering in the wire and the presence of an incoherent higher-order process.

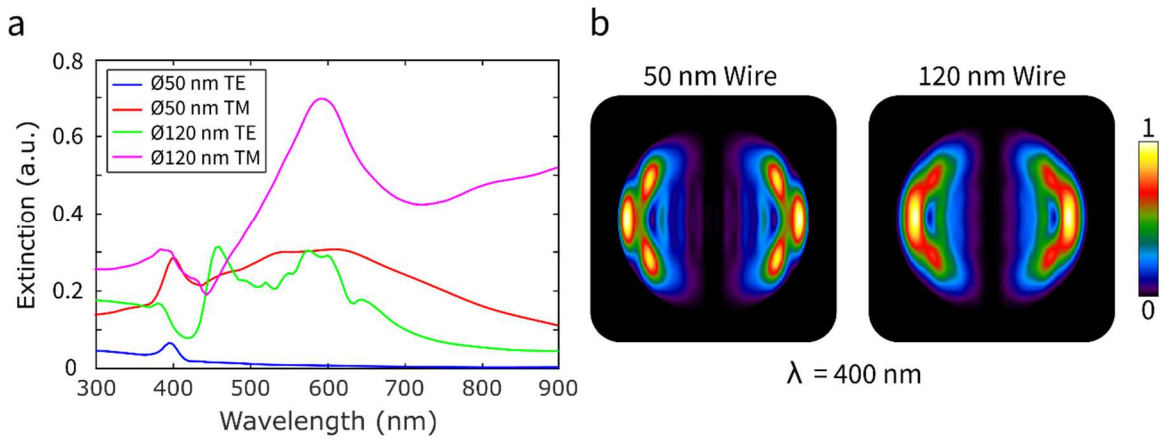

Figure 4.5 The simulated extinction spectra and far field patterns of two long silicon nanowires, with a diameter of 50 and 120 nm. (a) The extinction spectra for TE and TM polarization of both the 50 and the 120 nm wires. The extinction is normalized to the plane wave source. The blue and green curves correspond to an excitation polarization perpendicular to the wire axis (TE), and the red and magenta curves to an excitation polarization parallel to the wire axis (TM). Near the central excitation wavelength at 800 nm there are no resonance effects, however, each of the curves shows a resonance near 400 nm. **(b)** The far field radiation pattern of a quadrupole radiating inside a 50 (left) and 120 nm (right) silicon wire, oriented horizontally. The pattern is predominantly left-right, with each side having 3 main peaks in the 50 nm wire, that appear to fuse in the wider, 120 nm wire.

4.4 The angular patterns of 120 nm SiNWs

Next, we perform the same measurements on the nanowires with a diameter of 120 nm. As with the 50 nm wires, the SH angular emission patterns are practically identical across the wire (Fig. 4.6). For TE excitation (Fig. 4.6b-d TE), the angular SH pattern is once more confirms the simulations (Fig. 4.3d Surface), while for TM excitation the pattern is drastically changed. This change in pattern is a strong indication that another coherent nonlinear process is occurring, one that is brighter than the bulk contribution. In fact, each wire radiated SH mainly at the critical angle, with multiple sharp peaks around it (Fig. 4.6b-d TM). The main peaks positionally overlap with those that appear under TE excitation, which is the expected result from a $\chi^{(2)}_{\perp\parallel\parallel}$ contribution, which has a pattern similar to that of $\chi^{(2)}_{\perp\perp\perp}$. The secondary peaks oriented along the wire axis appear to be the result of a relatively weak bulk contribution. The simulated angular pattern from the bulk (Fig. 4.5b – right) shows that the three lobes from the 50 nm wire are fused together, which qualitatively explains the maxima parallel to the wire axis. In contrast with [126], when under TM excitation the surface contribution of the wire investigated is ~3x brighter than the bulk instead of ~2x darker. We attribute this difference to fabrication [92]. Another difference with respect to our measurements of the 50 nm wire is the lack of homogenous background. The narrower wire was driven with 1.6 times more light than the wider one when under TM excitation, and the resulting lack of background is indicative that the at this lower excitation power any higher-order processes that were present in the narrower wire are now comparable to the background noise.

To estimate the relative brightness of the SHG from the wires under TE and TM excitation, we integrated the total number of counts in each back focal plane image and averaged them over various beam positions over a wire. As the incoming intensity of our laser beam was constantly adjusted in order to not damage our emCCD, we must correct the counts accordingly (Table 4.1). We find that after compensating for the change in the laser intensity as well as the wire extinction cross-section, SHG from TM polarization decreases by about a factor 2 with respect to TE polarization on the 120 nm wires. This may seem to be a direct contradiction to the results in [126], but the distinct extinction spectra were not corrected for in that work.

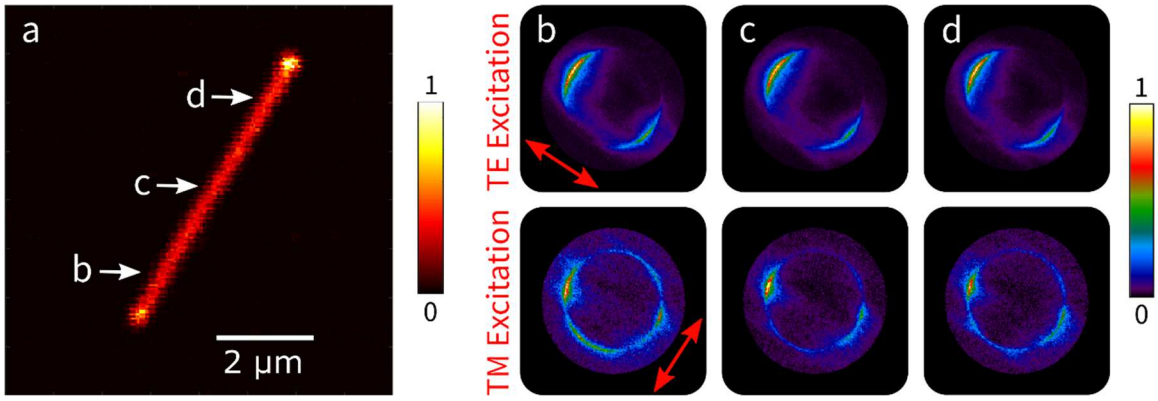

Figure 4.6 Second harmonic signal and back focal plane images from 120 nm silicon nanowires. The red arrows denote the excitation polarization and the white arrows indicate the position on the wire where each BFP image was measured. **(a)** A piezo scan of a wire with a diameter of the 120 nm when under TM excitation. **(b-d)** The back focal plane measurements of the wire in with TE excitation **(top)**, and with TM excitation **(bottom)**, measured from the same positions. The measurements were taken from at least 300 nm away from the antenna apexes to avoid the surface contribution when exciting with TM polarization.

As the BFP measurements of the 50 and 120 nm wires under TM excitation are so dissimilar, and the surface contribution from the narrower wire was not visible next to the bright bulk contribution, we must conclude that the bulk was suppressed via some mechanism. An increase in wire diameter may account for some of the suppression of the bulk SH as it is radiated from the center of the wire and the absorption coefficient of silicon dramatically increases at $\lambda < 500$ nm (and has a peak at 290 nm). However, simulations indicate that absorption cannot explain a difference greater than a factor 2. The presence of bulk SH in the two wires is due to the combination of both the wire geometry and the tight focus of our beam, giving rise to a strong field gradient, but the field profile within each wire is different due to their different sizes. Even the inefficient coupling to a mode can easily disperse the excitation fields within the wire and reduce the gradient, which we believe to be the case here.

Finally, in the values in Table 4.1, we overestimate the relative SHG efficiency in the 50 nm wire. If we consider that the decrease in relative efficiency is due to higher-order

processes and that $\chi^{(2)}_{\perp\parallel\parallel}$ and δ have similar amplitudes, they should each be about two orders of magnitude weaker than $\chi^{(2)}_{\perp\perp\perp}$, which is well in agreement with theoretical predictions [127].

	Average Counts (cts/s)	Extinction Cross Section (a.u.)	Corrected Counts (cts/s)	Relative SHG Efficiency (a.u.)
50 nm SiNW TM Excitation	$5.6\cdot10^{6}$	$1.6\cdot10^{-1}$	$8.9\cdot10^{7}$	TE is ~30 times more efficient than TM
50 nm SiNW TE Excitation	$3.4\cdot10^{6}$	$5.4\cdot10^{-3}$	$3.0\cdot10^{9}$	
120 nm SiNW TM Excitation	$6.0\cdot10^{5}$	$4.7\cdot10^{-1}$	$2.4\cdot10^{6}$	TE is ~60 times more efficient than TM
120 nm SiNW TE Excitation	$1.9\cdot10^{6}$	$5.5\cdot10^{-2}$	$1.4\cdot10^{8}$	

Table 4.1 A study in the number of counts measured with the emCCD. For each wire, the number of counts was measured at several positions and averaged, keeping away from the wire apexes. Bear in mind that with electron multiplication, it is not the real number of counts measured, but the numbers shown are proportional to the actual counts and to each other. As the SH signal was highly dependent on the wire diameter and the incident polarization, we adjusted the input excitation power with neutral density filters to avoid saturating the camera. The optical density (OD) attenuating our laser for each measurement was 1.7, 1.1, 1.6 and 1.3 for 50 nm TM, 50 nm TE, 120 nm TM, and 120 nm TE, respectively. The extinction cross-section was taken from Fig. 4.5a for a wavelength of 800 nm. The corrected counts corrects for the difference in excitation intensity and the extinction cross section of the wire. To do so, first we multiply the average counts by 10^{2N}, where N is the difference in optical density between the measurements. In the case of the 50 (120) nm wire, the difference was 0.6 (0.3), thus there was $10^{0.6} \approx 4$ ($10^{0.3} \approx 2$) times more incident power, which should give 16 (4) times more SH signal for TM excitation. Then we multiply the TE counts by the square of the ratio of the extinction cross section for TE and TM. The relative efficiency is an estimate on the how much more efficient SHG from TE and TM excitation is after compensating for the difference in cross-section and neutral density filters. We observe that the larger wires see a relative decrease in SH efficiency when under TM excitation, by about a factor 2, with respect to TE excitation.

In summary, our back focal plane measurements largely confirm the predictions made on the origin of second harmonic generation from these crystalline silicon nanowires. The predicted angular emission pattern from the bulk contribution was somewhat lacking in that it neglected to include the scattering effects of the silicon nanowire itself, but its contribution is still supported by our measurements and simulations. We also measured a drastic shift in angular radiation patterns when switching from 50 to 120 nm wires, which corresponds to the appearance of the parallel surface term that was observed by the Paillard et al. [125-126].

4.5 Conclusions

We have demonstrated the use of back focal plane imaging as a tool to identify different $\chi^{(2)}$ components in crystalline silicon nanowires due to their different polarization and angular symmetries. Typically, bulk contributions are neglected whenever second harmonic generation is discussed, but in the 50 nm wire geometry, its presence cannot be denied, particularly when tightly focused excitation beams are present. We further used FDTD simulations to show where theoretical predictions deviated from our measurements, and calculated the relative magnitude of three different second order terms. While exact estimates for their values were not provided here, that may well be the next step in advancing the state of the art.

Chapter 5

Switchable directional second harmonic generation from a single nanoantenna

By directing light, optical antennas can enhance light−matter interaction and improve the efficiency of nanophotonic devices. However, the optical antennas used generally have a passive directivity and do not allow for controling or switching of their emission direction. In this chapter, we exploit the coherent nature of second harmonic generation and control the interference between electric dipole and quadrupole moments of a single nanoantenna, exploiting both surface and bulk second harmonic, to switch its predominant emission direction. We experimentally demonstrate the operation of such an antenna, and provide insight on the origin of the directional emission through simulations and theoretical models. The advantages of the presented design bring directional optical antennas closer to practical applications such as optical switches and directional waveguides.

5.1 From linear to nonlinear; from incoherent to coherent emission

Single emitters such as molecules, ions or quantum dots generally emit as electric dipoles and, as shown in Chapter 2, when coupled to optical antennas their emission pattern changes to the emission characteristics of the multipole moments of the antenna. A limitation of such designs, e.g. the aforementioned SRR in Chapter 2, is that the relative amplitude and phase of each multipole is fixed. The coupling of more quantum emitters to such an antenna does not give a coherent interference between them despite their having similar or identical spectra and radiative decay lifetimes, as the emission is spontaneous, with dephasing time ~50fs, i.e. incoherent, and any phase relation between the emitted photons is lost. Coherent processes, do not suffer this limitation. Thus, one could think of directing scattering or stimulated emission, however both have the problem of the strong background dye to the excitation. Metallic antennas, with their strong field confinement, are efficient sources of non-linear response, such as SHG [88-104], third harmonic generation [100, 103], coherent anti stokes Raman scattering [132-135], etc. Here we will continue to work with SHG with the antenna as the intrinsic source, as the spectrally distinct SH is advantageous for background free detection, and of course as the SHG constitutes a coherent response which allows phase control.

In Chapter 3 we experimentally demonstrated dipolar antennas at the fundamental wavelength radiate as two exactly out-of-phase dipoles or a linear quadrupole at the second harmonic wavelength, often referred to as the E1 + E1 → E2 process. We also discussed how one might modify the phase between two such antennas when combined perpendicularly in a cross configuration. In this chapter, we exploit the potential of this coherent response to selectively switch the predominant direction of light emission at the second harmonic wavelength.

Directional interference

Generally, directional emission can be modeled in two distinct approaches: (1) as a point source multipole or (2) as a distribution of multiple electric dipoles. Both approaches are equally correct from a theoretical standpoint but provide distinct physical insight. For example, to perfectly recreate the emission pattern of a magnetic dipole, an infinite ring of in-phase electric dipoles is required in the multipole dipole model (Fig. 5.1).

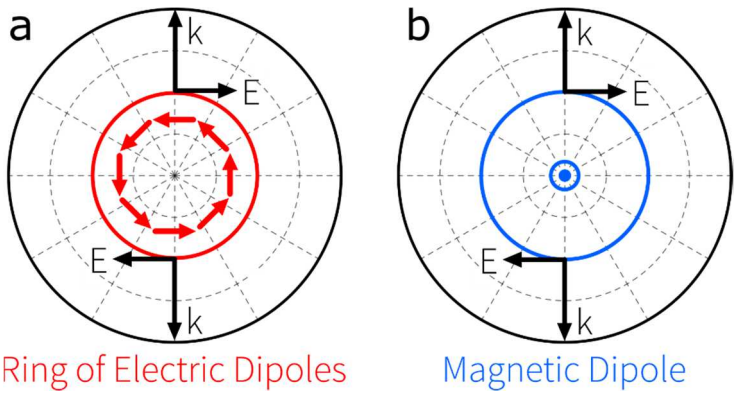

Figure 5.1 A comparison of a magnetic dipole from the multipole expansion and multiple electric dipoles. Red and blue arrows denote electric and magnetic dipoles, respectively. **(a)** The azimuthal emission pattern of a ring of in-plane electric dipoles radiating in phase. **(b)** The azimuthal emission pattern of an out-of-plane magnetic dipole. Note how the fields and k-vectors are identical.

If one is working with a complex single-element sub-wavelength antenna, such as the split-ring in Chapter 2, a multipole expansion is typically the best option as local fields can have multipole moments that are all centered around the same source position on the antenna. A multiple dipole model would also have worked, however would have required 5 dipoles (2 of which would be radiating in phase and 2 out of phase) to accurately represent one dipole plus one lateral quadrupole. If each dipole would have been radiating with an independent phase, then more multipolar components would have been required in the multipole expansion, and depending on the number of required components perhaps a multiple dipole model would have been a better representation. On the other hand, if one considers a multi-element antenna, such as a phased-array or a Yagi-Uda array of dipoles [50], with their lengths and positions tuned for directional interference, then clearly a multiple dipole model makes more physical sense. In designing a phase-controllable directional SHG antenna, we will exploit the interference of different multipoles, and take into account that the emitted SH is proportional to the vectorial product of two local fields. Here we will discuss the concepts of wire antennas, multipolar antennas, magnetic transitions and quadrupolar modes, local field gradients and surface versus bulk second harmonic.

Wire antenna: multiple dipoles.

As phased arrays of dipoles are capable of unidirectional emission, how would such a concept work in the second harmonic? Taking, for example, the Yagi-Uda antenna, one must note that each dipole radiates as a linear quadrupole in the second harmonic with its emission being a zero exactly normal to the dipole axis. Such a configuration can work in SHG if all of the rod elements are within our laser excitation spot. The directionality of the Yagi-Uda stems from the different length of each dipolar element having a slightly different phase. As this is a passive effect that geometry is unviable towards our goal of controllable directionality.

Another geometry is the wire antenna, which in the linear regime is one of the most directional and broadband plasmonic antennas [57, 136-139]. The mode of operation of such an antenna is that of a phased uniaxial array of electric dipoles, with a correct spacing and dephasing. For this one needs a wire long enough for a propagating surface plasmon to decay without being back reflected. It is excited optically at one end to launch the plasmon, and the material losses create a constantly decaying amplitude and phase shift from one hot spot to the next. As each hot spot radiates like an electric dipole, together their far field interference creates a unidirectional emission. A perhaps unexpected attribute of this mode of operation is that it is possible to achieve directional emission for all dipole orientations [57], as long as they are all parallel to each other and arranged uniaxially. While this method of operation is highly directional, implementing it with SHG is not without its issues. For example, the necessary dephasing of a propagating plasmon along the wire is disastrous for our broadband excitation, which requires in-phase photons to give a visible SH signal. To overcome this issue, we must first analyze the multiple mechanisms that can give rise to SHG.

5.2 Multipole expansion of SHG: electric dipole, quadrupole, magnetic dipole, field gradients

Generally, in nonlinear optics, following the conventional dipole approximation, SH require non-centrosymmetric media. For centrosymmetric media, only the symmetry-breaking surface contributions are considered. Yet outside the dipole approximation, bulk components may also contribute even in centrosymmetric media, with the next order terms being electric field gradients and magnetic dipole moments. The non-linear polarization has extra "non-dipolar" terms generally omitted. Repeating the equations from Chapter 4, the second harmonic polarizability is as follows:

$$\boldsymbol{P}^{(2w)}(\boldsymbol{r}) = \boldsymbol{P}^{(2w)}_{surface} + \boldsymbol{P}^{(2w)}_{bulk} \tag{5.1}$$

$$\boldsymbol{P}^{(2w)}(\boldsymbol{r}) = \overleftrightarrow{\boldsymbol{\chi}}^{(2)}_{s} : \boldsymbol{E}^{(w)}(\boldsymbol{r})\boldsymbol{E}^{(w)}(\boldsymbol{r}) + \overleftrightarrow{\boldsymbol{\chi}}^{(2)}_{b} : \boldsymbol{E}^{(w)}(\boldsymbol{r})\boldsymbol{\nabla}\boldsymbol{E}^{(w)}(\boldsymbol{r}) \tag{5.2}$$

In bulk optics the higher order terms can be ignored, however in nanoplasmonics, with structures of subwavelength dimensions and fields confined on subwavelength scale, the dipole approximation reaches its limits and such higher order terms do become important. With the right geometry and/or excitation conditions, one may engineer an increased importance of the non-dipolar terms, which may be surface or bulk. Note that bulk SHG may appear in centrosymmetric media outside of the dipole approximation, that is to say, if field gradients and magnetic contributions are considered. Amongst these possible terms, there is the E1 + M1 → E1 and the E1 + E2 → E1 processes, and both processes can potentially originate in both the surface and bulk of the medium. Thus, here we aim to exploit these terms by engineering an antenna such as to give it a strong magnetic field or electric field gradient within its surface and/or bulk, such that it becomes be possible to engineer different sources of SHG, and tentatively control their mutual interference in generating the second harmonic. The surface

and bulk contributions are decomposed in equations 5.3 and 5.4 below.

$$\boldsymbol{P}_S^{(2)} = \chi_{\perp\perp\perp}^{(2)}[\boldsymbol{E}_\perp^2]\widehat{\boldsymbol{e}_\perp} + \chi_{\perp\parallel\parallel}^{(2)}[\boldsymbol{E}_\parallel^2]\widehat{\boldsymbol{e}_\perp} + \chi_{\parallel\parallel\perp}^{(2)}[\boldsymbol{E}_\perp \boldsymbol{E}_\parallel]\widehat{\boldsymbol{e}_\parallel} \tag{5.3}$$

$$\boldsymbol{P}_{bulk}^{(2\omega)}(\boldsymbol{r}) = \gamma\boldsymbol{\nabla}\left(\boldsymbol{E}^{(\omega)} \cdot \boldsymbol{E}^{(\omega)}\right) + \beta\boldsymbol{E}^{(\omega)}\left(\boldsymbol{\nabla} \cdot \boldsymbol{E}^{(\omega)}\right) + \delta(\boldsymbol{E}^{(\omega)} \cdot \boldsymbol{\nabla})\boldsymbol{E}^{(\omega)} \tag{5.4}$$

Each of these components allow for what can be categorized as electric dipole (E1), magnetic dipole (M1) and electric quadrupole (E2) transitions in the fundamental that give electric dipole and quadrupole emission in the second harmonic [88-89, 140]. The typically most basic and efficient process, E1 + E1 → E1, is purely dipolar and in this case is forbidden due to the symmetry of the problem. The E1 + E1 → E2 process is allowed from all of the surface components. The E1 + M1 → E1 process is only forbidden from the $\chi_{\perp\perp\perp}^{(2)}$ component, but is allowed in all of the others. Finally, the E1 + E2 → E1 process is allowed by all of the components.

The magnetic dipole contribution

First, we consider the magnetic contribution from the E1 + M1 → E1 process. While the second harmonic mechanisms are given in purely electric field terms, the magnetic transition comes from the curvature of electric fields that are arise from a net magnetic dipole moment. Given that there is no known naturally occurring material that has a non-unity relative magnetic permeability at optical frequencies, plasmonic resonances in ring-like structures such as the split-ring resonator (SRR) must be considered. Using the SRR as a first-order mode (Fig. 3c), one immediately encounters several problems. The first is that the magnetic field maximum is outside of the antenna volume and within the hole in the ring. The second is that the surface SHG would be “silenced” due to the narrow gap. Silencing is the result of the proximity of the two surfaces within the gap radiating as out-of-phase dipoles, similar to the rods in Chapter 4, but with a greatly reduced distance, typically from ~130 to ~15 nm. As the moment of a linear quadrupole is dependent on the distance squared of the two out-of-phase dipoles that it is comprised of, such a moment becomes 75 times darker in this example. This is more than enough to counter any possible gains from increased local field enhancements, as they are typically a factor 5 or less when compared to a single rod. Thus, antenna gaps must be avoided if a surface second harmonic signal is desired. The fabrication of SRRs resonant in the visible-to-near infrared range is also challenging due to the small antenna size, but not impossible with current fabrication techniques, such as focused ion beam milling with a helium source. The other issues can be addressed by widening the gap of the split-ring. A semi-circle or V-like geometry are both capable of increasing the distance of their electric hot spots as well as shifting the location of the magnetic field maxima closer to the edge of the plasmonic material. However, this comes at the cost of a reduced magnetic response. Adding a nonlinear material to the antenna gap may also give SHG a medium in which the magnetic transition can occur. Assuming that such a nonlinear magnetic transition is of the same order as the electric transition at the antenna apexes, the concept of directional dipole-quadrupole interference becomes

feasible, though without any phase control as the magnetic and electric field maxima have a static phase difference defined by the antenna geometry. A static phase difference is, unfortunately, precisely what we wish to avoid as our interest lies in active control over the antenna's emission direction.

The electric quadrupole contribution

Next, we consider the E1 + E2 → E1 process. In the case of a rod antenna with its first order dipole resonance excited at the fundamental wavelength, it will have a maximum electric field when the positive and negative charges are localized at the antenna apexes. The quadrupole transition at the surface refers to antiparallel SH dipoles that appear around the cross section of the rod (Fig. 5.2). Given that the orientation of each SH dipole is necessarily normal to the surface, for the cross section of a cylinder in free space, its SHG will be a sum of infinite quadrupoles around the antenna center, which gives a zero net emission. While the cross section of a fabricated antenna rod is not quite circular, and may have a slightly asymmetric charge distribution, these perturbations are still negligible, as they did not appear in the measurements in Chapter 3. Furthermore, it is impossible to achieve directional interference with the E1 + E1 → E2 process as a dipole perpendicular to a linear quadrupole cannot interfere directionally due to their field symmetries.

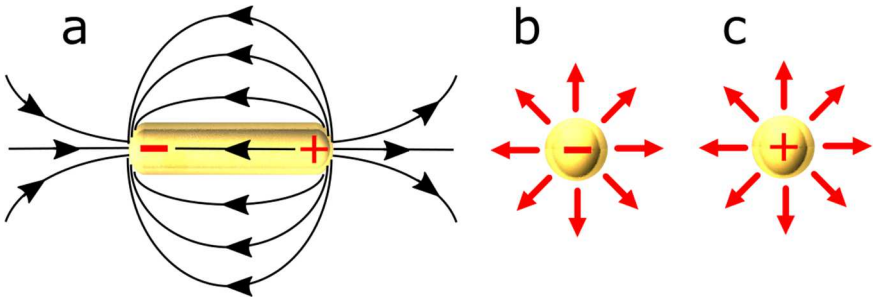

Figure 5.2 Electric fields of a dipole antenna and SHG from surface contributions orthogonal to the antenna axis. (a) A sketch of the charge distribution and resulting electric field lines of a dipole antenna. **(b)** A sketch of SHG surface dipoles at the cross section of the side of the antenna with negative and **(c)** positive charge. Note that their orientation is independent of both the sign (direction) of the electric fields, this is a result of their orientation depending on the direction of the surface normal.

The bulk terms β, γ and δ in equation 5.4 also permit the E1 + E2 → E1 process, but they depend on electric field gradients. If we take a simple dipole antenna as an example, with a positive-negative charge distribution at the antenna apexes as in Fig. 5.2a, the electric field is maximized at the antenna apexes, while within the antenna volume there is a weak field maximum in the middle of the rod. The field gradient at this central peak is zero, and with its maximum/minimum at the inflection points midway between the antenna center and its apexes. As in Chapter 4, these inflection points correspond to different sides of the slope, and the gradients have opposite signs creating a quadrupolar pattern. In contrast with the

semiconductor wires, in metals the fields do not penetrate the antenna volume well, and the bulk terms will be multiplied by relatively weak values [141-142]. One antenna geometry that attempted to maximize the gradient effects was studied within the group, specifically, the geometry called a “dumbbell antenna”, shown in Fig. 5.3b. This antenna is essentially a rod with widened apexes and a narrow body, with the intention of diffusing the surface charge at the apexes and reducing surface SHG, while maximizing the interior fields within the narrowed region along the antenna body to promote bulk SHG. Previous research on silicon indicates about a 100x difference between surface and bulk contributions [130], and our data show indications of a bulk SHG contribution in aluminum, with perhaps a 50/50 ratio with respect to surface SHG, but it is an indirect interpretation, and the work is still unpublished.

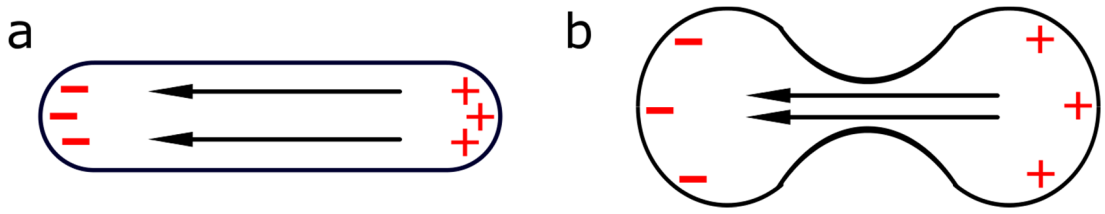

Figure 5.3 A qualitative comparison between a dipole and dumbbell antenna, with their charge distribution and current lines shown. (a) A dipole antenna and **(b)** a dumbbell antenna. Note how the charge is more dispersed at the dumbbell antenna apexes with respect to the dipole, and how its current lines are closer.

An alternative method to create (strong) field gradients is to use the laser field directly from our excitation beam, instead of the modal field inside the antenna. Clearly, if the diffraction-limited Gaussian excitation spot is centered on an antenna then any bulk contribution will quickly vanish as it did with the dipole case, but if one displaces the excitation beam such that about half of the laser spot is over the antenna, only one of the slopes of said spot will be over the antenna. Furthermore, if the beam is over one half or the opposite half of the rod, those field gradients will have opposite signs, giving a certain level of control. Plasmonic dipole antennas that are resonant with our excitation beam (750-860 nm) are around 130 nm in length, which is less than half the size of our diffraction-limited spot size (about 280 nm at FWHM), and will be overlapped with the excited field that is considerably more extended. A longer, higher order, resonant antenna, such as a λ or $3\lambda/2$ antenna are both better matched in size with respect to our laser spot, have less intense hot spots, and are more suitable to drive a local asymmetric gradient field in the antenna.

In general, odd parity modes such as the dipole ($\lambda/2$) and octupole ($3\lambda/2$) modes are often referred to as bright modes, and even parity modes such as the quadrupole (λ) mode are referred to as dark modes. This stems from the fact that even parity modes have a net current of zero at any given moment and cannot be excited by, for example, a plane wave. In order to light up a dark mode some method must be employed to break its symmetry, such as localizing a quantum emitter in the near field of one antenna apex of a λ antenna. While the excitation enhancement of such an emitter may be small under plane wave excitation, the presence of the

emitter itself breaks symmetry and it will radiate in the antenna's quadrupolar mode with a corresponding emission enhancement. In the case of SHG from a λ antenna resonant at the fundamental wavelength, as the emitter is the antenna itself, one must use an alternative method of breaking symmetry, such as asymmetric excitation on one side of the rod axis.

5.3 Directional SH emission from quadrupolar λ antennas

Here we propose to use λ antennas and scan our diffraction-limited excitation spot with respect to the center of our antennas. This approach has the combined advantage of exciting a λ antenna by breaking symmetry, as well as creating a non-zero field gradient when integrating over the antenna surface and volume. The same experimental setup used in the previous chapters was also used here. Gold rod antennas with the λ resonance centered near 800 nm are around 290 nm in length. Our excitation spot size (in intensity), given our NA of 1.46 and a central wavelength of 800 nm, is diffraction-limited and measures ~280 nm at full-width at half-maximum (FWHM). A priori one would expect that moving the spot about halfway off the antenna with respect to its center would enable us to drive the λ mode, as one would strongly be exciting half of the antenna and weakly exciting the other half. Simulations shown in Fig. 5.4a demonstrate that absorption is maximized for a displacement of 200 nm (magenta, solid), but is relatively stable between 150 and 250 nm, and that each curve decreases as the spot is moved off of the antenna. Notice how there is no peak when the beam is centered on the antenna (0 nm displacement – black curve), as the quadrupolar mode cannot be driven in the symmetric condition. A near electric field map (Fig. 5.4b) reveals that it is a dipole mode driven far off-resonance as there is almost no field at the antenna apexes despite our beam spot being right on top of it. Once the beam is moved off-center, a peak with quadrupolar fields in the fundamental immediately emerges (Fig. 5.4c) and the tell-tale signs of an antenna resonance, its hot spots, become visible. For a plane electric field monitor a few nm away from antenna, a dipole resonance will show three local field maxima, two just outside its apexes and one in between, so the presence of a second field maximum between the antenna (Fig. 5.4c) apexes is clearly the result of a quadrupole resonance.

We characterize the nonlinear emission of the antennas with a confocal microscope with two detection branches corresponding to real and momentum space imaging. A high-numerical aperture oil-immersion objective (1.46 NA) is essential for angular detection as most of the emission is radiated beyond the critical angle of the air-glass interface. The excitation and incoherent two-photon photoluminescence (TPPL) is separated from the SHG with a 670 short-pass dichroic mirror, a 440 nm short-pass filter and a 390 nm band-pass filter. For confocal detection, in real space, an avalanche photodiode is used. For momentum space imaging, in the Fourier plane, we record images in the back-focal plane (BFP) of the objective using an EMCCD.

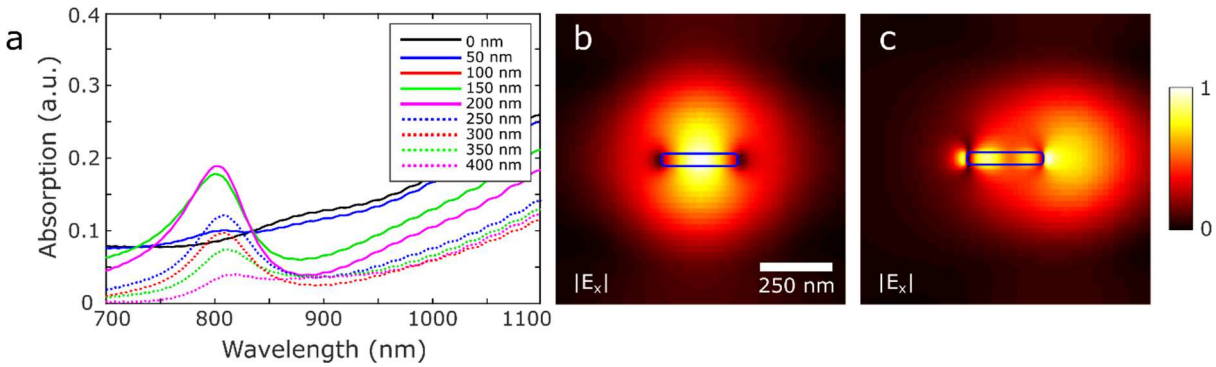

Figure 5.4 Excitation of a quadrupolar mode through beam positioning. We simulate a Gaussian beam with a FWHM of 280 nm and scan it along the axis of a 270 nm Au rod. **(a)** The absorption spectra as the beam is systemically moved from the center of the antenna up to 400 nm away along the antenna axis. **(b)** $|E_x|$ at a wavelength of 800 nm when the beam is centered over the antenna center. The blue rectangle denotes the position of the antenna. **(c)** $|E_x|$ at a wavelength of 800 nm when the beam center is 200 nm away from the antenna center.

Fig. 5.5a shows a piezo scan of a sweep array of gold nanorods in real space, with their length increasing by 20 nm in each row, from 100 to 360 nm. As the dipole resonance is extremely bright, the color scale is saturated to clearly see the quadrupole resonance. Note how the single spot for the dipole resonance splits in two for the antennas between 260 and 300 nm in length (Fig. 5.5a - inset). An antenna with a nominal length of 280 nm (later measured with a SEM and found to be typically 290 ± 5 nm) was selected and a series of BFP images were then taken along its axis while scanning our beam ± 400 nm with respect to its center, with a step size of 50 nm. The counts of each of the BFP images were integrated and plotted with respect to the beam position (Fig. 5.5b – red curve). Note how the two peaks are centered approximately ± 200 nm from the antenna center, which corresponds exactly with the simulations in Fig. 5.4. We then integrate the pixels from the top and bottom halves of each BFP image, calculate their quotient and then plot the logarithm of each quotient with respect to the beam position to help quantify the directionality in dB (Fig. 5.5b – blue curve). The values range from -3.2 to 2.6 dB, which correspond to 2.1 times more counts in the bottom half space than in the top, and 1.8 times more counts the top than in the bottom, respectively. We attribute the slight asymmetries in both the directionality factors and the total counts to slight fabrication differences in the antenna edges. Sharper/duller apexes in a nanoantenna can easily cause minor changes in the linear excitation fields that in turn become much more noticeable in nonlinear signals because of their exponential relation.

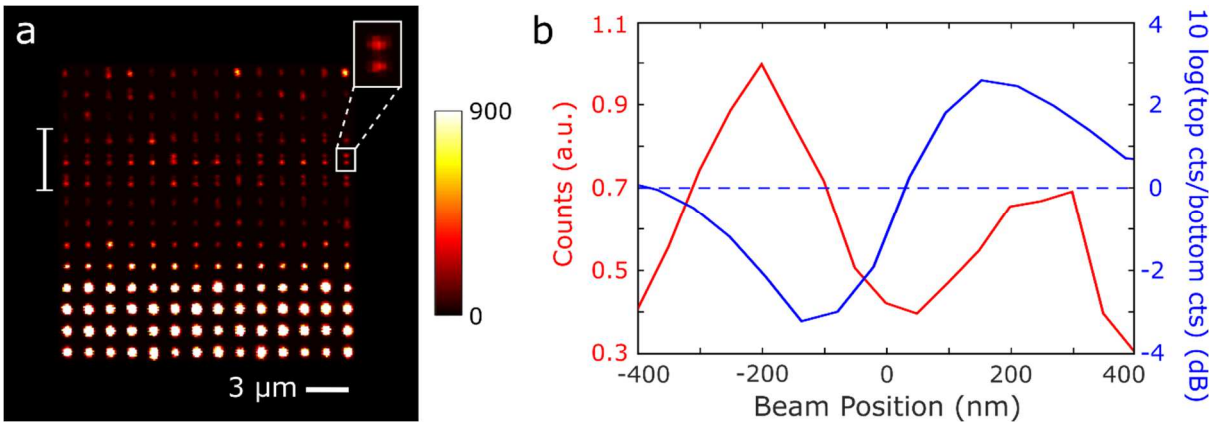

Figure 5.5 Second harmonic generation from a λ antenna. (a) A piezo scan of the SHG from a sweep array of nanoantennas, with each row corresponding to a 20 nm increase in antenna length, from 100 (bottom) to 360 nm (top). The antennas are vertically oriented. Note how in the inset there are two spots for one antenna; this is consistent for the three rows of antennas marked on the left of the scan. Those rows correspond to antennas that are nominally 260, 280 and 300 nm in length. The color scale is in counts/5 ms and was saturated by a factor of 2 to make the longer antennas visible (e.g. the maximum number of counts was 1800 at one of the dipole antennas). **(b)** The integration of counts in a series of BFP images that were taken while scanning along the antenna axis (red curve), and the logarithm of the quotient of the integration of counts at the top half of each BFP image with respect to the bottom half (blue curve). The dashed blue lines denotes the position where there is zero directionality.

A selection of the BFP images (Fig. 5.6) shows that the emission pattern of each measurement consists mainly of two dominant lobes, oriented at the top and bottom, similar to the linear quadrupole in chapter 3. However, the presence of some emission along the horizontal axis instead of an exact zero is indicative of a more complex system. Furthermore, note that there is a suppression of the top or bottom lobe, depending on the excitation beam position. This effect is most pronounced in Fig. 5.6b and e, which are 300 nm apart. As the BFP images contain angular information in each pixel, we calculate angular plots in polar and azimuth direction, which are quantitative and more intuitive to understand. Fig. 5.7 shows the polar and azimuthal cuts of the data in Fig. 5.6b and e. The front-to-back ratio, defined as the intensity ratio between the point of maximum emission power and its diametrically opposite point in the BFP, are 3.1 and 2.5 (5 and 4 dB) for the directional BFP measurements (Fig. 5.6b and e, respectively).

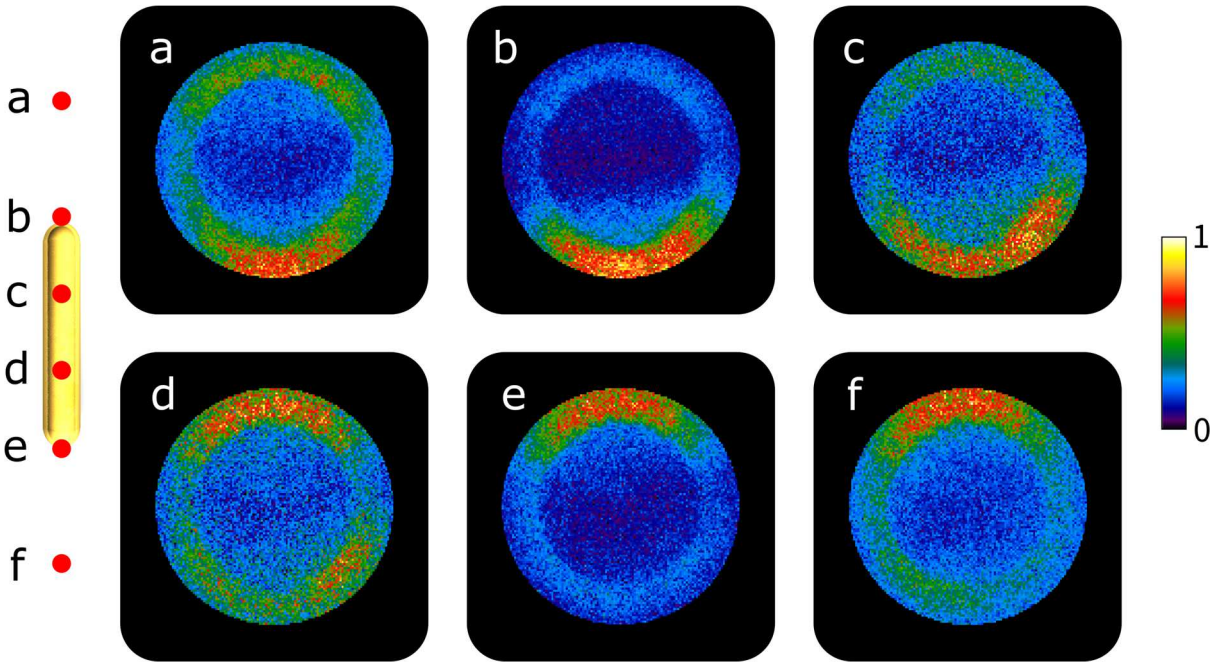

Figure 5.6 Switchable directionality of SHG in a single nanoantenna. Radiation patterns (intensity distribution patterns taken at the back focal plane of our objective) recorded a various positions of our excitation beam respect to the antenna. Note how the predominant emission lobes switches direction as the beam is scanned. **(a-c)** BFP images taken with our excitation beam centered 300, 150 and 50 nm above the antenna center. **(d-f)** BFP images taken with our excitation beam centered 50, 150 and 300 nm below the antenna center.

The switchable emission patterns are a result of our asymmetric excitations due to beam displacement, however, a purely E1 + E1 → E2 surface process only explains the existence of the upper and lower quadrupole lobes, as was the case in chapter 3. The lack of a clear zero across the center of the BFP pattern is a sign of at least one other component, specifically, one capable of radiating in this area, and capable of interfering with the upper/lower lobes. Surprisingly, an electric dipole parallel to the linear quadrupole fits this description perfectly, despite not having its emission peaks overlapping with those of the quadrupolar lobes. A least squares fitting algorithm was implemented, with the parameters being the amplitudes of theoretical multipoles, in this case an x-oriented electric dipole and an x-oriented longitudinal quadrupole. The relative phase was $\pi/2$ for Fig. 5.2b, and $3\pi/2$ for Fig. 5.6e.

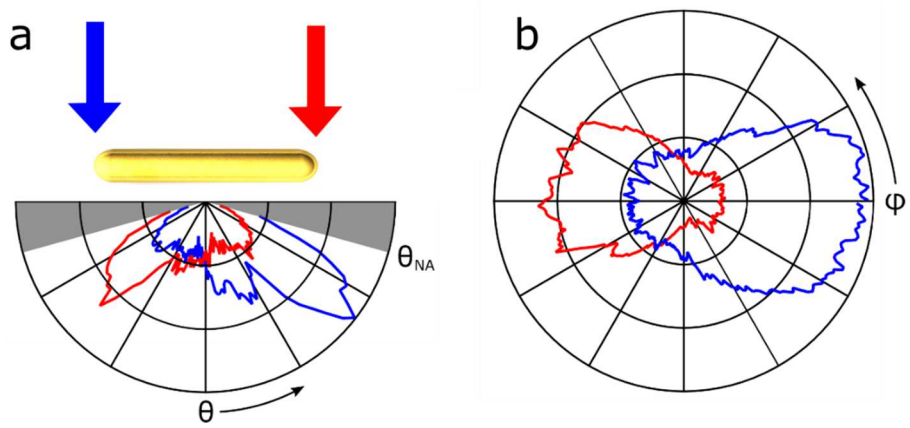

Figure 5.7 Unidirectional emission in angular space. The angular radiation patterns along the polar (θ) and azimuthal (φ) angles, color-coded by the beam position. **(a)** A polar plot for two excitation positions corresponding to Fig. 6.5b (red) and e (blue). The greyed areas correspond to angles outside the maximum collection angle of our detection (73.8°). **(b)** The azimuthal plot of the two aforementioned excitation positions for θ = 60°. The angular patterns were directly calculated from the back-focal-plane images.

5.4 Surface and bulk SHG

To identify the origin of this electric dipole, which explains the directionality of our system reasonably well, we return to FDTD simulations. As was mentioned before, a dipolar component in the second harmonic in this system can be a result of electric field gradients from the bulk or a magnetic dipole component, however, the azimuthal symmetry of the antenna geometry prohibits a magnetic dipole moment. Thus, as the surface and bulk electric field gradient terms also support the E1 + E2 → E1 process, this is the one we analyse in more detail.

Using the same simulations as in Fig. 5.4a, we record the electromagnetic fields in a 3D volume and integrate the internal electric field gradient components throughout the entire antenna volume (Fig. 5.8a-b). Note how in Fig. 5.8a the dominant components are the ones perpendicular to our antenna axis, while in Fig. 5.8b the strongest component is precisely the one needed, with a non-negligible z-component. We also find that the x-component of $(E\cdot\nabla)E$ is strongest within ~4 nm of the antenna apexes. The apex under the excitation beam is about 2.5x stronger than the opposite end, and the rest of the volume is negligible compared to this shell in the case of the x-component, due to relatively low amplitudes and interfering phases along the antenna. Scanning the beam along the antenna axis as was done experimentally reveals that this x-component is non-existent when the beam is centered on the antenna, and that it reaches its maximum when moved 200 nm off center along the antenna axis (Fig. 5.8c). Its phase is also about $\pm \pi/2$ with respect to the fields at the antenna apexes. Integrating $|E|$ throughout the entire antenna volume (Fig. 5.8d) shows no notable features when scanning along the antenna, apart from the fact that the fields drop as the beam is moved away from the antenna. Notice that the peaks in Fig. 5.8c are about 30 nm red-shifted with respect to those in Fig. 5.4a where absorption is maximized for the antenna excitation.

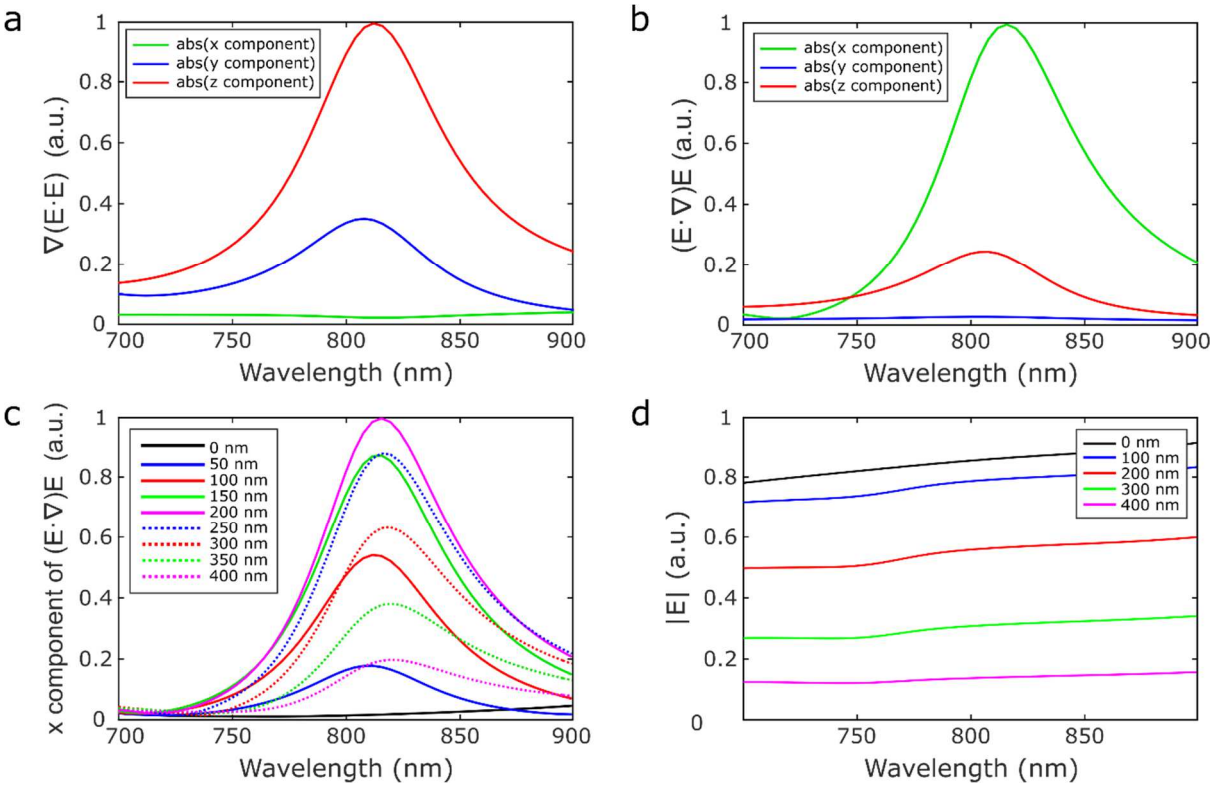

Figure 5.8 Integrated fields of a λ antenna. The simulated field gradients integrated over the entire antenna volume (step size = 2 nm) when driven by a Gaussian beam displaced 200 nm from the antenna center along its axis. **(a)** Spectra of the absolute values of the *x*, *y* and *z* components of ∇(E·E). **(b)** Spectra of the absolute values of the *x*, *y* and *z* components (E·∇)E. **(c)** Spectra of the absolute value of the x component of (E·∇)E for various beam positions. **(d)** Spectra of the integrated values of |E| for several beam positions.

Next, we fit the experimental results to a parallel dipole-quadrupole interference model (Fig. 5.9). Note that while qualitatively the top/bottom lobes are enhanced/diminished, other features are not explained, namely the non-zero background in the experiment, and the horizontal zero that is not displaced as we scan our beam over the antenna. The amplitude and phase of the dipole with respect to the quadrupole is about 0.4 and ± π/2, where an amplitude of unity is the total amount of light emitted by the quadrupole (eq. 5.5). While the fitting algorithm could better match the top/bottom lobes by increasing the dipole amplitude, the increasing shift in the horizontal zero line upwards/downwards made the fit worse overall. The non-zero background may simply be a result of the leaking of incoherent (i.e. omnidirectional) emission from the antenna, possibly three-photon photoluminescence, or perhaps a weak out-of-plane dipole component in SHG (e.g. Fig. 5.8b – red curve), which has minimal interference with the in-plane quadrupole and dipole due to their orthogonal nature. Clearly, the model of dipole-quadrupole interference from a point source is too simplistic. Analysis of the simulated antenna near fields reveals that, for the central wavelength of 800 nm, the antenna apexes are not exactly π out of phase, and they are in fact about 0.1π away from that theoretical ideal, and neither are their amplitudes identical. This asymmetry is a result of one apex being exactly under our excitation field, and thus the fields are a complex sum of the plasmon resonance and

the incident field, whereas the field on the opposite end is entirely induced. In Chapter 3 we discussed why there is little-to-no crosstalk through the antenna between the second fields, and this reasoning is doubly true for an antenna more than twice as long. However, as the central second harmonic wavelength is 400 nm, the fact that the apex dipoles (which we typically modelled as a linear quadrupole) are not exactly π out of phase and are more than $\lambda_{SHG}/2$ apart, means that their interference with each other is not quite a theoretical quadrupole. Thus, their interference with other elements can no longer be easily explained with a simple dipole-quadrupole interference model as any interference can now only by physically explained by multiple electric dipoles with various positions and phases. This interference between multiple parallel dipoles is the mode of operation of a nanowire, though the local phase and amplitude difference have different origins, and this antenna shares a common trait with wire antennas, namely their unmoving emission minimum across the center of their BFP image. While it is beyond the scope of this work to model exactly how many dipoles are required to precisely fit the radiation pattern, the mode of operation of this directional second harmonic antenna and the reason for it remains qualitatively explained through both simulations and experiment.

$$\left[\int \delta \ \left(\boldsymbol{E}_{in}^{(w)} \cdot \boldsymbol{\nabla}\right)\boldsymbol{E}_{in}^{(w)} dV\right]^2 \approx 0.4\left[\int \overleftrightarrow{\boldsymbol{\chi}}_s^{(2)} : \boldsymbol{E}^{(w)}(\boldsymbol{r})\boldsymbol{E}^{(w)}(\boldsymbol{r}) dS\right]^2 \tag{5.5}$$

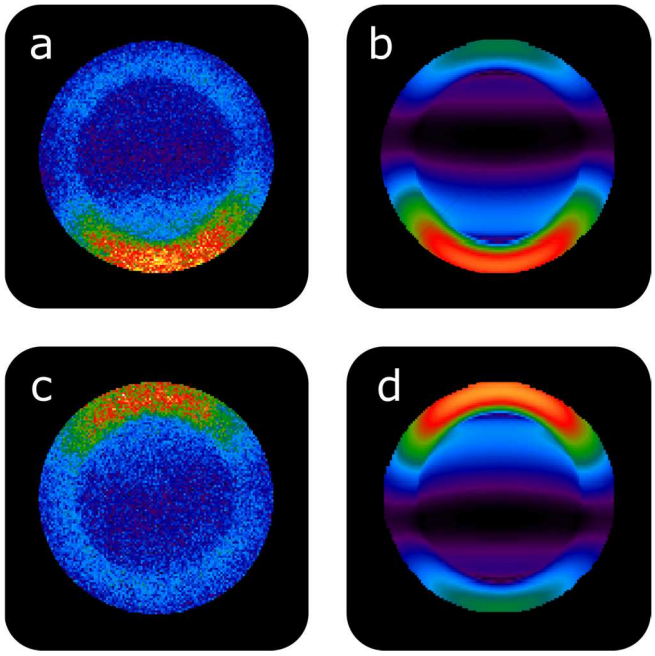

Figure 5.9 Fitted radiation patterns with a point source multipole model. (a) Directional emission when excited from the upper apex of the antenna. **(b)** The fit of a. **(c)** Directional emission when excited from the lower apex of the antenna. **(d)** The fit of c. The phases of the electric dipole in b and d are -π/2 and π/2, respectively, while their relative amplitudes are about 0.4 (where 1 is the total intensity radiated by the quadrupole). The r^2 values for b and d are 0.75 and 0.67, respectively.

In summary, numerical simulations and theoretical fits of experimental data both support the mode of operation of 3 parallel dipoles interfering to give a directed emission of light from a sub-diffraction-limited single-element nanoantenna, with a possible orthogonal dipole and/or an incoherent contribution from photoluminescence.

5.5 Conclusions

We have discussed in detail different modes of operations for directional antennas and how they might work for nonlinear antennas. We also analysed the different $\chi^{(2)}$ transitions possible beyond the electric dipole approximation and designed an antenna to maximize the contribution of the bulk contribution with respect to the surface by using an antenna dark mode. With this design, we demonstrated the switchable unidirectional emission of SHG from a single nanoantenna, which would not have been possible without the bulk contribution that is so often neglected in plasmonics. With both theoretical models and FDTD simulations, we provided evidence that its method of operation is due to the interference of two simultaneous but distinct nonlinear processes, and qualitatively explained the main radiative features of the angular emission. Remarkably, this functionality comes from an object whose footprint is 1/12 of λ_{SHG}^2. Further optimization of the antenna size parameters and pulse shaping of the excitation beam may give a brighter signal and/or more directional response. This nonlinear directional nanoantenna might not beat the efficiency with respect to the U-shaped split-ring resonator antenna studied in chapter 2, but we have gained a key advantage over the SSR, coherence, and thus the ability to dynamically control the interference and thus the emission direction.

List of Publications

- **IM Hancu**, AG Curto, M Castro-Lopez, M Kuttge, and NF van Hulst, "Multipolar interference for directed light emission", *Nano Lett.*14, 166 (2014).

- N Accanto, L Piatkowski, **IM Hancu**, J Renger, and NF van Hulst, "Resonant plasmonic nanoparticles for multicolour second harmonic imaging", *Appl. Phys. Lett.* 108, 083115 (2016).

- M Stockman, […] **IM Hancu**, et al., "Roadmap on plasmonics", *J. Opt*. 20, 4 (2017).

- N Accanto, P de Roque, M Galvan-Sosa, **IM Hancu**, and NF van Hulst, "Closed loop phase control of the coherent two-photon absorption in resonant optical nanoantennas", *submitted* (2018).

- **IM Hancu** and NF van Hulst, "Controlling second harmonic generation from plasmonic dipole antennas", *in preparation* (2018).

- **IM Hancu** and NF van Hulst, "Switchable directional second harmonic generation from a single nanoantenna", *in preparation* (2018).

Bibliography

[1] P Biagioni, JS Huang, and B Hecht, “Nanoantennas for visible and infrared radiation”, *Rep. Prog. Phys. 75*, 24402 (2012).

[2] P Bharadwaj, B Deutsch, and L Novotny, “Optical antennas”, *Adv. Opt. Photon.* 1, 438, (2009).

[3] L Novotny and NF van Hulst, “Antennas for light”, *Nat. Photon*. 5, 83 (2011).

[4] E Kretschmann, “Decay of non radiative surface plasmons into light on rough silver films. Comparison of experimental and theoretical results”, *Opt. Comm.* 6 185-187 (1972).

[5] P Bharadwaj, A Bouhelier, and L Novotny, “Electrical excitation of surface plasmons”, *Phys. Rev. Lett.* 106, 226802 (2011).

[6] KJ Vahala, “Optical microcavities”, *Nature* 424, 839 (2003).

[7] A Kinkhabwala, Z Yu, S Fan, K Muellen, WE Moerner, and Y Avlasevich, “Large single-molecule fluorescence enhancements produced by a bowtie nanoantenna”, *Nature Photon*. 3, 654 (2009).

[8] M Husnik, S Linden, R Diehl, J Niegemann, K Busch, and M Wegener, “Quantitative Experimental Determination of Scattering and Absorption Cross-Section Spectra of Individual Optical Metallic Nanoantennas”, *Phys. Rev. Lett*. 109, 233902 (2012).

[9] CM Dodson and R Zia, “Magnetic dipole and electric quadrupole transitions in the trivalent lanthanide series: Calculated emission rates and oscillator strengths”, *Phys. Rev. B.* 86, 125102 (2012).

[10] S Tojo, M Hasuo, and T Fujimoto, “Absorption Enhancement of an Electric Quadrupole Transition of Cesium Atoms in an Evanescent Field", *Phys. Rev. Lett.* 92, 053001 (2004).

[11] A Compaan and HZ Cummins, “Resonant Quadrupole-Dipole Raman Scattering at the 1S Yellow Exciton in Cu2O”, *Phys. Rev. Lett.* 31, 41 (1973).

[12] ML Andersen, S Stobbe, AS Sorensen, and P Lodahl, “Strongly modified plasmon–matter interaction with mesoscopic quantum emitters”, *Nature Phys.* 7, 215 (2011).

[13] JR Zurita-Sánchez and L Novotny, “Multipolar interband absorption in a semiconductor quantum dot”, *J. Opt. Soc. Am. B* 19, 1355 (2012).

[14] M Moskovits and DP DiLella, “Intense quadrupole transitions in the spectra of molecules near metal surfaces”, *J. Chem. Phys.* 77, 1655 (1982).

[15] PG Etchegoin and ECL Ru, “Multipolar emission in the vicinity of metallic nanostructures”, *J. Phys.: Cond. Matter* 18, 1175 (2006).

[16] PK Jain, D Ghosh, R Baer, E Rabani, and AP Alivisatos, “Near-field manipulation of spectroscopic selection rules on the nanoscale”, *Proc. Natl, Acad. Sci. USA* 109, 8016 (2012).

[17] M Kauranen and AV Zayats, “Nonlinear plasmonics”, *Nat. Photonics* 6, 737-748 (2012).

[18] MA Lieb, JM Zavislan, and L Novotny, “Single-molecule orientations determined by direct emission pattern imaging”, *J. Opt. Soc. Am. B* 21, 1210 (2004).

[19] AM Weiner DE Leaird, JS Patel, and JR Wullert, “Programmable femtosecond pulse shaping by use of a multielement liquid-crystal phase modulator”, *Opt. Lett*. 15, 326 (1990).

[20] AM Weiner, “Femtosecond pulse shaping using spatial light modulators”, *Rev. Sci. Instrum.* 71 1929 (2000).
[21] AM Weiner, DE Leaird, JS Patel, and JR Wullert, “Programmable shaping of femtosecond optical pulses by use of 128-element liquid crystal phase modulator”, *IEEE J. Quantum Electron*. 28, 908 (1992).
[22] DH Reitze, AM Weiner, and DE Leaird, “Shaping of wide bandwidth 20 femtosecond optical pulses”, *Appl. Phys. Lett.* 61, 1260 (1992).
[23] D Meshulach, D Yelin, and Y Silberberg, “Adaptive ultrashort pulse compression and shaping”, *Opt. Commun*. 138, 345 (1997).
[24] T Feurer, JC Vaughan, RM Koehl, and KA Nelson, “Multidimensional control of femtosecond pulses by use of a programmable liquid-crystal matrix”, *Opt. Lett.* 27, 652 (2002).
[25] A Monmayrant, S Weber, B Chatel, “A newcomer's guide to ultrashort pulse shaping and characterization”, *J. Phys. B.: At. Mol. Opt. Phys*. 43, 103001 (2010).
[26] VV Lozovoy, I Pastrik, M Dantus, “Multiphoton intrapulse interference. IV. Ultrashort laser pulse spectral phase characterization and compensation”, *Opt. Lett.* 29, 775 (2004).
[27] VV Lozovoy, M Dantus, “Laser control of physicochemical processes; experiments and applications”, *Annu. Rep. Prog. Chem., Sect. C: Phys. Chem.* 102, 227 (2006).
[28] D Brinks, M Castro-Lopez, R Hildner, NF van Hulst, “Plasmonic antennas as design elements for coherent ultrafast nanophotonics”, *Proc. Natl. Acad. Sci USA* 110, 18386 (2013).
[29] Jackson, JD “Classical Electrodynamics” 3rd ed.; Wiley: New York (1999).
[30] R Trebino. “Frequency-Resolved Optical Gating: The Measurement of Ultrashort Laser Pulses”. Spring Science & Business Media, Moston, MA (2012).
[31] SJ Orfanidis. “Electromagnetic Waves and Antennas”. Rutgers Univeristy (2008).
[32] P Devi, VV Lozovoy, M Dantus, " Measurement of group velocity dispersion of solvents using 2-cycle femtosecond pulses: experiment and theory”, *AIP Advances* 1, 032166 (2011).
[33] P Bowlan, U Fuchs, R Trebino, UD Zeitner, “Measuring the spatiotemporal electric field of tightly focused ultrashort pulses with sub-micron spatial resolution”, *Opt. Express*, 16, 13663 (2008).
[34] R Trebino, “Measuring the seemingly immeasurable”, *Nat. Photon*. 5, 189 (2011).
[35] C Iaconis and IA Walmsley, “Spectral phase interferometry for direct electric-field reconstruction of ultrashort optical pulses”, *Opt. Lett*. 23, 792 (1998).
[36] Y Coello, VV Lozovoy, TC Gunaratne, B Xu, I Borukhovich, C-H Tseng, T Weinacht, and M Dantus, “Interference without an interferometer: a different approach to measuring, compressing, and shaping ultrashort laser pulses”, *J. Opt. Soc. Am. B* 25, A140 (2008).
[37] KA Walowicz, I Pastrik, VV Lozovoy, and M Dantus, “Multiphoton intrapulse interference. 1. Control of multiphoton processes in condensed phases”, *J. Phys. Chem. A* 106, 9369 (2002).
[38] VV Lozovoy, I Pastrik, KA Walowicz, and M Dantus, “Multiphoton intrapulse interference. II. Control of two-and three-photon laser induced fluorescence with shaped pulses”, *J. Chem. Phys.* 118, 3187 (2003).

[39] B Xu, JM Gunn, JM Dela Cruz, VV Lozovoy, and M Dantus, "Quantitative investigation of the multiphoton intrapulse interference phase scan method for simultaneous phase measurement and compensation of femtosecond laser pulses ", *J. Opt. Soc. Am. B* 23, 750 (2006).
[40] VV Lozovoy, B Xu, Y Coello, and M Dantus, "Direct measurement of spectral phase for ultrashort laser pulses", *Opt. Express* 16, 592 (2008).
[41] N Accanto, JB Nieder, L Piatkowski, M Castro-Lopez, F Pastorelli, D Brinks, and NF van Hulst, "Phase control of femtosecond pulses on the nanoscale using second harmonic nanoparticles", *Light Sci. Appl*. 3, e143 (2014).
[42] S Kühn, U Hakason, L Rogobete, and V Sandoghdar, "Enhancement of single-molecule fluorescence using a gold nanoparticle as an optical nanoantenna", *Phys. Rev. Lett*. 97, 017402 (2006).
[43] P Anger, P Baradwaj, and L Novotny ," Enhancement and quenching of single-molecule fluorescence", *Phys. Rev. Lett*. 96, 113002 (2006).
[44] TH Taminiau, FD Stefani, and NF van Hulst, *Opt. Express 16*, 16858–16866 (2008).
[45] TH Taminiau, RJ Moerland, FB Segerink, L Kuipers, and NF van Hulst. *Nano Lett*. 7, 28 (2007).
[46] P Grahn, A Shevchenko, and M Kaivola, "" *New J. Phys. 14*, 093033 (2014).
[47] S Mühlig, C Menzel, C Rockstuhl, and F Lederer, *Metamaterials 5*, 64–73 (2011).
[48] T Inoue and H Hori, *Opt. Rev. 5*, 295–302 (1998).
[49] AG Curto, TH Taminiau, G Volpe, MP Kreuzer, R Quidant, and NF van Hulst, *Nat. Commun. 4*, 1750 (2013).
[50] AG Curto, G Volpe, TH. Taminiau, MP Kreuzer, R Quidant, and NF van Hulst, *Science* 329, 930 (2011).
[51] T Kosako, Y Kadoya, and HF Hofmann, *Nat. Photon. 4* (2010).
[52] D Dregely, R Taubert, J Dorfmüller, R Vogelgesang, K Kern, and H Giessen, *Nat. Commun. 2*, 267 (2011).
[53] HJ Lezec, A Degiron, E Devaux, RA Linke, L Martin-Moreno, FJ Garcia-Vidal, and TW Ebbesen, *Science 297*, 820–2 (2002).
[54] H Aouani, O Mahboub, N Bonod, E Devaux, E Popov, H Rigneault, TW Ebbesen, and J Wenger, *Nano Lett. 11*, 637–644 (2011).
[55] YC Jun, KCY Huang, and ML Brongersma, *Nat. Commun. 2*, 283 (2011).
[56] B Rolly, B Stout, S Bidault, and N Bonod, *Opt. Lett.* 36, 3368–70 (2011).
[57] T Shegai, VD Miljkovic, K Bao, H Xu, P Nordlander, P Johansson, and M Käll, "Unidirectional Broadband Light Emission from Supported Plasmonic Nanowires", *Nano Lett.* 11, 706-711 (2011).
[58] Y Wang, AS Helmy, and GV Eleftheriades, "Ultra-wideband optical leaky-wave slot antennas", *Opt. Express* 19, 12392 (2011).
[59] C Belacel, B Habert, F Bigourdan, F Marquier, J-P Hugonin, SM de Vasconcellos, X Lafosse, L Coolen, C Schwob, C Javaux, B Dubertret, J-J Greffet, P Senellart, and A Maitre, "Controlling spontaneous emission with plasmonic optical patch antennas", *Nano Lett.* 13, 1516 (2013).
[60] DT Schoen, T Coenen, FJ García de Abajo, ML Brongersma, and A Polman, "The planar parabolic optical antenna", *Nano Lett.* 13, 188–193 (2013).

[61] M Nieto-Vesperinas, R Gomez-Medina, and JJ Saenz, "Angle-suppressed scattering and optical forces on submicrometer dielectric particles", *J. Opt. Soc. Am. A 28*, 54–60 (2011).
[62] S Person, M Jain, Z Lapin, JJ Sáenz, G Wicks,and L Novotny, "Demonstration of zero optical backscattering from single nanoparticles", *Nano Lett.* 13, 1806–9 (2013).
[63] YH Fu, AI Kuznetsov, AE Miroshnichenko, YF Yu, and B Luk'yanchuk, "Directional visible light scattering by silicon nanoparticles", *Nat. Commun*. 4, 1527 (2013).
[64] AE Krasnok, DS Filonov, PA Belov, AP Slobozhanyuk, R Constantin, and YS Kivshar, "Ultracompact all-dielectric superdirective antennas", *arXiv* 1211.0230 (2012).
[65] B Rolly, B Stout, and N Bonod, "Boosting the directivity of optical antennas with magnetic and electric dipolar resonant particles", *Opt. Express* 2012, *20*, 20376–20386.
[66] B Rolly, J-M Geffrin, R Abdeddaim, B Stout, and N Bonod, "Controllable emission of a dipolar source coupled with a magneto-dielectric resonant subwavelength scatterer", *Sci. Rep.* 2013, *3*, 3063.
[67] G Pellegrini, P Mazzoldi, and G Mattei, "Asymmetric plasmonic nanoshells as subwavelength directional nanoantennas and color nanorouters: a multipole interference approach", *J. Phys. Chem. C* 2012, *116*, 21536–21546.
[68] W Liu, AE Miroshnichenko, DN Neshev, and YS Kivshar, "Broadband unidirectional scattering by magneto-electric core–shell nanoparticles", *ACS Nano* 2012, *6*, 5489–5497.
[69] NA Mirin and NJ Halas, "Light-bending nanoparticles", *Nano Lett.* 2009, *9*, 1255–1259.
[70] D Vercruysse, Y Sonnefraud, N Verellen, FB Fuchs, G Di Martino, L Lagae, VV Moshchalkov, SA Maier, and P Van Dorpe, "Unidirectional side scattering of light by a single-element nanoantenna", *Nano Lett.* 2013, *13*, 3843–9.
[71] CM Soukoulis and M Wegener, "Past achievements and future challenges in the development of three-dimensional photonic metamaterials", *Nat. Photon.* 5, 523 (2011).
[72] C Enkrich, M Wegener, S Linden, S Burger, L Zschiedrich, F Schmidt, J Zhou, T Koschny, and C Soukoulis, "Magnetic metamaterials at telecommunication and visible frequencies", *Phys. Rev. Lett.* 2005, *95*, 203901.
[73] C Rockstuhl, F Lederer, C Etrich, T Zentgraf, J Kuhl, and H Giessen, "On the reinterpretation of resonances in split-ring-resonators at normal incidence", *Opt. Express* 2006, *14*, 8827–8836.
[74] J Zhou, T Koschny, and CM Soukoulis, *Opt. Express* 2007, *15*, 17881–17890.
[75] G Boudarham, N Feth, V Myroshnychenko, S Linden, J García de Abajo, M Wegener, and M Kociak, "Magnetic and electric excitations in split ring resonators", *Phys. Rev. Lett.* 2010, *105*, 255501.
[76] W Lukosz, "Light emission by magnetic and electric dipoles close to a plane dielectric interface. III. Radiation patterns of dipoles with arbitrary orientation", *J. Opt. Soc. Am.* 1979, *69*, 1495–1503.
[77] CA Balanis, "Antenna Theory: Analyses and Design" 3rd ed., John Wiley and Sons, Inc.: Hoboken, New Jersey (2005).
[78] L Novotny and B Hecht, "Principles of Nano-Optics" 2nd ed., Cambridge University Press: Cambridge (2012).

[79] FJ Rodríguez-Fortuño, C García-Meca, R Ortuño, J Martí, and A Martínez, "Modeling high-order plasmon resonances of a U-shaped nanowire used to build a negative-index metamaterial", *Phys. Rev. B* 79, 075103 (2009).
[80] FB Arango and AF Koenderink, "Polarizability tensor retrieval for magnetic and plasmonic antenna design", *New J. Phys.* 15, 073023 (2013).
[81] J Yao, L Yang, Y Ye, "An antenna to direct light to opposite directions", *Opt. Commun.* 300, 274–276 (2013).
[82] N Verellen, Y Sonnefraud, H Sobhani, F Hao, VV Moshchalkov, P Van Dorpe, P Nordlander, and SA Maier, "Fano resonances in individual coherent plasmonic nanocavities", *Nano Lett.* 9, 1663–7 (2009).
[83] B Luk'yanchuk, NI Zheludev, SA Maier, NJ Halas, P Nordlander, H Giessen, and CT Chong, "The Fano resonance in plasmonic nanostructures and metamaterials", *Nat. Mater*. 9, 707–15 (2010).
[84] E Plum, VA Fedotov, and NI Zheludev, "Planar metamaterial with transmission and reflection that depend on the direction of incidence", *Appl. Phys. Lett.* 94, 131901 (2009).
[85] I Sersic, MA van de Haar, FB Arango, and AF Koenderink, "Ubiquity of optical activity in planar metamaterial scatterers", *Phys. Rev. Lett.* 108, 223903 (2012).
[86] J Butet, P-F Brevet, and OJF Martin, "Optical Second Harmonic Generation in Plasmonic Nanostructures: From Fundamental Principles to Advacned Applications" *ACS Nano* 9 (11) 10545-10562 (2015).
[87] K Kneipp, Y Wang, H Kneipp, LT Perelman, I Itzkan, RR Dassari, and MS Feld. "Single molecule detection using Surface-Enhanced Raman Scattering". *Phys. Rev. Lett.* 78, 1667 (1997).
[88] S Nie and SR Emory, "Probing Single Molecules and Single Nanoparticles by Surface-Enhanced Raman Scattering". *Science* 21, 275 (1997).
[89] JI Dadap, J Shan, KB Eisenthal, TF Heinz, "Second-harmonic Rayleigh scattering from a sphere of centrosymmetric material", *Phys. Rev. Lett.* 83 (20), 4045–4048 (1999).
[90] JI Dadap, J Shan, TF Heinz, "Theory of optical second-harmonic generation from a small sphere of centrosymmetric material: small particle limit", *J. Opt. Soc. Am. B* 21, (2004).
[91] SG Rodrigo, H Harutyunyan, and L Novotny, "Coherent Control of Light Scattering from Nanostructured Materials by Second-Harmonic Generation". *Phys. Rev. Lett.* 110, 177405 (2013).
[92] P Reichenbach and LM Eng, "3D-steering and superfocusing of second-harmonic radiation through plasmonic nano antenna arrays", *J. Laser App* **24**, 042005 (2012).
[93] SB Hasan, C Etrich, R Filter, C Rockstuhl, and F Lederer, "Enhancing the nonlinear response of plasmonic nanowire antennas by engineering their terminations", *Phys. Rev. B* 88, 205125 (2013).
[94] D de Ceglia, MA Vincenti, C De Angelis, A Locatelli, JW Haus, and M Scalora "Role of antenna modes and field enhancement in second harmonic generation from dipole nanoantennas", *Opt. Express* 23, 2 (2015).
[95] GD Bernasconi, J Butet, and OJF Martin, "Mode analysis of second-harmonic generation in plasmonic nanostructures", *J. Opt. Soc. Am. B*, 33, 4 (2016).

[96] K Thyagarajan, J Butet, OJF Martin, “Augmenting second harmonic generation using Fano resonances in plasmonic systems”, *Nano Lett.* 13, 1847 (2013).
[97] K Thyagarajan, S Rivier, A Lovera, OJF Martin, “Enhanced second-harmonic generation from double resonant plasmonic antennae”, *Opt. Express* 20, 12860 (2012).
[98] J Butet, and OJF Martin, “Fano resonances in the nonlinear optical response of coupled plasmonic nanostructures”, *Opt. Express* 22, 24 (2014).
[99] PY Chen, C Argyropoulos, G D’Aguanno, A Alù, “Enhanced Second-Harmonic Generation by Metasurface Nanomixer and Nanocavity”, *ACS Photonics* 2, 1000-1006 (2015).
[100] H Linnenbank and S Linden, “Second harmonic generation with two-photon resonant plasmonic metamaterials”, *Optica* 1, 1 (2014).
[101] M Lippitz, MA van Dijk and M Orrit, “Third-Harmonic Generation from Single Gold Nanoparticles”, *Nano Lett*. 5, 799-802 (2005).
[102] C Anceau, S Brasselet, J Zyss, and P Gadenne, “Local second-harmonic generation enhancement on gold nanostructures probed by two-photon microscopy”, *Opt. Lett*. 28, 9 (2003).
[103] S. Viarbitskaya, O Demichel, B Cluzel, GC des Francs, and A Bouhelier, “Delocalization of Nonlinear Optical Responses in Plasmonic Nanoantennas”, P*hys. Rev. Lett.* 115, 197401 (2015).
[104] H. Aouani, M. Rahmani, M Navarro-Cia, and SA Maier, “Third-harmonic-upconversion enhancemnet from a single semiconductor nanoparticle coupled to a plasmonic antenna”, *Nat. Nanotechnol*. 9, 290 (2014).
[105] Celebrano, M.; Wu, X.; Baselli, M.; Großmann, S.; Biagioni, P.; Locatelli, A.; De Angelis, C.; Cerullo, G.; Osellame, R.; Hecht, B.; Duò, L.; Ciccacci, F.; Finazzi, M., “Mode matching in multiresonant plasmonic nanoantennas for enhanced second harmonic generation”, *Nat. Nanotechnol.* 10, 412 (2015).
[106] Berthelot, J.; Bachelier, G.; Song, M.; Rai, P.; Dereux, A.; Bouhelier, A. “Silencing and enhancement of second-harmonic generation in optical gap antennas”, *Opt. Express* 20, 10498 (2012).
[107] P Mühlschlegel, H-J Eisler, OJF Martin, B Hecht, and DW Pohl, “Resonant Optical Antennas”, *Science* 308, 5728 (2005).
[108] J Chen, A Kravasin, P Ginsburg, AV Zayats, T Pullerits and KJ Karki, “Evidence of High-Order Nonlinearities in Supercontinuum White-Light Generation from a Gold Nanofilm”, *ACS Photonics* 5, 5 (2018).
[109] P Vasa, M Singh, R Bernard, AK Dharmadhikari, JA Dharmadhikari, and D Mathur, “Supercontinuum generation in water doped with gold nanoparticles”, *Appl. Phys. Lett*. 103, 111109 (2013).
[110] FJ Rodríguez-Fortuño, G Marino, P Ginzburg, D O’Connor, A Martínez, GA Wurtz, and AV Zayats, “Near Field Interference for the Unidirectional Excitation of Electromagnetic Guided Modes”, *Science* 340, 6130 (2013).
[111] Z Chen, T Holmgaard, SI Bozhevolnyi, AV Krasavin, AV Zayats, L Markey, and A Dereux, “Wavelength-selective directional coupling with dielectric-loaded plasmonic waveguides”, *Opt. Lett.* 34, 3 (2009).

[112] M Qiu, M Mulot, M Swillo, S Anand, B Jaskorzynska, and A Karlsson, "Photonic crystal optical filter based on contra-directional waveguide coupling", *Appl. Phys. Lett.* 83, 5121 (2003).
[113] H Mesnil, and F Hache, "Experimental Evidence of Third-Order Nonlinear Dichroism in a Liquid of Chiral Molecules", *Phys. Rev. Lett.* 85, 4257 (2000).
[114] M Ren, E Plum, J Xu, and NI Zheludev, "Giant nonlinear optical activity in plasmonic metamaterial", *Nat. Commun.* 3, 833 (2012).
[115] R Li, R Sullivan, W Al-Basheer, RM Pagni, and RN Compton, "Linear and nonlinear circular dichroism of R-(+)-3-methylcyclopentanone", *J. Chem. Phys.* 125, 144304 (2006).
[116] YS Kivshar and A Miroshnichenko, "Meta Optics with Mie Resonances", *Opt. Photonics News* 28, 24-31 (2017).
[117] I Staude, AE Miroshnichenko, M Decker, NT Fofang, S Liu, E Gonzales, J Dominguez, TS Luk, DN Neshev, I Brener, and YS Kivshar, "Tailoring Directional Scattering through Magnetic and Electric Resonances in Subwavelength Silicon Nanodisks", *ACS Nano* 7, 9 (2013).
[118] AI Kuznetsov, AE Miroshnichenko, ML Brongersma, YS Kivshar, B Luk'yanchuk, "Optically resonant dielectric nanostructures", *Science* 18, 354 (2016).
[119] Lord Rayleigh, "The Problem of the Whispering Gallery," *Scientific Papers* 5, 617–620 (1912).
[120] D Smirnova and YS Kivshar, "Multipolar nonlinear nanophotonics", *Optica* 3, 11 (2016).
[121] MR Shcherbakov, PB Vabishchevich, AS Shorokhov, KE Chong, D-Y Choi, I Staude, AE Miroshnichenko, DN Neshev, AA Fedyanin, and YS Kivshar, "Ultrafast All-Optical Switching with Magnetic Resonances in Nonlinear Dielectric Nanostructures", *Nano Lett*. 15, 10 (2015).
[122] S Buckley, M Radulaski, J Petykiewicz, KG Lagoudakis, J-H Kang, M Brongersma, K Biermann and J Vuckovic, "Second harmonic generation in GaAs photonic crystal cavities in (111)B and (001) crystal orientations", *ACS Photonics* 1, 516-523 (2014).
[123] Y Yang, W Wang, A Boulesbaa, II Kravchenko, DP Briggs, A Puretzky, D Geohegan, and J Valentine, "Nonlinear Fano-Resonant Dielectric Metasurfaces", *Nano Lett*. 15, 7388-7393 (2015).
[124] Y Zeng, I Roland, X Checoury, Z Han, M El Kurdi, S Sauvage, B Gayral, C Brimont, T Guillet, M Mexis, F Semond, and P Boucaud, "Resonant second harmonic generation in a gallium nitride two-dimensional photonic crystal on silicon", *Appl. Phys. Lett.* 106, 081105 (2015).
[125] C Wang, Z Li, M-H Kim, X Xiong, X-F Ren, G-C Guo, N Yu, and M Loncar, "Metasurface-assisted phase-matching-free second harmonic generation in lithium niobate waveguides", *Nat. Commun*. 8, 2098 (2017).
[126] PR Wiecha, A Arbouet, H Kallel, P Periwal, T Baron and V Paillard, "Enhanced nonlinear optical response from individual silicon nanowires", *Phys. Rev. B* 91, 121416 (2015).

[127] PR Wiecha, A Arbouet, C Girard, T Baron, and V Paillard, “Origin of Second Harmonic Generation from Individual Silicon Nanowires”, *Phys. Rev. B* 93, 125421 (2016).
[128] P Guyot-Sionnest, and YR Shen, “Bulk contribution in surface second-harmonic generation”, *Phys. Rev. B* 38, 7985 (1988).
[129] JI Dadap, “Optical second-harmonic scattering from cyllindrical particles”, *Phys. Rev. B* 78, 205322 (2008).
[130] S Cattaneo, and M Kauranen, “Polarization-based identification of bulk contributions in surface nonlinear optics”, *Phys. Rev. B* 72, 235403 (2005).
[131] SV Makarov, MI Petrov, U Zywietz, V Milichko, D Zuev, N Lopanitsyna, A Kuksin, I Mukhin, G Zograf, E Ubyivovk, DA Smirnova, S Starikov, BN Chichkov, and YS Kivshar, “Efficient Second-Harmonic Generation in Nanocrystalline Silicon Nanoparticles”, *Nano Lett*. 17, 5 (2017).
[132] M Falasconi, LC Andreani, AM Malvezzi, M Patrini, V Mulloni, and L Pavesi, “Bulk and surface contributions to second-order susceptibility in crystalline and porous silicon by second-harmonic generation”, *Surface Science* 481, 105 (2001).
[133] CK Chen, ARB de Castro, YR Shen, and F DeMartini, “Surface Coherent Anti-Stokes Raman Spectroscopy”, *Phys. Rev. Lett*. 43, 946 (1979).
[134] T Ichimura, N Hayazawa, M Hashimoto, Y Inouye, and S Kawata, “Tip-Enahnced Coherent Anti-Stokes Raman Scattering for Vibrational Nanoimaging”, *Phys. Rev. Lett*. 92, 220801 (2004).
[135] Y Zhang, Y-R Zhen, O Neumann, JK Day, P Nordlander, and NJ Halas, “Coherent anti-Stokes Raman scattering with single-molecule sensitivity using a plasmonic Fano resonance”, *Nat. Commun*. 5, 4424 (2014).
[136] S Yampolsky, DA Fishman, S Dey, E Hulkko, M Banik, EO Potma and VA Apkarian, “Seeing a single molecule vibrate through time-resolved coherent anti-stokes Raman scattering”, *Nat. Photonics* 8, 650-656 (2014).
[137] S Zhang, H Wei, K Bao, U Kakanson, NJ Halas, P Nordlander, and H Xu, “Chiral Surface Plasmon Polaritons on Metallic Nanowires”, *Phys. Rev. Lett*. 107, 096801 (2011).
[138] Z Li, F Hao, Y Huang, Y Fang, P Nordlander, and H Xu, “Directional Light Emission from Propagating Surface Plasmoncs of Silver Nanowires”, *Nano Lett.* 9, 12 (2009).
[139] D van Dam, DR Abujetas, R Paniagua-Domínguez, JA Sánchez-Gil, EPAM Bakkers, JEM Haverkort, and J Gómez Rivas, “Directional and Polarized Emission from Nanowire Arrays”, *Nano Lett*. 15, 7 (2015).
[140] M Finazzi, P Biagioni, M Celebrano, and L Duò, “Selection rules for second-harmonic generation in nanoparticles”, *Phys. Rev. B* 76, 12 (2007).
[141] D Timbrell, JW You, YS Kivshar, and NC Panoiu, “A comparative analysis of surface and bulk contributions to second-harmonic generation in centrosymmetric nanoparticles”, *Sci. Rep.* 8, 3586 (2018).
[142] M Ethis de Corny, N Chauvet, G Laurent, M Jeannin, L Olgeirsson, A Drezet, S Huant, G Dantelle, G Nogues, and G Bachelier, “Wave-Mixing Origin and Optimization in Single and Compact Aluminum Nanoantennas”, *ACS Photonics* 8, 10 (2016).